UNIVERSITY OF CALIFORNIA
RIVERSIDE

Illuminating Large Stable Isotope Variations in Alkaline Lakes

A Dissertation submitted in partial satisfaction
of the requirements for the degree of

Doctor of Philosophy

in

Earth and Planetary Sciences

by

Christopher John Tino

December 2023

Dissertation Committee:
Dr. Timothy W. Lyons, Chairperson
Dr. Eva E. Stüeken
Dr. Maryjo N. Brounce
Dr. Gordon D. Love

The Dissertation of Christopher John Tino is approved:

_____

_____

_____

_____

Committee Chairperson

University of California, Riverside

ACKNOWLEDGEMENTS

Writing these acknowledgements is in some ways an uncomfortable experience, because it forces me to reflect on all of the lesser paths that graduate school, and life more broadly, could have taken if not for my remarkably good fortune. First among these strokes of luck are the people that raised me—my parents and siblings. Their strong moral compasses and deeply felt understanding of what is most valuable in life has provided a high standard that I'm constantly striving towards, albeit mostly in vain.

I would not have gone to graduate school—let alone complete it—without my wife, JJ. Her sacrifices on my behalf have been profound and near-constant. For all of my talk of eventually becoming a PhD scientist, it was her early and unwavering support that pushed me to apply with confidence and ambition. That her family would also become a source of thoughtful kindness and support is yet another unearned boon.

How does an unsatisfied microbiology analyst become a biogeochemist that has studied remarkable sites all over the world? The answer is simple: other people. The first class I took at UCR was a so-called "isotope boot camp" run by Marilyn Fogel. One does not have to read far into this dissertation to surmise the immense impact this has had on my work. I feel honored to have known Marilyn, if only for a short time. Steve Bates has been an outstanding technical mentor and a thoughtful friend. Jen Stern has provided insightful and uplifting mentorship. The entire Lyons lab has been occupied exclusively by intelligent, distinctive, and considerate minds that are always willing to lend a hand. As has the Schwieterman lab, which invited me to meetings during collectively trying times, providing a much-needed sense of momentum and joy for research. Dan Gregory

showcased the work ethic and integrity needed to jumpstart a great career. Ying Lin and Laurie Graham have kept me sane with their diligent approach to seemingly insurmountable technical issues. A special acknowledgement must be made to my office mate Chenyi Tu, with whom I've shared many wonderful conversations that have extended well beyond business hours. And to Nate Marshall, who witnessed me flail while foolishly attempting to hike muddy Olomana Ridge in sandals. There are, as always, too many terrific people to properly capture in this space.

I would like to acknowledge my committee members. Thank you to Gordon Love and Maryjo Brounce, who have always kept their doors open and held a genuine, continued interest in my work. Thank you to Eva Stüeken, who has been there from the start and has set the pace with an unparalleled dedication to geochemistry. You have always made time and treated me as your own student. This dissertation does not exist without your remarkable generosity and sense of obligation.

None of these enriching encounters happen without the person who provided me with this extraordinary opportunity. Thank you, Tim. You have always led by example—for all your creativity and knowledge, it was never in doubt that hard work and empathy are the true pillars of success. By mentoring with patience and allowing complete intellectual freedom, you have given me one of the most rewarding graduate experiences imaginable. I can only hope to have held up my end of the bargain. These years have been transformative, thank you for giving me the chance.

DEDICATION

"How far back must you go to discover the beginning of trouble?"
Philip Roth, *Goodbye, Columbus*

For my wife, JJ – I'd use your full name, but you'd never forgive me.

ABSTRACT OF THE DISSERTATION

Illuminating Large Stable Isotope Variations in Alkaline Lakes

by

Christopher John Tino

Doctor of Philosophy, Graduate Program in Earth and Planetary Sciences
University of California, Riverside, December 2023
Dr. Timothy W. Lyons, Chairperson

Stable isotopes ratios have yielded major geochemical insights since the mid-twentieth century, and yet there remains new ground to be broken when analyzing traditional isotopic systems in extreme environments. This dissertation relies on such analyses—including $\delta^{13}C$, $\delta^{18}O$, $\delta^{15}N$, and $\delta^{34}S$—at ancient and modern alkaline lakes. The specificity of these environments belies their broader significance, including for the earliest (> 3.5 Ga) Earth and Mars. For instance, impact craters, which were a vital feature of those systems, tend to produce alkaline lakes as a result of the weathering of mafic impact ejecta. Alkaline lakes are also among the most bioproductive natural aquatic environments, with chemistries favorable for accumulating bioessential compounds thought necessary for a *de novo* origin of life. The novel datasets within this dissertation investigate the capacity for alkaline lakes to exhibit distinct isotopic records. The exceptional nature of such signatures, particularly when combined with various contextual data, may allow them to act as effective proxies for past conditions. Notable examples include $\delta^{34}S$ evidence of Rayleigh distillation during sulfate reduction within an impact-induced hydrothermal paleolake (Chapter 1), as well as

the connection between pH and elevated $\delta^{15}N$ via ammonia volatilization (Chapter 2); both of these topics are investigated at the Miocene Ries crater lake in southern Germany. To further elucidate $\delta^{15}N$ increases via ammonia volatilization, multiple extant lakes of the Coorong lagoon in South Australia are examined (Chapter 3). The results suggest hypersalinity is an important control on heightened $\delta^{15}N$ dynamics and preservation in shallow alkaline systems. The dissertation work is then placed within a broader context (Chapter 4) by reviewing additional putative sites of ammonia volatilization; this includes a new stable isotope data set from the Green River Formation. A schematic for elevated $\delta^{15}N$ in redox-stratified basins is proposed, based on the balance of ammonia volatilization and denitrification in response to spatial and temporal shifts in pH, salinity, and chemocline depth. In sum, alkaline lakes can exhibit remarkably distinct $\delta^{15}N$ and $\delta^{34}S$ signatures, which can help establish constraints on aqueous conditions at sites of high geologic and astrobiological value.

TABLE OF CONTENTS

LIST OF FIGURES

LIST OF TABLES

Chapter 1

Are Large Sulfur Isotope Variations Biosignatures in an Ancient, Impact-Induced Hydrothermal Mars Analog?

Preface:

The contents of this chapter have been published in a modified form as:

Tino, C. J., Stüeken, E. E., Arp, G., Böttcher, M. E., Bates, S. M., & Lyons, T. W. (2023). Are Large Sulfur Isotope Variations Biosignatures in an Ancient, Impact-Induced Hydrothermal Mars Analog? *Astrobiology*. ahead of print, DOI: 10.1089/ast.2022.0114.

Abstract

Discrepancies have emerged concerning the application of sulfur stable isotope ratios as a biosignature in impact crater paleolakes. The first in-situ $\delta^{34}S$ data from Mars at Gale crater display a ~75‰ range that has been attributed to an abiotic mechanism. Yet biogeochemical studies of ancient environments on Earth generally interpret $\delta^{34}S$ fractionations > 21‰ as indicative of a biological origin, and studies of $\delta^{34}S$ at analog impact crater lakes on Earth have followed the same approach. We performed analyses (including $\delta^{34}S$, TOC wt%, and SEM imaging) on multiple lithologies from the Nördlinger Ries impact crater, focusing on hydrothermally altered impact breccias and associated sedimentary lake-fill sequences to determine whether the $\delta^{34}S$ properties define a biosignature. The differences in $\delta^{34}S$ between the host lithologies may have resulted from thermochemical sulfate reduction, microbial sulfate reduction, hydrothermal equilibrium fractionation, or any combination thereof. Despite abundant samples and instrumental

precision currently exclusive to Earth-bound analyses, assertions of biogenicity from $\delta^{34}S$ variations > 21‰ at the Miocene Ries impact crater are tenuous. This discourages the use of $\delta^{34}S$ as a biosignature in similar environments without independent checks that include the full geologic, biogeochemical, and textural context, as well as a comprehensive acknowledgment of alternative hypotheses.

Introduction

Impact crater lakes may have housed the earliest (> 3.5 Ga) habitable environments on Earth and Mars. In these locations, impact-induced hydrothermal activity would have provided heat in opposition to a faint young Sun and could have sourced compounds thought necessary for prebiotic synthesis of life's building blocks as well as the bioessential elements needed to sustain life (Abramov and Kring, 2005; Cockell et al., 2020; Farmer, 2000; Kacar et al., 2020; Kring, 2000; Osinski et al., 2013). These attributes make impact craters appealing targets for origin-of-life studies and the search for extinct life on Mars. In fact, impact craters have been the sites of multiple surface exploration missions, including the landing of the Perseverance rover in Jezero crater (Goudge et al., 2015; Grotzinger et al., 2015; Osinski et al., 2020; Mangold et al., 2021).

The collective understanding of nutrient cycling in ancient crater lakes has long relied on studies of geochemical proxies at well-preserved analog environments on Earth's surface (Hays et al., 2017; Léveillé, 2010; Osinski et al., 2020). One such proxy is the ratio of the two most abundant stable isotopes of sulfur (i.e., $\delta^{34}S = [(^{34}S/^{32}S)_{sample}/(^{34}S/^{32}S)_{Vienna-}$

$_{\text{Canyon Diablo Troilite}} - 1] \times 1000$), which has the potential to illuminate both internal and surface processes on Earth and Mars (Nielsen et al., 1991; Canfield, 2001; Franz et al., 2019; King and McLennan, 2010). Sulfur has an expanded valence octet that allows for a redox continuum, with oxidation states ranging from -2 to +6. Stable S-isotope ratios can be fractionated during chemical exchanges across this range by kinetic and equilibrium reactions linked to both abiotic and biological processes (Canfield, 2001; Baune and Böttcher, 2010; Sakai, 1957; Seal, 2006; Surkov et al., 2012; Thode et al., 1961).

Mars can be considered a S-rich planet, evidently possessing a higher relative surface abundance of S than present-day Earth (Clark et al., 1982; Franz et al., 2019). Sulfur has been examined on the Martian surface in a multitude of forms, including Fe-sulfides (e.g., pyrrhotite [$Fe_{1-x}S$] and pyrite [FeS_2]); Ca/ Mg/Fe-sulfates, such as anhydrite [$CaSO_4$]; and the Fe-hydroxide-sulfate mineral jarosite [$KFe_3(SO_4)_2(OH)_6$] (Franz et al., 2019; Squyres et al., 2004; Vaniman et al., 2014). The reference base of the stable S-isotope system, Vienna-Canyon Diablo Troilite ([VCDT]: $\delta^{34}S = 0‰$, $^{34}S/^{32}S = 441.626 \pm 0.039 \times 10^{-4}$; Ding et al., 2001), presents a practical comparative scale for both Mars and Earth, because it reflects the S isotope composition of our solar system's primordial terrestrial material (Hoefs, 2021; Sharp, 2017; Thode et al., 1961). Sulfur isotope ratios in Martian crater settings therefore have great potential to provide novel insights into past environmental conditions, including the presence of life. However, before this geochemical signature can be applied as a potential proxy for biological activity, it is imperative to develop a more thorough understanding of the range of possible S-isotope-fractionating processes that can operate in impact craters.

The complexity surrounding S fractionation mechanisms has provided the basis of multiple recent studies investigating S cycling in ancient impact craters (e.g., Kring et al., 2021; Schaefer et al., 2020, 2022). Hydrothermal mineral assemblages from borehole samples of Chicxulub crater's peak rim display anhydrite and pyrite with $\Delta^{34}S_{sulfate\text{-}sulfide}$ values of 25‰ to 54‰ (Kring et al., 2021). There, consistent visual evidence of pyrite framboids bolsters an interpretation of microbial sulfate reduction [MSR] as the primary fractionation mechanism (Kring et al., 2021). At Haughton crater in the Canadian High Arctic, a $\Delta^{34}S_{sulfate\text{-}sulfide}$ of 44‰ was observed between gypsum and pyrite, along with a $\Delta^{34}S_{sulfate\text{-}sulfide}$ of 71‰ between gypsum and marcasite [orthorhombic FeS_2]. Due to the magnitude of these differences, these data have also been interpreted as MSR (Parnell et al., 2010). However, there is a lack of reported sedimentary framboidal pyrite, the formation of which is often attributed to high rates of dissimilatory sulfate reduction associated with organic matter degradation (Passier et al., 1999; Rickard, 2021). This form notably differs from euhedral pyrite, which can form in sediments via lower microbial process rates, overgrowths on framboids (Passier et al., 1999), recrystallization (Liaghati et al., 2005), or a combination thereof. *In situ* analyses of S isotopes have been made by the Mars Science Laboratory's [MSL] Sample Analysis at Mars [SAM] instrument suite at Gale crater (Franz et al., 2017). The reported values span from -47 (± 14)‰ to 28 (± 7)‰, which is noted as similar to the terrestrial range observed on Earth (Franz et al., 2017; Hoefs, 2021). A multi-step abiotic fractionation mechanism was proposed, which included atmospheric oxidation and ultraviolet photolysis of volcanogenic S, followed by hydrothermal equilibrium fractionation (Franz et al., 2017). These contradictory

interpretations—specifically, thermophilic MSR at impact craters on Earth versus a set of abiotic reactions for the first *in situ* surface $\delta^{34}S$ analyses from Mars—call for additional understanding of sulfur isotope ratios and related controls at analog sites.

To shed further light on these contrasting studies and their respective implications, we have performed a study of multi-phase sulfur speciation and isotope partitioning at the Ries crater in southern Germany. Our aim is to determine if and when large S isotope fractionation events in crater lake systems are definitively linked to life. Accordingly, we explore the three plausible mechanisms known to produce significant $\delta^{34}S$ variation in crater settings: MSR, thermochemical sulfate reduction [TSR], and hydrothermal equilibrium fractionation.

Geologic Setting

The Nördlinger Ries, located 110 km northwest of Munich, Germany, is one of the best-studied craters on Earth (**Fig. 1.1**) (Arp et al., 2013a; Graup, 1999; Newsom et al., 1990; Pohl et al., 1977; Stöffler et al., 2013). It is ~24 km in diameter and was generated at 14.7495 ± 0.016 Ma by the impact of a 1.3 ± 0.2 km-diameter meteorite (Artemieva et al., 2013; Di Vincenzo, 2022). The target rocks included Mesozoic sedimentary strata and Variscan crystalline basement rocks (Pohl et al., 1977; Stöffler et al., 2013; Sturm et al.,

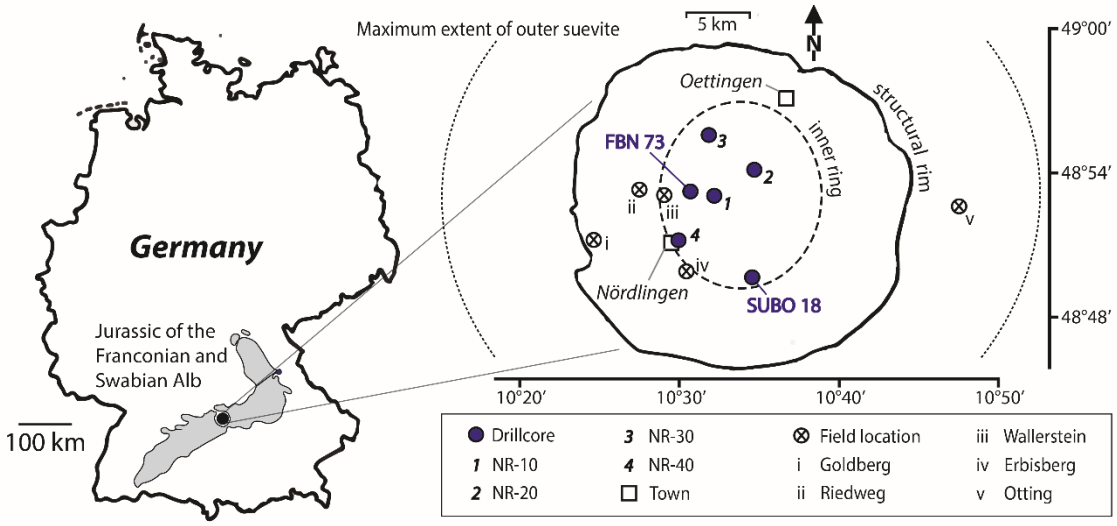

Figure 1.1 Geographical context for Ries crater, including the locations of all drill core and field sites sampled or referenced in this study. Adapted from Arp et al. (2013a) and Stöffler et al. (2013).

2013). The Ries crater is the type locality for suevite, an impact melt-bearing breccia now identified at several terrestrial crater sites where crystalline rocks compose all or part of the surface target (Osinski et al., 2016; Stöffler et al., 2013). It is considered a Mars analog because—like many craters on Mars—it possesses a well-preserved dual-layer ejecta [DLE] blanket with a rampart structure (Barlow, 2005; Hörz et al., 1983; Kenkmann and Schönian, 2006; Pohl et al., 1977; Sturm et al., 2013; Viola et al., 2017). The lower ejecta layer is a continuous mixture of sedimentary and crystalline basement rocks termed "Bunte Breccia" (Hörz et al., 1983; Pohl et al., 1977). The upper ejecta layer ["outer suevite"] comprises discontinuous patches of suevite, and suevite also occurs within the central crater basin as a continuous breccia lens ["crater suevite"] (Pohl et al., 1977; Stöffler et al., 2013; von Engelhardt, 1990; von Engelhardt, 1997). Comprehensive reviews of crater formation mechanisms can be found in Artemieva et al. (2013) and Stöffler et al. (2013). Of direct astrobiological interest is the impact-induced formation of a hydrothermal crater lake system that consequentially interacted with the DLE for roughly 10^4 to 10^6 years (Arp

et al., 2013b; Caudill et al., 2021; Muttik et al., 2010; Newsom et al., 1986; Osinksi, 2005; Sapers et al., 2017).

The Ries Crater Paleolake

A closed-basin lake formed in the Ries basin shortly after the impact and existed for 1–2 Myr (Arp et al., 2021a; Füchtbauer et al., 1977; Jankowski, 1977; Montano et al., 2021). Successive weathering of suevite followed by Bunte Breccia, in combination with diminishing hydrothermal activity, caused multiple distinct shifts in the lake's chemistry through time (Arp et al., 2013a). These shifts correlate approximately with the four stratigraphic units established by Füchtbauer et al. (1977) (**Fig. 1.2**). The first waters in the basin were transient playas that deposited sandstones and reworked suevite, which are now referred to as the basal member or unit A (Füchtbauer et al., 1977). This interval was followed by the formation of a permanent, eutrophic, high-pH alkali-saline lake that deposited the bituminous shales and laminated marls of the organic-rich laminite member (unit B) (Füchtbauer et al., 1977; Arp et al., 2013a; Rullkötter et al., 1990; Stüeken, Tino et al., 2020). Changes in the dominant weathering and alteration source from suevite to Bunte Breccia led to a shift toward saline waters with circum-neutral pH and deposition of calcareous claystones of the marl member (unit C) (Arp et al., 2013a). Then, a change to alternating hyposaline and hypersaline conditions led to deposition of the clay member (unit D) (Arp, 2006; Arp et al., 2013a; Füchtbauer et al., 1977). The youngest preserved lake sediments still show evidence of hydrologically closed conditions with no evidence for an outlet (Arp et al., 2017). Eventually, the lake basin filled with sediment, and lake waters permanently disappeared.

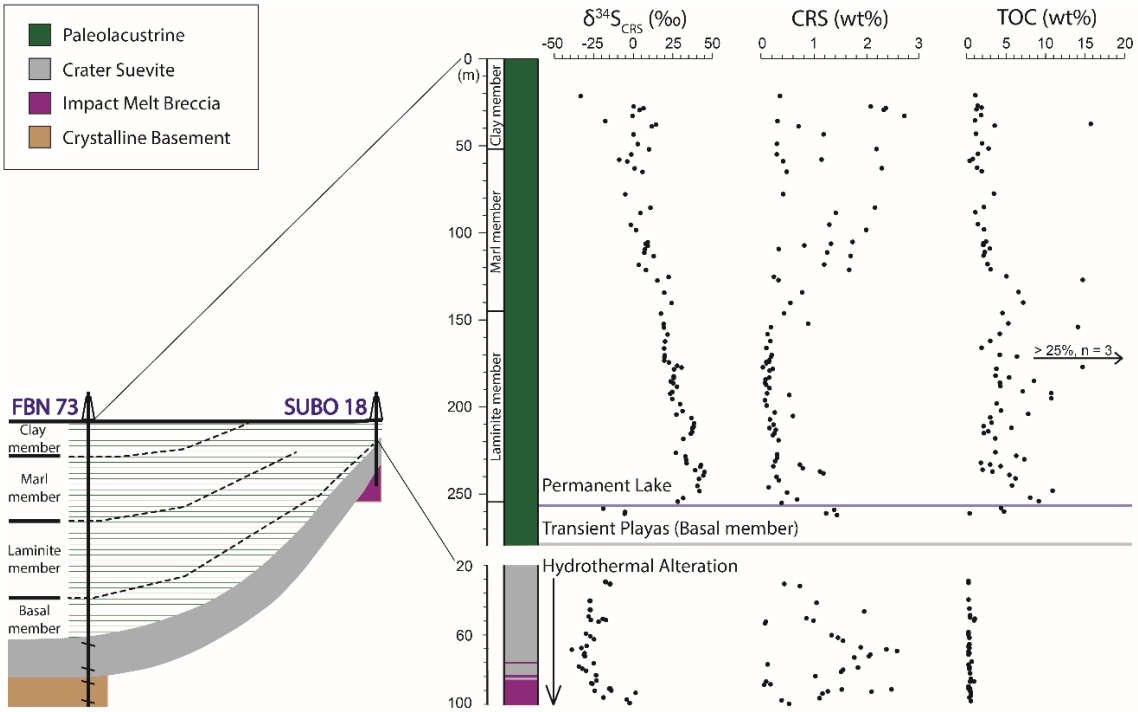

Figure 1.2 Stratigraphic trends of the FBN 73 and SUBO 18 drill cores, connected to a simplified diagram of their relative positions within Ries crater's concave structure. The depths used for bounding the four sedimentary units (members) of FBN 73 are from Füchtbauer et al. (1977), and the dashed stratigraphic correlation markers are adapted from Arp et al. (2021). Lithostratigraphy of SUBO 18 is adapted from Reimold et al. (2012). Angular lines near the base of the visual representation for FBN 73 represent breaks in stratigraphy and thus a deviation from relative scale at depths below 314.3 meters.

Impact-induced Hydrothermal Activity

Hydrothermal alteration was pervasive within the central basin, as indicated by the complete replacement of impact-generated glasses in crater suevite (Osinski, 2005; Stöffler, 1977). Melt-rich layers within suevite sequences from multiple drill cores point to temperatures of ~600°C for the first post-impact materials that settled in the basin (von Engelhardt, 1990). The earliest sustained hydrothermal fluids were likely derived from surface meteoric waters and groundwaters from the surrounding country rock. These fluids ranged from 200–300°C as indicated by K-metasomatism and chloritization in crater suevite (Osinski, 2005; Osinski et al., 2004). The second or main stage of alteration

occurred via weakly alkaline fluids as temperatures decreased through the 200–100°C window and was characterized by intermediate argillic alteration and zeolitization products within crater suevite (Osinski, 2005). Muttik et al. (2010) used stable oxygen [$\delta^{18}O$] and hydrogen [δD] isotope data from crater suevite to constrain the temperatures of the final alteration stage to 43–112°C. Temperature increased monotonously with depth in association with convective circulation, and the coolest stage was likely the longest-lived (Muttik et al., 2010). Quantitative constraints on the duration and intensity of hydrothermal activity as it relates to the paleolake waters are presently limited. Stratigraphically, hydrothermal activity occurred throughout the basal member and extended into the laminite member (Arp et al. 2013b). During deposition of the laminite member, Ca-bearing fluids of both hydrothermal and non-hydrothermal origin were locally introduced to alkaline waters, leading to the formation of carbonate spring mounds and travertines (Arp, 1995; Arp et al., 2013b). The observation of streamer carbonates in the Erbisberg spring mound (coordinates: 48°49′52.34″N, 10°30′42.56″E) indicate that 70°C waters were still emerging from the system several 100 kyr after impact and that hydrothermal effects extended at least to the crater's inner ring (Arp et al., 2013b). While the subsurface impact breccias faced significant exposure to hydrothermal fluid temperatures above the current known limits of life (~121°C), there is no reason to assume that the earliest lake waters, or the sediments deposited from them, ever existed at uninhabitably high temperatures. Such high temperatures would require elevated pressure to maintain water in a liquid state, which is not plausible for this lake system in the Miocene. Given the lateral and vertical extent of

hydrothermal activity, drill cores and field sites are highly complementary at Ries crater. This study therefore includes samples from both.

Samples and Methods

Sample Collection

We analyzed the research drill core Nördlingen 1973 [FBN 73], which contains one of the most extensive paleolake sedimentary sections among the Ries drill cores and has been the subject of multiple geochemical studies, which provide valuable context for our $\delta^{34}S$ work (Füchtbauer et al., 1977; Muttik et al., 2010, 2011; Osinski, 2005; Stüeken, Tino et al., 2020; von Engelhardt, 1997). For our examination of the paleolake sediments, 81 samples were selected across 241 m of stratigraphy (**Fig. 1.2**; 21–262 m depth in the core or 403–164 m above modern sea level [a.s.l.]). To demonstrate that the paleolacustrine $\delta^{34}S$ data collected from the FBN 73 drill core are representative for the whole basin, 27 samples from four exploratory Nördlinger Ries [NR] wells were included (**Fig. 1.3**; NR-10, NR-20, NR-30, and NR-40 drilled by BEB Erdgas und Erdöl GmbH in the early 1980s; permission for use was provided by ExxonMobil; Rullkötter et al., 1990; Barakat et al., 2012; Barakat et al., 2013). All lacustrine sediment samples in this study have undergone minimal post-depositional geothermal heating. Vitrinite reflectance data from FBN 73 samples suggest a maximum temperature of 60°C (Wolf, 1977). Subsequent biomarker studies of NR cores pointed similarly to very minor thermal overprints (Barakat and Rullkötter, 1995).

We assessed the S chemistry resulting from hydrothermal alteration within the impact breccia by selecting 33 samples spanning 71 m of stratigraphy (**Fig. 1.2**; 29–100 m core depth, 315–386 m a.s.l.) from the Enkingen [SUBO 18] core. SUBO 18 contains 21 meters of lacustrine sedimentary rock overlying ~65 m of crater suevite, followed by ~15 m of impact melt breccia (i.e., melt content > 50%). This is the only coherent sequence of impact melt breccia encountered in a Ries crater drill core thus far (Pohl et al., 2010; Reimold et al., 2012; Reimold et al., 2013).

Field sampling was included to complement the drill core analyses, with the hope of elucidating the S composition of both the water column of the alkaline lake and the subaerial weathering environment that fed into the basin at that time. Eight samples were collected from two carbonate mounds—Wallerstein travertine (n = 2, 48°53′20.3″N, 10°28′28.9″E) and Goldberg spring mound (n = 6, 48°51′40.7″N, 10°25′19.8″E)—for analysis of carbonate-associated sulfate [CAS] content as a proxy for the SO_4^{2-} composition of the water column during the alkaline lake phase (**Fig. 1.4**). The Wallerstein samples are from the base of that mound, which is composed of non-fossiliferous carbonates with intercalations of brine shrimp fecal pellets (Pache et al., 2001), signifying that they were deposited synchronously to the pellet-rich lower part of the laminite member (Jankowski, 1977) and formed before the Goldberg mound samples. The sampled portions of the Goldberg and Wallerstein mounds in this study were formed subaqueously (i.e., in a mixing zone of sub-lacustrine spring and alkaline lake water; Arp, 1995; Pache et al., 2001). Multi-isotope ($^{87}Sr/^{86}Sr$, $\delta^{13}C$, $\delta^{18}O$) constraints on mixing ratios at Ries spring precipitation zones suggest that the majority of SO_4^{2-} available for incorporation as CAS was derived

from the lake water (Pache et al., 2001). To evaluate possible S contributions to the inner basin from the surficial weathering of outer suevite, three samples of outer suevite were collected from Riedweg (n = 1, 48°54′54.4″N, 10°26′39.8″E) and Otting (n = 2, 48°52′24.1″N, 10°47′55.0″E).

Geochemical Analyses

The outer rims of all drill core and field samples were trimmed with either a rock saw or manually operated rock chipper, depending on sample hardness. The resulting interiors were hammered into subcentimeter-sized chips, rinsed with deionized H_2O, and dehydrated at 50°C for a minimum of 48 hours. The rock chips were then pulverized in a ball mill.

Total organic carbon [TOC], total inorganic carbon [TIC], total sulfur [TS], chromium-reducible sulfide [CRS], and CAS data for all FBN 73, SUBO 18, and field samples were collected in the Lyons Biogeochemistry Laboratory at the University of California, Riverside [UCR]. Total Carbon [TC], TIC, and TS were measured via combustion on an Eltra CS-500 carbon-sulfur analyzer, all with precision better than ±0.1 wt%. TOC was then calculated as the difference between measured TC and TIC.

The chromium reduction method (e.g., Canfield et al., 1986) was used to assess S present in sulfide minerals. Specifically, bulk sample powders were mixed with a 1 M $CrCl_2$ (acidified to 0.5 M HCl) solution under a stream of N_2 gas (i.e., anoxic conditions) and brought to a boil to evolve hydrogen sulfide [H_2S] from present CRS phases. That H_2S was trapped in a silver nitrate solution as silver sulfide [Ag_2S], which was then quantified gravimetrically and converted to wt% CRS in the sample, assuming all H_2S precipitated as

Ag_2S. For carbonate-rich samples (TIC wt% > 11), powders were decarbonated with 1N HCl prior to chromium reduction. In studies of ancient sediments, CRS is typically dominated by sulfur hosted in pyrite. Consistent with these past studies, previously published petrographic analyses of SUBO 18 confirm pyrite as the predominant S phase in the Ries impact breccia (Reimold et al., 2012; Reimold et al., 2013). Standard deviations [σ] for CRS wt%, as measured from repeat (n = 6) analyses of a randomly selected SUBO 18 sample and repeat analyses (n = 7) of a randomly selected FBN 73 sample, were σ = 0.03 wt% and σ = 0.07 wt%, respectively. Sulfur isotope ratio ($\delta^{34}S$) measurements of those same sets showed σ = 0.23‰ (FBN 73) and σ = 0.16‰ (SUBO 18).

To extract CAS, carbonate samples were rinsed in a 5% NaCl solution for three consecutive nights (the solution being refreshed each day) to remove all easily soluble sulfates. This step was followed by two consecutive deionized H_2O rinses of 24 hours each. To remove organic-S and trace sulfides, the samples were then treated with a 30% H_2O_2 solution, the volume of which was calculated to be ~100x in excess of the organic content as inferred from TOC wt% measurements (assuming a simplified CH_2O stoichiometry). This step was followed by two rinses with deionized H_2O of 24 hours each. The purified carbonates were then acidified with a 4N HCl solution with 5 wt% stannous chloride [$SnCl_2$] until effervescence ceased. Insoluble materials were removed by filtration, followed by addition of a saturated barium chloride [$BaCl_2$] solution to quantitatively precipitate the SO_4^{2-} as $BaSO_4$. The volume of added $BaCl_2$ was calculated to be roughly 40x in excess of the CAS as estimated by conservatively assuming that the measured wt% TS was entirely CAS. CAS concentrations (mg/kg) were then calculated via gravimetry of

the filtered and dried $BaSO_4$. Triplicate analyses of a randomly selected carbonate sample yielded a coefficient of variation [CV; ratio of σ to the mean] = 0.1% for CAS contents, and $\delta^{34}S$ values for that same triplicate agreed to within 0.1‰.

Sulfur isotope ratios for the CRS and CAS were measured at UCR using a Thermo Scientific Delta V Plus continuous-flow stable isotope ratio mass spectrometer [IRMS]. Sulfur from Ag_2S and $BaSO_4$ was converted to SO_2 and separated via gas chromatography [GC] on a Costech ECS 4010, with gas flow to the IRMS controlled by a Thermo Scientific ConFlo III open split interface. For $\delta^{34}S_{CRS}$, samples were bracketed by the international reference standards IAEA-S1, -S2, and -S3. For $\delta^{34}S_{CAS}$, samples were bracketed by IAEA-SO5, -SO6, and NBS-127 (for the $\delta^{34}S$ values of these standards, see Appendix 1 of Sharp, 2017). Precision for all standards in all runs was better than σ = 0.3‰.

Bulk sediment (i.e., including all S in a given sample) and kerogen enrichments of NR-10, NR-20, NR-30, and NR-40 were analyzed at ICBM Oldenburg for TC and TS using a Carlo Erba EA 1108 elemental analyzer. Carbonate was removed with dilute HCl, and TOC was determined coulometrically using a Ströhlein-type 702 Coulomat. TIC contents were obtained from the difference between TC and TOC. The kerogen fraction was separated as described in Barakat and Rullkötter (1995), where solvent-extracted residues are demineralized with a HF:HCl (1:1) treatment followed by additional Soxhlet and ultrasonic extractions. Bulk sediment and kerogen samples were analyzed for $\delta^{34}S$ using combustion-isotope-ratio-monitoring mass spectrometry [C-irmMS]—specifically, a Finnigan MAT 252 mass spectrometer coupled to a Carlo Erba EA 1108 elemental analyzer via a Finnigan MAT ConFlo II open split interface, as described in detail by

Böttcher et al. (1998) and Böttcher and Schnetger (2004). IAEA-S1, -S2, and -S3, as well as NBS 127, were used to calibrate the $\delta^{34}S$ values to VCDT. Precision for the measurements was better than $\sigma = 0.2‰$. Isotope values reported in "‰" are equivalent to "mUr" (milli-Urey; Brand and Coplen, 2012).

Backscattered electron [BSE] imaging (**Fig. 1.6**) was performed in the Brounce Geochemistry Laboratory at UCR using a JEOL JCM-7000 benchtop scanning electron microscope [SEM]. A combination of manual observations and montage imaging was used to examine the entirety of polished surfaces.

Results

Paleolake Sediments

FBN 73

Starting from the lowest sample depth (261.5 m), $\delta^{34}S_{CRS}$ values of sedimentary rocks from FBN 73 (**Fig. 1.2, Table 1.1**) are uniformly negative in the basal member (mean = -9.9‰, n = 3, $\sigma = 6.5‰$, 261. 5 m - 258.5 m). Moving upcore into the laminite member, values shift from -19.0‰ at 258.5 m to 28.1‰ at 254.5 m, and reach a maximum of 45.1‰ at 237.5 m within an interval characterized by high values (mean = 38.0‰, n = 19, $\sigma =$ 4.6‰) spanning from 248.5 m to 206.5 m. Values generally decrease over the remainder

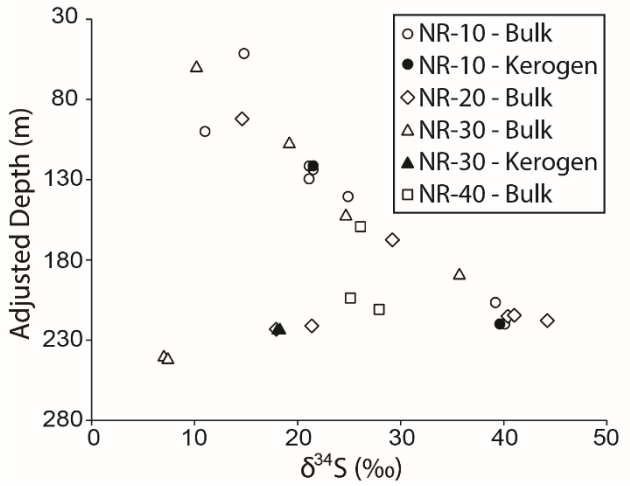

Figure 1.3 $\delta^{34}S$ data from bulk and kerogen analyses across the sedimentary paleolake intervals of four drill cores (NR-10, NR-20, NR-30, and NR-40) from within the inner ring of Ries crater. Sample depths were adjusted based on vertical trends, using the unadjusted NR-30 sample depths as a fixed reference point.

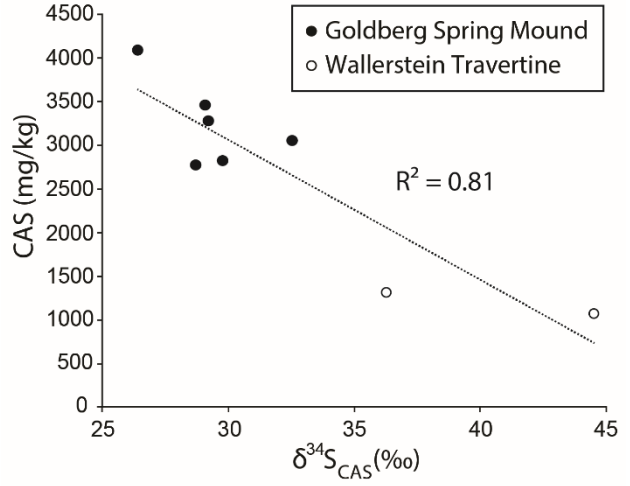

Figure 1.4 CAS (mg/kg) vs. $\delta^{34}S_{CAS}$ (‰) scatterplot composed of data generated from the Goldberg and Wallerstein carbonate mounds. The negative relationship with a strong coefficient of determination indicates that the highest $\delta^{34}S_{CAS}$ values were generated

of the laminite member, with the unit reaching its minimum of 17.5‰ just before the transition into the marl member at 145 m depth. This trend of decreasing values continues throughout the marl (mean = 6.9‰, n = 23, σ = 8.3‰, 140.5 m - 52.1 m) and clay (mean = -1.2‰, n = 10, σ = 13.5‰, 49.1 m - 21.55 m) members but the data have a larger spread.

CRS contents (dominantly pyrite; see Samples and Methods) vary from 0.02 wt% to 5.65 wt%. Values throughout the entire laminite member (mean = 0.30 wt%, n = 48, σ = 0.27 wt%) are generally lower than those within the other units (basal member [mean = 1.35 wt%, n = 3, σ = 0.09 wt%], marl member [mean = 1.09 wt%, n = 23, σ = 0.67 wt%], and clay member [mean = 2.77 wt%, n = 10, σ = 1.57 wt%]). Coefficients of determination [R^2] via

linear regression show weak or no relationship between CRS wt% and $\delta^{34}S_{CRS}$ ($R^2 = 0.15$ for all samples, and $R^2 \leq 0.35$ in all individual stratigraphic units). TOC contents follow the trends reported in Förstner (1977) and Stüeken, Tino et al. (2020). The basal, laminite, and marl members display no discernable relationship between wt% CRS and TOC ($R^2 < 0.04$ in all cases), but the clay member shows a positive relationship with an R^2 of 0.79.

NR-10, NR-20, NR-30, and NR-40

Data from the four exploratory wells (**Fig. 1.3**, **Table 1.2**) allow for a wider breadth of $\delta^{34}S$ examination in terms of both sedimentary host phases and spatial distributions within the lake basin. Bulk and kerogen $\delta^{34}S$ data ($\delta^{34}S_{Bulk}$ and $\delta^{34}S_{Kerogen}$) show trends that are similar, in both magnitude and pattern, to the $\delta^{34}S_{CRS}$ values from FBN 73. For any given sample where both $\delta^{34}S_{Bulk}$ and $\delta^{34}S_{Kerogen}$ were measured (n = 3), the differences were minor (≤ 0.5‰) between the two measured phases. Viewed within this context, our bulk measurements indicate that $\delta^{34}S$ is uniformly elevated in the lower laminite member, regardless of which S-bearing phase dominates the isotopic mass balance (e.g., kerogen or pyrite) within a given sample. Moving up core, the combined data series rises from a minimum $\delta^{34}S_{Bulk}$ of 7.4‰ to a maximum $\delta^{34}S_{Bulk}$ of 44.2‰. There is a consistent up-core decrease over the remainder of the sample set, with data from the four uppermost adjusted sample depths (using NR-30 as a zero-reference line) falling below 15‰ (mean = 12.65‰, n = 4, 100.0 m - 51.5 m).

Table 1.1 Geochemical data ($\delta^{34}S_{CRS}$, CRS, TOC) from drill cores FBN 73 and SUBO 18. Reproducibilities (1SD) are 0.25‰ or better for $\delta^{34}S_{CRS}$, 0.07 wt% or better for CRS, and 0.1 wt% for TOC. * = not measured, n.d. = not detected

Depth (m)	Notes	$\delta^{34}S_{CRS}$ (‰)	CRS (wt%)	TOC (wt%)
FBN 73 (Nördlingen 1973 research drilling)				
Claystone member	Centimeter-scale laminated mudstone, dark gray, carbonaceous intercalations			
21.55 (403.5 m a.s.l.)		-33.3	0.35	1.0
27.55		0.2	2.08	1.2
28.55		6.4	2.37	1.7
29.55		4.0	2.33	1.1
32.95		-0.5	2.72	1.7
35.95		-17.7	0.30	0.9
37.95	Coal seam	14.4	5.65	15.6
38.95		11.7	0.70	3.4
43.575		0.2	1.18	1.0
49.1		2.8	0.29	1.8

Marl member	Calcareous pale gray mudstone, massive to centimeter-scale bedding			
52.1		10.0	2.19	2.6
55.1		-1.3	0.28	1.3
58.1		-8.9	1.14	0.6
59.1		-3.8	0.40	0.2
63.1		0.8	2.29	1.2
65.1		5.8	0.47	1.8
78		-5.1	0.41	3.3
85.7		10.9	2.16	2.0
88.7		4.5	1.41	1.0
95.5		-1.6	1.29	1.3
98.5		1.7	1.99	2.0
105.5		9.1	1.73	2.3
106.5		7.7	1.32	2.0
107.5		9.2	0.81	2.0
109.5		7.5	0.32	2.8
111.5		7.0	1.25	2.2

113.5		13.0	1.69	2.0
118.5		3.5	1.19	2.5
121.5		8.1	1.67	2.9
125.5		22.4	0.23	4.9
127.5	Bituminous	15.2	0.31	14.6
134.5		19.6	0.77	6.4
140.5		24.2	0.54	7.0
Laminite member	Millimeter-scale laminated mudstone, calcareous to bituminous			
146.5		17.5	0.42	4.4
152.5		19.2	0.88	5.1
154.5	Bituminous	19.4	0.17	14.0
158.5		21.7	0.11	4.0
162.5		20.1	0.16	2.8
166.5		19.5	0.08	1.7
170.5		19.8	0.19	4.1
171.5		19.7	0.17	6.2
173.5	Bituminous	19.6	0.14	25.6

174.5	Bituminous	22.5	0.08	33.3
176.5	Bituminous	27.8	0.02	34.7
177.5	Bituminous	30.6	0.20	14.6
178.5		25.8	0.14	3.6
182.5		25.6	0.14	3.5
183.5		25.6	0.07	5.2
185.5	Bituminous	23.6	0.06	8.4
186.5	Bituminous	25.4	0.08	4.1
188.5	Bituminous	27.7	0.14	4.1
191.5	Bituminous	24.7	0.10	7.0
192.5	Bituminous	23.4	0.52	10.6
195.5	Bituminous	24.7	0.06	10.6
198.5		29.6	0.09	3.7
202.5		31.2	0.24	4.2
204.5	Bituminous	27.3	0.59	7.7
206.5		36.8	0.15	2.8
209.5		38.6	0.22	3.0

211.5		38.2	0.14	2.0
212.5		37.3	0.26	5.5
214.5		37.2	0.24	2.6
215.5		36.5	0.21	2.0
218.5		31.7	0.32	3.5
226.5		26.9	0.29	3.5
228.5	Bituminous	33.1	0.29	6.1
230.5	Bituminous	33.5	0.25	7.2
232.5		33.8	0.72	1.6
233.5		42.8	0.22	2.8
234.5		42.5	0.78	4.2
236.5		39.2	1.11	1.9
237.5		45.1	1.17	3.1
239.5	Bituminous	44.3	0.28	5.3
241.5	Bituminous	41.6	0.32	6.0
245.5	Bituminous	40.6	0.13	5.6
248.5	Bituminous	41.9	0.48	10.7

252.5	Bituminous	31.6	0.67	7.9
254.5		28.1	0.38	9.0
Basal member	Sandstone with interlaminated calcareous marlstone			
258.5	Marlstone	-19.0	1.38	4.2
260.5	Marlstone	-5.2	1.22	4.6
261.5	Marlstone	-5.5	1.43	0.2
SUBO 18 (Enkingen drilling)				
Crater Suevite	Polymict breccia with groundmass containing clastic and melt particles			
29.53 (385.47 m a.s.l.)		-10.0	0.42	< 0.1
30.75		-7.1	0.72	< 0.1
40.46		-19.8	1.04	< 0.1
45.57		-19.7	1.94	0.1
49.50		-20.7	0.85	0.2
50.87		-11.8	0.98	0.2
51.50		-19.3	0.07	0.8
52.48		-14.4	0.06	0.7
59.33		-22.4	1.32	< 0.1

60.79		-19.7	1.45	< 0.1
62.58		-17.3	1.54	0.1
66.42		-22.0	1.88	0.1
67.61		-25.3	2.37	< 0.1
68.59		-31.4	2.57	0.1
70.61		-23.3	2.06	< 0.1
71.61		-23.7	2.03	0.1
72.37		-23.1	1.76	< 0.1
76.44	Impact melt breccia	-17.5	0.11	0.4
78.23		-26.9	1.82	< 0.1
79.54		-24.7	1.54	0.1
80.73		-22.3	1.50	0.1
Impact Melt Breccia	Melt content > 50%, relatively poor in suevite groundmass			
83.29		-16.0	1.02	0.2
86.40		-15.7	0.08	0.3
87.95		-19.0	0.16	0.7
88.16		-18.3	0.04	0.2

90.93	-6.9	2.46	< 0.1
91.04	-7.7	1.52	< 0.1
92.11	-6.3	1.25	0.2
92.23	-16.9	2.09	< 0.1
93.43	9.1	1.15	0.2
94.28	*	n.d.	0.3
96.11	-11.3	1.10	0.3
97.28	3.5	0.37	0.1
99.35	5.3	0.51	0.3

Table 1.2 Geochemical data ($\delta^{34}S_{Bulk}$, $\delta^{34}S_{Kerogen}$, TOC, TIC, TS) from NR-10, NR-20, NR-30, NR-40. Reproducibilities (1SD) are 0.25‰ or better for $\delta^{34}S_{Bulk}$ and $\delta^{34}S_{Kerogen}$, and 0.1 wt% or better for TOC, TIC, and TS. * = not measured

Adjusted Depth (m)	Unadjusted Depth (m)	Drill core	$\delta^{34}S_{Bulk}$ (‰)	TS (wt%)	TOC (wt%)	TIC (wt%)
Bulk samples						
51.5	81.5	NR-10	14.8	2.6	2.5	0.4
59.6	98.1	NR-20	10.2	1.5	2.9	0.4
92.7	92.7	NR-30	14.6	1.1	2.1	0.6
100	130	NR-10	11.0	2.0	7.2	1.2
107.2	145.7	NR-20	19.2	1.3	1.7	0.5
121.5	151.5	NR-10	21.3	2.1	12.3	1.5
123.8	153.8	NR-10	21.5	1.4	15	1.8
129.5	159.5	NR-10	21.1	1.7	11.9	1.5
140.5	170.5	NR-10	24.9	1.1	25.5	3.1
152	190.5	NR-20	24.7	1.4	7.7	1.2
159.3	46.8	NR-40	26.1	1.2	1.9	0.6
167.8	167.8	NR-30	29.2	2.2	7.8	1.2
189	227.5	NR-20	35.7	0.5	3.4	0.8

203.8	91.3	NR-40	25.1	2.2	4.6	0.9
206.5	236.5	NR-10	39.2	2.8	3.5	0.7
210.9	98.4	NR-40	27.9	3.1	7.7	1.1
214	214	NR-30	41.0	1.5	3.7	0.9
215.1	215.1	NR-30	40.4	3.6	10.3	1.3
218	218	NR-30	44.2	2.3	5.8	1.2
220	250	NR-10	40.1	3.6	14.4	1.8
221.4	221.4	NR-30	21.4	2.7	2.8	0.7
222.9	222.9	NR-30	18.0	3.8	8.4	1.0
240	278.5	NR-20	7.0	5.1	4.5	0.6
241.5	280	NR-20	7.4	3.3	4.0	0.9
Kerogen extracts			$\delta^{34}S_{Kerogen}$ (‰)			
121.5	151.5	NR-10	21.5	*	*	*
220	250	NR-10	39.6	*	*	*
222.9	222.9	NR-30	18.1	*	*	*

Table 1.3 Geochemical data ($\delta^{34}S_{CAS,}$ CAS, TIC, TOC, TS, CRS) for all field samples. Reproducibilities (1SD) are 0.25‰ or better for $\delta^{34}S_{CAS}$, 27 mg/kg (n = 3) for CAS, 0.07 wt% or better for CRS, and 0.1 wt% for TIC, TOC, and TS. * = not measured, n.d. = not detected

Identifier	$\delta^{34}S_{CAS}$ (‰)	CAS (mg/kg)	TIC (wt%)	TOC (wt%)	TS (wt%)	CRS (wt%)
Carbonate Mounds						
Goldberg 1	29.2	3280	11.7	0.2	0.2	0.001
Goldberg 2	29.8	2825	11.8	0.2	0.1	0.003
Goldberg 3	26.4	4091	11.8	< 0.1	0.2	0.002
Goldberg 4	29.1	3460	11.3	0.5	0.1	0.001
Goldberg 5	32.5	3055	11.8	0.1	0.1	0.001
Goldberg 6	28.7	2775	11.6	0.3	0.1	n.d.
Wallerstein 1	44.5	1075	11.7	0.2	< 0.1	0.002
Wallerstein 2	36.3	1316	11.7	0.2	0.1	0.001
Outer Suevite						
Otting 1	*	*	≤ 0.1	≤ 0.1	< 0.1	0.001
Otting 2	*	*	≤ 0.1	≤ 0.1	< 0.1	n.d.
Riedweg 1	*	*	≤ 0.1	≤ 0.1	< 0.1	n.d.

Carbonate Mounds

$\delta^{34}S_{CAS}$ values of the carbonates (**Fig. 1.4, Table 1.3**) show a range from 26.4‰ to 44.5‰ (mean = 32.1‰, n = 8, σ = 5.5‰). Analyses from Wallerstein travertine ($\delta^{34}S_{CAS}$ = 36.3‰, 44.5‰) display higher values than those from the Goldberg spring mound (mean = 29.3‰, n = 6, σ = 1.8‰). CAS contents range from 1075 mg/kg to 4091 mg/kg, and there is strong negative correlation between CAS content and $\delta^{34}S_{CAS}$, where samples with lower CAS contents tend to have higher $\delta^{34}S_{CAS}$ ($R^2 = 0.81$). TIC for all carbonate samples is 11.6 wt% or greater (compared to 12 wt% for pure $CaCO_3$), attesting to their very low insoluble, siliciclastic contents. CRS contents were 30 mg/kg or lower and represent ≤ 5% of the measured TS in any given sample, suggesting that the risk of isotopic contamination from CRS oxidation during CAS extraction is low.

Impact Breccias

SUBO 18 (Crater Suevite)

The lowest sample depths (99.35 m - 86.4 m) of SUBO 18 are composed of impact melt breccia (n = 13) and have $\delta^{34}S_{CRS}$ values that generally decrease up core, ranging from 9.1‰ to -19.0‰ (**Fig. 1.2, Table 1.1**). The transition into crater suevite at 82.92 m coincides with a continued decrease until the minimum of -31.4‰ is reached at 68.59 m depth. This minimum is 4.5‰ lower than the next lightest value (-26.9‰ at 78.23 m) and does not appear to be representative of crater suevite (mean: -20.2‰, n = 20, σ = 5.8‰) or the entire set of impact breccia samples (mean: -15.8‰, n = 33, σ = 9.1‰). $\delta^{34}S_{CRS}$ then increases monotonically over the remainder of the core, reaching the crater suevite

maximum of -7.1‰ at 30.73 m, near the top of the analyzed interval. CRS wt% spans from 0.04% to 2.57% and differs in its relationship with $\delta^{34}S_{CRS}$ depending on rock type (**Fig. 1.5a**): crater suevites show a moderate negative correlation ($R^2 = 0.54$, $p < 0.001$), with high CRS wt% tending to correspond with low $\delta^{34}S_{CRS}$, while impact melt breccias show no discernable relationship ($R^2 = 0.03$). TOC wt% varies from < 0.1% (i.e., below detection limit [b.d.l.]) to 0.8%, but the majority of samples display low values; all but four of the 34 analyses have ≤ 0.3 wt% TOC. TOC wt% is consistently low in the samples with highest CRS wt% (**Fig. 1.5b**)—specifically, all samples with CRS contents > 1.3 wt% (n = 15) also have TOC ≤ 0.1 wt%.

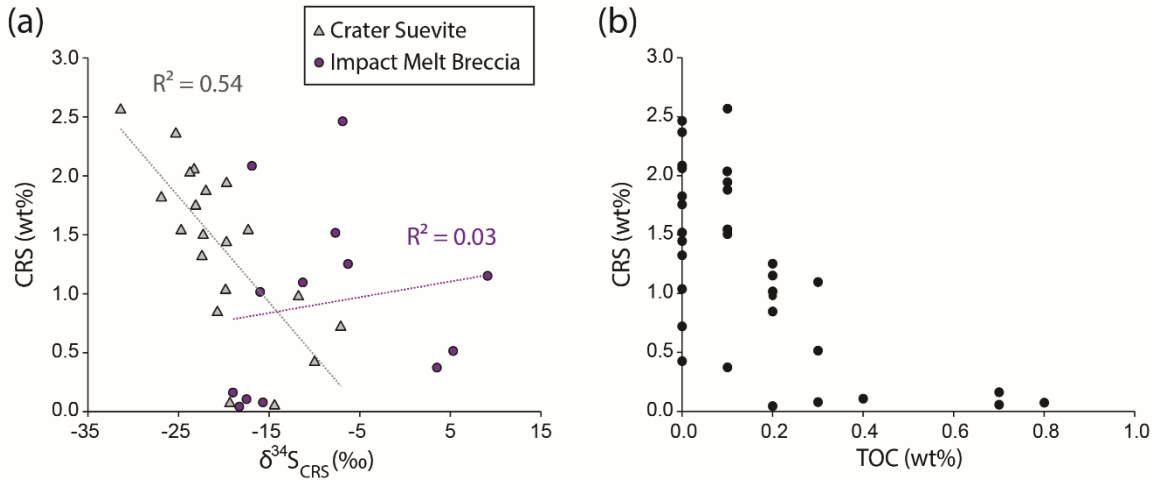

Figure 1.5 Scatterplots of SUBO 18 data. (a) There is a moderate relationship for CRS wt% versus $\delta^{34}S_{CRS}$ in crater suevite samples, but no relationship between these variables in impact melt breccia samples. (b) An apparent low TOC threshold is observed for the highest CRS contents, where all breccia samples with > 1.3 wt% CRS also have TOC ≤ 0.1 wt%.

BSE imaging (**Fig. 1.6**) reveals that Fe-sulfides are mainly disseminated throughout the groundmass (i.e., not in clasts) of both the crater suevite and the impact melt breccia. This observation is in agreement with previous petrographic and geochemical analyses of SUBO 18 (Reimold et al., 2012; Reimold et al., 2013), which revealed that these sulfides

are predominantly pyrite of post-impact origin, with minor occurrences of sphalerite [(Zn, Fe)S] in melt particles. Morphologically, the vast majority of the observed pyrite is non-framboidal, regardless of sample depth. Only one ~100 μm^2 area of one sample (68.59 m) was observed to contain framboid-like morphologies, which are ~1 μm in diameter and fracture-filling.

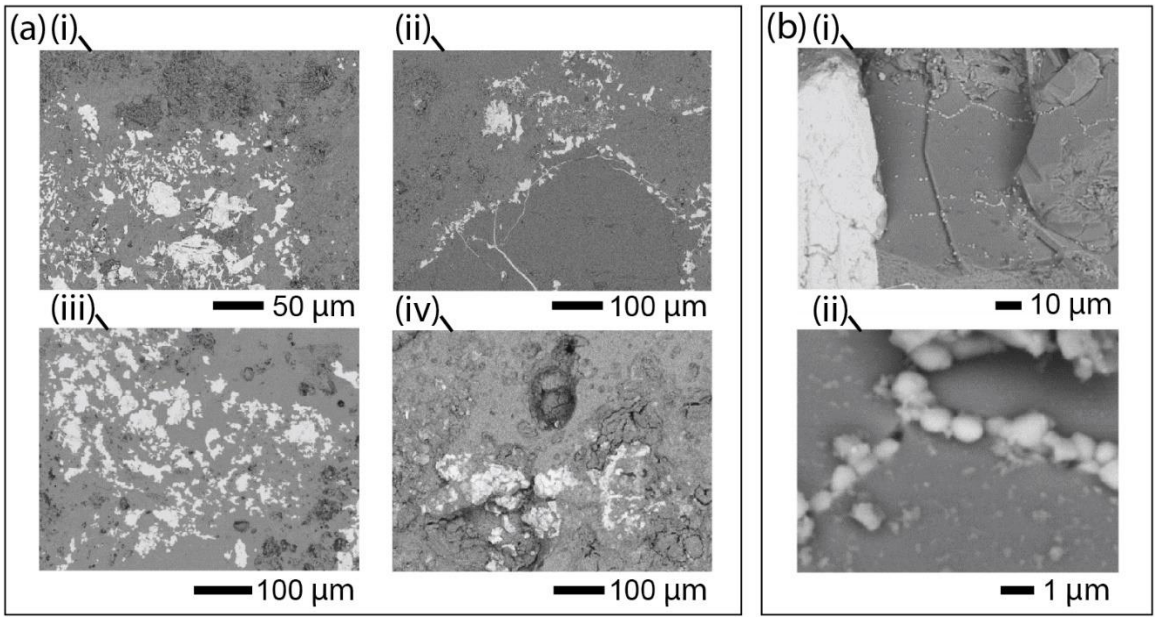

Figure 1.6 BSE Imaging data of polished SUBO 18 billets. (a) Images from four different depths show pyrite morphologies that are non-framboidal in nature. Depths: (i) 96.11 m, (ii) 90.93 m, (iii) 68.59 m, (iv) 30.75 m. (b) The only observation of framboid-like morphologies among the samples (shown at two different magnifications), where they (i) are filling fractures and (ii) are approximately 1 μm in diameter. They could alternatively be described as linked, near-equidimensional microcrystals. Both (i) and (ii) are at sample depth 68.59 m.

Field Samples (Outer Suevite)

All three field samples of outer suevite display CRS contents of 10 mg/kg or less. As a result, isotope measurements were not performed on these samples. These values are notably below 0.04 wt%, the observed CRS minimum for crater suevite. TOC was ≤ 0.1 wt%, and TS was < 0.1 wt% for all outer suevite samples.

Discussion

Overview of sulfur geochemistry at the hydrothermal Ries crater lake

The SUBO 18 interval under investigation is composed of impact breccias that had hydrothermal fluids migrate through them en route to the water column of the Miocene Ries crater lake. The formation of secondary pyrite in the subsurface impact breccias likely had a direct influence on the S chemistry of the fluids that reached and accumulated in the overlying waters, and the chemistry of these lake waters is preserved in the sedimentary deposits of FBN 73. The strongest hydrothermal influence on lake water chemistry likely occurred during the basin's early evolution from transient playas to a permanent lake (i.e., an interval of several 100 kyr that was likely coincident with the basal member extending into the early laminite member). The distinct geochemical differences between SUBO 18 and FBN 73 (**Fig. 1.2**) support this overarching interpretation. The lowest $\delta^{34}S_{CRS}$ values are sequestered in impact breccia, with the highest $\delta^{34}S_{CRS}$ values residing in the laminite member of the paleolake sediments. In a general sense, this relationship would be expected in order to satisfy isotopic mass balance. Past research suggests that meteoric waters (i.e., supplied by a combination of groundwater and precipitation) and the materials that they weathered were likely the only significant sources of dissolved SO_4^{2-} to the lake for much of its history (Arp et al., 2013a). During periods of hydrothermal activity, much of that SO_4^{2-} was apparently scavenged in the subsurface as sulfide, resulting in average CRS contents that are higher in the underlying impact breccias compared to sediments of the laminite member. Sulfate that was not scavenged in the subsurface would have become available to the lacustrine system via ascending hydrothermal fluids.

Within the crater lake ecosystem, as archived by FBN 73 and the carbonate mound samples, $\delta^{34}S$ was uniformly high. CAS data (**Fig. 1.4**) indicate that the SO_4^{2-} isotope composition of the water column ($\delta^{34}S_{CAS}$) during deposition of the laminite member ranged from 26.4‰ to 44.5‰, a spread similar to that of the $\delta^{34}S_{CRS}$ values of the FBN 73 laminite (17.5‰ to 45.1‰). Absolute concentrations of dissolved SO_4^{2-} in the lake water column cannot be directly inferred from measured CAS concentrations or $\delta^{34}S_{CAS}$ (Fichtner et al., 2017; Gill et al., 2008). However, given the depositional similarities of the carbonate mounds sampled in this study, we assert that comparisons of relative CAS concentrations, at least in a first-order sense, are valid. The strong anticorrelation between CAS concentrations and $\delta^{34}S_{CAS}$ values ($R^2 = 0.81$) suggests that high extents of S sequestration in the subsurface impact breccias led to more positive $\delta^{34}S$ values of the water-column sulfate. Furthermore, because the Wallerstein samples are older than those of the Goldberg mound, the $\delta^{34}S_{CAS}$ data of the carbonates fall on the same stratigraphically descending $\delta^{34}S$ trend defined by the laminite member. The slight differences between $\delta^{34}S_{CAS}$ and laminite $\delta^{34}S_{CRS}$ values therefore indicate small or insignificant fractionation events during the transformation of dissolved SO_4^{2-} (as captured by CAS) to mineral-phase sulfide (represented by CRS), or vice versa.

The data across the NR cores (**Fig. 1.3**) provide additional evidence that the general observed lake $\delta^{34}S$ trend represents a homogenous signal that existed throughout the basin and that $\delta^{34}S$ values are similar in magnitude across all phases measured (i.e., CRS, CAS, bulk materials, and kerogen). The NR core data also extend the argument that, at least during deposition of the lower laminite member, sulfate with high $\delta^{34}S$ was distributed

throughout the water column and in the sediments, with that S pool being preserved in the sediments with minimal net fractionation. This assertion is consistent with experimental studies that have demonstrated only small (< 4‰) $\delta^{34}S$ fractionation during the formation of both CAS from dissolved sulfate and pyrite from dissolved sulfide (Barkan et al., 2020; Butler et al., 2004), although some ^{34}S enrichment has been observed in sedimentary organic matter when compared to co-existing Fe-sulfides (e.g., Kotuzov et al., 2020).

In a model approach, Arp et al. (2013a) used the SO_4^{2-} concentrations found in local modern groundwaters (~0.85 mM; Winkler, 1972) and a dynamic impact breccia weathering scenario to show that water column SO_4^{2-} values were likely higher than 200 μM shortly after lake formation and remained that way for the remainder of the lake's lifetime (Arp et al., 2013a; Füchtbauer et al., 1977). Therefore, a concentration-dependent metabolic isotope effect, which can lead to small fractionations from MSR in a low SO_4^{2-} [below 200 μM] environment, appears unlikely (Crowe et al., 2014; Habicht et al., 2002; Harrison and Thode, 1958). However, near-quantitative MSR (i.e., an extent that is indistinguishable in the rock record from a quantitative reaction)—leading to reservoir-effect-induced sulfide isotopic compositions that closely resemble those of the parent dissolved SO_4^{2-}—is plausible under the high organic productivity regime of the laminite member. Microbial sulfate reduction likely occurred in the lake sediments during early diagenesis and possibly in the water column during certain intervals (i.e., euxinia), specifically in a saline hypolimnion with a sulfide surplus relative to Fe^{2+}, as indicated by the presence of thiophene biomarkers in the early laminite sediments (Arp et al., 2013a; Barakat et al., 1994; Barakat and Rullkötter, 1997; Rullkötter et al., 1990).

The coincident, gradual decline in $\delta^{34}S_{CRS}$ throughout the remainder of FBN 73 could then be interpreted as reflecting a highly restricted, evaporitic lake with progressively decreasing contributions of hydrothermally derived SO_4^{2-} and progressively increasing contributions of SO_4^{2-} from karstic groundwater and surface weathering of Bunte Breccia (Arp et al., 2013a). In any case, it is apparent that there was little-to-no observable S-isotope fractionation within the earliest subaerial lake itself. Thus, we interpret from the above data that the primary locus of fractionation (and therefore the source of both the maximum and minimum observed $\delta^{34}S$ values) was the subsurface hydrothermal system. The exact nature of the S isotope fractionation mechanism in the hydrothermal system, and its relevance as a biosignature, is more complex.

Mechanisms for the observed sulfur isotope variation

There are multiple lines of reasoning that can be used to assess the observed $\delta^{34}S$ variation at Ries Crater. MSR is often evoked as a means of explaining large differences in $\delta^{34}S$ values between source sulfate and product sulfide [$\Delta^{34}S_{sulfate\text{-}sulfide}$], with offsets of up to 75‰ (Brunner et al., 2005; Canfield et al., 2010; Lyons and Gill, 2010; Sim et al., 2011; Wortmann et al., 2001). However, meteorite impacts can induce target rock temperatures well in excess of 130°C, exceeding the limits of life and possibly generating significant thermochemical sulfate reduction while using the reducing power of organic matter (Abramov and Kring, 2005; Ivanov, 2004; Machel, 2001; Osinski et al., 2013). Thermochemical sulfate reduction has been shown to yield $\Delta^{34}S_{sulfate\text{-}sulfide}$ values of up to 21‰; this can confound interpretations that assign S-isotope fractionations to MSR,

specifically in cases where $\delta^{34}S$ variations are smaller than 21‰ in rocks exposed to temperatures above 100°C (Machel et al., 1995; Machel, 2001; Ohmoto and Goldhaber, 1997; Watanabe et al., 2009). Additionally, theoretical work indicates that hydrothermal activity can lead to large equilibrium fractionations between aqueous SO_4^{2-} and H_2S—e.g., $\Delta^{34}S_{SO_4^{2-}\text{-}H_2S}$ = 43.4‰ at 100°C (Eldridge et al., 2016; Marini et al., 2011; Ohmoto and Goldhaber, 1997; Sakai, 1968). Equilibrium S fractionation is typically considered for magmatic hydrothermal systems, but impact events also provide a plausible setting for this effect, depending on crater size, target rock composition, and fluid chemistry (Abramov and Kring, 2007; Franz et al., 2017; Ivanov, 2004; Kirsimäe and Osinski, 2012; Marini et al., 2011; Osinski et al., 2013). Each of these scenarios (i.e., MSR, TSR, and equilibrium fractionation) warrants individual evaluation, as well as consideration for the potential simultaneous or sequential occurrence of two or more fractionation mechanisms.

Microbial sulfate reduction

If the $\delta^{34}S$ data are viewed in the absence of the full system context, MSR is the most straightforward way to reconcile the $\delta^{34}S_{CRS}$ difference between the highest paleolake sedimentary samples and average impact breccia values (Δ = 61‰; **Fig. 1.2, Table 1.1**). Hydrothermal activity does not preclude MSR: optimal growth rates for hyperthermophilic MSR Bacteria can be at temperatures as high as 83°C, with an observed upper limit of 90°C (*Thermodesulfobacterium geofontis*; Hamilton-Brehm et al., 2013), while MSR Archaea also show optimal growth at temperatures as high as 83°C (*Archaeoglobus fulgidus*; Stetter 1988; Stetter et al. 1987) but can apparently function at temperatures

~100°C (Elsgaard et al., 1994; Jørgensen et al., 1992; Weber and Jørgensen, 2002). Canfield et al. (2000) measured MSR $\delta^{34}S$ fractionation from Guaymas Basin sediments sampled at 85°C and found $\Delta^{34}S_{sulfate\text{-}sulfide}$ of 13‰ to 28‰, comparable to results from pure thermophilic cultures (Böttcher et al., 1999). This fractionation is notably smaller than that observed in some isolates from mesophilic environments (i.e., > 60‰ in those measured by Canfield et al., 2010, and Sim et al., 2011). Taken together, these studies point to TSR or hydrothermal equilibrium as being the dominant S-fractionation mechanisms in geologic settings with temperatures > 100°C (Machel, 2001) and imply that, from a $\delta^{34}S$ perspective, it becomes increasingly difficult to distinguish between MSR and TSR as this temperature range is approached.

Appraisals of hyperthermophilic MSR viability aside, the lack of observed framboidal pyrite (associated with organics or otherwise) in favor of fracture- and/or void-filling forms makes possible biological origins ambiguous. In the single observed area where framboid-like pyrite is found (**Fig. 1.6b**), it is present in fracture fills. Indeed, these forms observed in SUBO 18 may not be true framboids in the sense that they do not show organized or disorganized clustering. They can instead be described as linked, near-equidimensional microcrystals. Even if we assume that all observed framboid-like pyrite was of bacterial origin, despite the variety of abiotic framboid formation mechanisms (Ohfuji and Rickard, 2005), these pyrites would be insignificant in terms of their overall contribution to $\delta^{34}S$ mass balance because they compose only a small portion of the total pyrite. The potential for morphological overprinting of pyrite framboids due to hydrothermal activity (Nozaki et al., 2020) furthers ambiguity and highlights a broader issue for sulfide biogenicity, as

hydrothermalism is generally considered a relevant feature for origin of life hypotheses on Earth as well as the search for life elsewhere (Deamer et al., 2019; Hendrix et al., 2019; Schwenzer and Kring, 2009). Hydrothermal activity is known to have been a feature of many impact craters on Earth and Mars (Osinski et al., 2013).

Contextual geochemical trends also contribute to MSR uncertainty. TOC wt% in the SUBO 18 samples is uniformly low, and a TOC wt% vs CRS wt% crossplot (**Fig. 1.5b**) shows low TOC wt% corresponding to high CRS wt%. This trend is the reverse of that typical of MSR, where higher TOC contents facilitate greater pyrite precipitation (e.g., Westrich and Berner, 1984). This reasoning also applies when scrutinizing the trend seen in suevite samples specifically (**Fig. 1.5a**), where higher CRS wt% corresponds to lower $\delta^{34}S_{CRS}$; greater rates of MSR and thus pyrite formation should impart smaller fractionations (Canfield, 2001; Kaplan and Rittenberg, 1964)—but the opposite is observed. Rather than invoking biology, these data may be better interpreted within the framework of post-impact TSR at temperatures exceeding 100°C.

Thermochemical sulfate reduction

Thermochemical sulfate reduction, like MSR, can consume organic carbon, facilitating pyrite formation and establishment of the lake's well-documented high alkalinity (Arp et al., 2013a; Füchtbauer et al., 1977; Stüeken, Tino et al., 2020). Importantly, TSR has been shown to be capable of fully consuming reactive carbon compounds in experimental settings (Meshoulam et al., 2016), allowing for the observed

high CRS wt% with low TOC wt% relationship in SUBO 18 (**Fig. 1.5b**). The net mass balance schematic thought to drive TSR is as follows (Machel, 1987; Machel, 2001):

$$SO_4^{2-} + \text{hydrocarbons} \rightarrow H_2S(HS^-) + HCO_3^-(CO_2) + H_2O$$

$$+ \text{altered hydrocarbons} + \text{solid bitumen}, \qquad (1.1)$$

where speciation within the CO_2-H_2O and H_2S-H_2O systems is pH- and temperature-dependent (e.g., Ohmoto and Goldhaber, 1997). There are multiple pathways that can play a role within this overall scheme, including an autocatalytic process involving H_2S consumption and generation (Orr, 1974; Zhang et al., 2008) and the potential necessity for Mg or Ca (Ma et al., 2008) in facilitating initial H_2S generation at the pH range (~6.5-8.5) of most TSR environments (Collins, 1975; Machel et al., 2001). This pH range is compatible with values suggested for the Ries hydrothermal fluids (Muttik et al., 2011; Osinski, 2005). Although fractionations associated with TSR do not appear to exceed the ~21‰ offset suggested in the $\delta^{34}S$ data compiled by Ohmoto and Goldhaber (1997) or generated experimentally by Watanabe et al. (2009), this value is not substantially smaller than what has so far been observed in (hyper)thermophilic MSR cultures (e.g., Böttcher et al., 1999; Canfield et al., 2000; Davidson et al., 2009; Habicht et al., 2005; Mitchell et al., 2009).

Rayleigh fractionation in a closed-system with respect to reactant SO_4^{2-} (and open for product H_2S to be removed as pyrite or volatilized out of the system; e.g., Hartmann and Nielsen, 2012) illustrates how distillation effects may have enhanced isotopic discrepancies within the crater lake system (**Fig. 1.7**; **Fig. 1.8**), where:

$$\delta_{\text{reactant(t)}} = (\delta_{\text{reactant(t=0)}} + 1000) \cdot f^{(\alpha_{\text{product-reactant}} - 1)} - 1000 \qquad (1.2)$$

$$\alpha = (1000 + \delta^{34}S_{product})/(1000 + \delta^{34}S_{reactant}) \quad (1.3)$$

and the δ value of total product molecules is approximated by:

$$\delta_{\Sigma product} = (\delta_{reactant(t=0)} - f \cdot \delta_{reactant(t)})/(1- f) \quad (1.4)$$

Within this framework, the observed maximum $\delta^{34}S_{CRS}$ in the lake sediments (≥ 45.1‰) and the mean $\delta^{34}S_{CRS}$ of SUBO 18 breccia (-15.8‰; represented here by the cumulative sulfide $\delta^{34}S$—or $\delta^{34}S_{\Sigma H_2S}$—value) can be satisfied via distillation. For example, when applying an initial $\delta^{34}S_{SO_4^{2-}}$ of 0‰, 74.1% of the original SO_4^{2-} pool must be removed with an enrichment factor [ε, where $\varepsilon = \delta^{34}S_{product} - \delta^{34}S_{reactant} \approx 1000\ln\alpha_{product\text{-}reactant}$] of ε = -32.8‰ (α ≈ 0.9672) in order to satisfy empirical observations (**Fig. 1.7a**). This enrichment factor is in excess of that for TSR (ε = -21‰) and higher than observations for cultured hyperthermophilic MSR (ε = -28‰). Alternatively, assuming a maximum TSR fractionation of ε = -21‰ (α ≈ 0.9790) in the same scenario generates $\delta^{34}S_{SO_4^{2-}}$ = 45.1‰ and $\delta^{34}S_{\Sigma H_2S}$ = -6.2‰ after reducing 87.8% of the original SO_4^{2-} pool (**Fig. 1.7b**). We use the maximum empirical ε value as a test case because the search for life elsewhere warrants a conservative approach to minimize the risk of a false positive. Similar ε values have been observed experimentally at 150°C (ε = -20.8‰; Watanabe et al., 2009), which is within the temperature range of the main alteration stage of Ries' impact breccias (100-200°C; Osinski, 2005). Shifting the initial $\delta^{34}S_{SO_4^{2-}}$ value in the negative direction allows for TSR results that track the entire dataset more closely. Thus, an initial $\delta^{34}S_{SO_4^{2-}}$ of -11.4‰ results in a $\delta^{34}S_{\Sigma H_2S}$ value of -15.7‰ with a $\delta^{34}S_{SO_4^{2-}}$ of 45.1‰ at 92.9% SO_4^{2-} removal. This scenario

would require the mixing of isotopically light SO_4^{2-} into the hydrothermal SO_4^{2-} reservoir. A plausible source of isotopically light sulfate is the oxidative weathering of pyrite within country rocks and/or impactites, including the Toarcian Posidonia shale, which is known to have contributed organic matter to Ries impact breccias (Hofmann et al., 2001). Previously measured $\delta^{34}S_{pyrite}$ from the Posidonia shale range from -7.7 to -44.5‰ (Berner et al., 2013). Various other target rock and regional S-bearing phases, including Jurassic carbonates (Reinhold, unpublished data) and Triassic arkoses (Nielsen, 1985; von Gehlen and Nielsen, 1985), display similarly low $\delta^{34}S$ values. Impact redistribution and oxidation of such materials, particularly via groundwater flow, may have lowered the $\delta^{34}S_{SO_4^{2-}}$ being fed into the hydrothermal system to $\delta^{34}S_{SO_4^{2-}} \leq$ -11.4‰ (i.e., consistent with the Rayleigh model presented above). While the pyrite in Posidonia shale, for example, is biogenic, naturally occurring abiotic pyrite with $\delta^{34}S \leq$ -11.4‰ (e.g., Goldfarb et al., 1991;

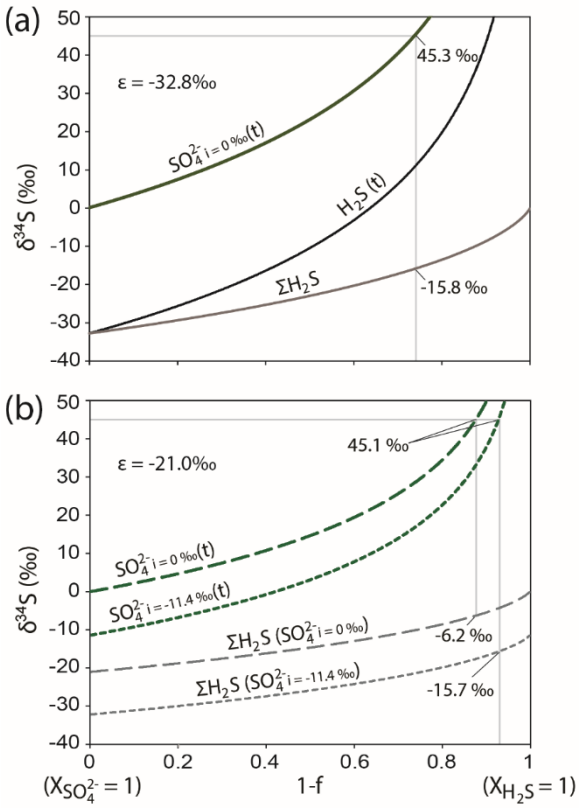

Figure 1.7 Rayleigh fractionation of stable S isotope ratios under multiple example starting conditions. (a) Using an initial $\delta^{34}S_{SO_4^{2-}}$ of 0‰ with an MSR-like enrichment factor of ε = -32.8‰ satisfies the maximum $\delta^{34}S_{CRS}$ observed in the lake sediments (≥ 45.1‰) with a $\delta^{34}S_{\Sigma H_2S}$ equal to the average SUBO 18 breccia $\delta^{34}S_{CRS}$ (-15.8‰). (b) Under a maximum TSR scenario (ε = -21.0‰) the initial SO_4^{2-} composition dictates whether the full observed isotopic range is expressed. An initial $\delta^{34}S_{SO_4^{2-}}$ of 0‰ results in $\delta^{34}S_{\Sigma H_2S}$ values ($\delta^{34}S_{\Sigma H_2S}$ = -6.2‰) that are higher than the average breccia $\delta^{34}S_{CRS}$ but within 1‰ of the suevite maximum ($\delta^{34}S_{CRS}$ = -7.1‰). Shifting the initial $\delta^{34}S_{SO_4^{2-}}$ value to -11.4‰, reflecting the input of light SO_4^{2-} (such as that sourced from oxidative pyrite weathering), satisfies the maximum $\delta^{34}S_{CRS}$ observed in the lake sediments with a co-occurring $\delta^{34}S_{\Sigma H_2S}$ that approximates the average SUBO 18 breccia $\delta^{34}S$.

Ohmoto and Goldhaber, 1997) could comprise the target rock of an impact crater on ancient Earth or Mars. Our model (**Fig. 1.8**) therefore explores a valid analog scenario.

The Rayleigh distillation scenarios above assume an ideal closed system and therefore can only provide a limited reconstruction of what was a highly dynamic environment (**Fig. 1.8**). Much of the earliest hydrothermal fluid was likely derived from groundwaters migrating into the hydrostatic void generated by the impact event (Osinski, 2005). Surface water would have percolated back downward into the breccia (Osinski, 2005) and tenuously balanced the upward movement of groundwater, particularly after reaching a hydrostatic equilibrium (there is no evidence of outlet formation at Ries crater). Thus, while Ries is not a theoretically ideal closed system, SO_4^{2-} anions would have had prolonged exposure to subsurface hydrothermal circulation. In any case, extensive Rayleigh distillation appears to have occurred: even the highest observed hyperthermophilic MSR fractionation (ε = -28) would require significant closed-system SO_4^{2-} removal (> 75%) to mimic the observed data.

It should be noted that an all-encompassing numerical solution that assumes the Ries crater to be a completely closed system with regards to $\delta^{34}S$ is not necessary to explain our observations. This is because temporal constraints on the intensity of hydrothermal activity during the paleolake interval that hosts $\delta^{34}S$ values of > 40‰ are limited. It is possible, for instance, that the $\delta^{34}S_{SO_4^{2-}}$ composition of the lake at that time reflects the latest possible stages of hydrothermal activity, when only the uppermost suevite was interacting with the lake surface water. The change in $\delta^{34}S_{\Sigma H_2S}$ through time may be reflected in the suevite $\delta^{34}S_{CRS}$ trend, which increases moving up core. This argument allows for a scenario

discussed above, where TSR generates $\delta^{34}S_{SO_4^{2-}}$ of 45.1‰ and $\delta^{34}S_{\Sigma H_2S}$ of -6.2‰ from initial $\delta^{34}S_{SO_4^{2-}}$ of 0‰ and could explain the relatively elevated $\delta^{34}S_{CRS}$ of the two uppermost suevite samples (which show values of -7.1‰ and -10.0‰). For this to occur, S would need to permanently escape the restricted basin, which can happen via H_2S volatilization. If the early laminite member waters were euxinic (Arp et al., 2013a; Barakat et al., 1994; Barakat and Rullkötter, 1997; Rullkötter et al., 1990), H_2S derived from the hydrothermal system could have been transported to the lake's water column. Water-column sulfide is susceptible to volatilization (Fry et al., 1986; Reese et al., 2008). An example is the modern Salton Sea in California, USA, where H_2S escapes to the atmosphere during seasonal mixing in a process that has been projected to remove ~24% of the basin's dissolved H_2S annually (Reese et al., 2008). While this effect imparts only minor fractionation ($\varepsilon_{gas\text{-}aqueous}$ = -1.6‰ to 3.0‰; see Baune and Böttcher, 2010; Fry et al., 1986; Sim et al., 2019), it nonetheless allows for the isotopic evolution of a restricted basin's sulfur reservoir on geologic timescales. This is because a proportion of the S derived from hydrothermal activity and isotopic distillation could have escaped via volatilization relatively early in the lake's history. If this was followed by increased relative input and mixing of non-hydrothermal, meteoric S (with its lower $\delta^{34}S$ composition), then the elevated early lacustrine $\delta^{34}S$ signal would be effectively diluted over time. The implication is that during formation of the lightest pyrite, $\delta^{34}S_{SO_4^{2-}}$ of < 45.1‰ may have been generated but is only briefly recorded in the rock record (i.e., during the transition from the basal member into the laminite member, where paleolake $\delta^{34}S_{CRS}$ values shift from -5.2‰ to 41.9‰ over the core depths of 260.5m–248.5m). As the basin evolved, the restricted recycling of high

$\delta^{34}S_{SO_4^{2-}}$ could have resulted in the simultaneous occurrence of the highest suevite $\delta^{34}S_{CRS}$ and the highest paleolake $\delta^{34}S$ values (Δ = 52.8‰, where $\delta^{34}S_{SO_4^{2-}}$ = 45.1‰ and $\delta^{34}S_{\Sigma H_2S}$ = -7.7‰). This spread can occur from TSR removing ~89% of a limited pool of SO_4^{2-} with an initial $\delta^{34}S_{SO_4^{2-}}$ value of -1.7—a plausible value for groundwater SO_4^{2-}, even without the likely mixing of an isotopically lighter SO_4^{2-} source such as oxidized pyrite of the Posidonia shale and/or other pyrite-bearing Jurassic and Triassic formations of the target rocks (Arp et al., 2021b). In light of the above discussion, we assert that TSR was as likely as MSR to have been the primary $\delta^{34}S$ fractionation mechanism in Ries crater.

Hydrothermal equilibrium isotope fractionation

The near-absence of organics associated with the most sulfide-enriched impact breccia samples may imply a role for hydrothermal equilibrium fractionation. After the exhaustion of reactive organic matter via TSR, equilibrium fractionation between aqueous S-bearing phases has been shown to occur (Meshoulam et al., 2016). The timescales needed for such an equilibration are highly dependent on temperature, pH, and the total concentration of S species [ΣS] (Ohmoto and Goldhaber, 1997; Sakai, 1968). According to the equations presented in Ohmoto and Goldhaber (1997), a hydrothermal solution (T = 100°C, pH = 7, ΣS = 0.01 molal) would take ~407 kyr to reach 90% of isotope exchange equilibrium (i.e., indistinguishable from an equilibrium state). At that temperature, the equilibrium fractionation for between SO_4^{2-} and H_2S has a $1000ln\alpha$ value of about 43‰, with SO_4^{2-} being substantially enriched in ^{34}S (Eldridge et al., 2016; Sakai, 1968). The subsequent equilibration of H_2S and HS^-, which is an expected occurrence at circumneutral-to-basic

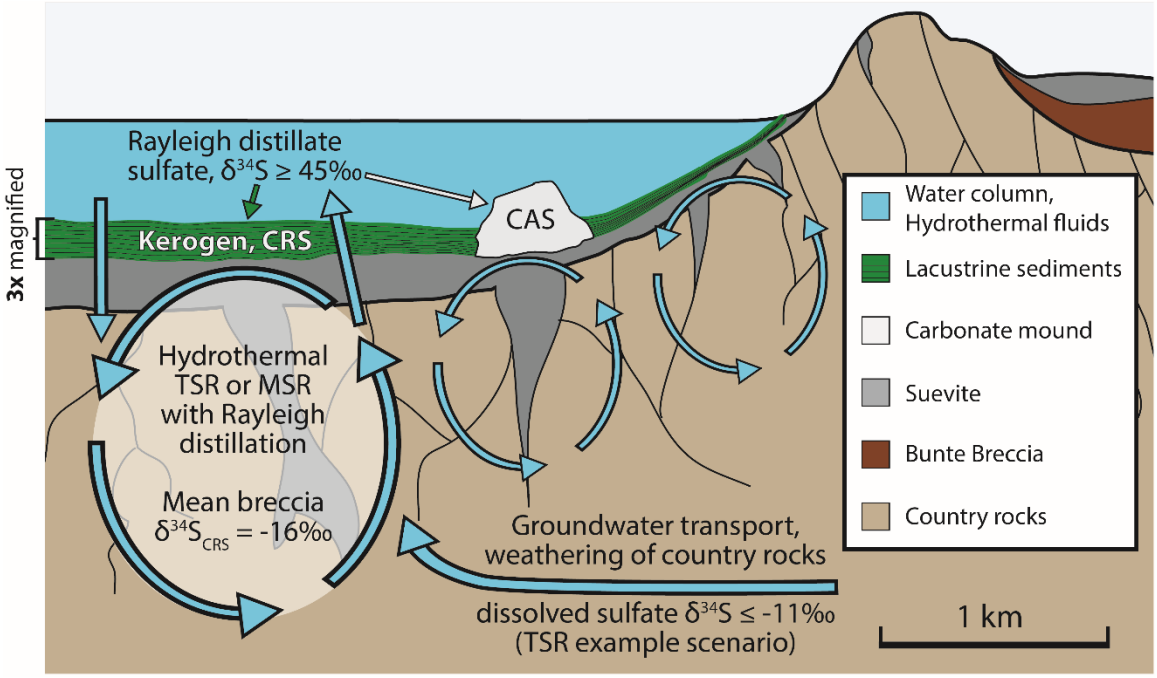

Figure 1.8 A proposed schematic of sulfur isotope fractionation at Ries crater during the earliest permanent lacustrine phase (late basal member into early laminite member). The primary locus of fractionation is within the subsurface hydrothermal system (fluid circulation indicated by blue arrows). The S system is initially fed by SO_4^{2-} primarily derived from the oxidative weathering of sulfide in country rocks that include impactites. Subaerial lake waters also percolate downward into the circulating fluids. In a TSR scenario (as visualized in **Figure 1.7b**) that reconciles our observed geochemical data, the $\delta^{34}S$ of this initial SO_4^{2-} must be -11‰ or lower. After a Rayleigh distillation process in which at least 93% of SO_4^{2-} is converted to H_2S (assuming a closed system), isotopically enriched SO_4^{2-} of $\delta^{34}S \geq 45‰$ reaches the water column of the lake. Sulfide produced in this hydrothermal process either precipitates as pyrite within suevite or is volatilized out of the system. Water column SO_4^{2-} is then incorporated into CAS (white arrow), as well as reduced and incorporated into lacustrine CRS and kerogen (green arrow), with little to no additional fractionation (indicated by the data in **Figures 1.2, 1.3, and 1.4**). Approximate basin structure, lithology, and horizontal scale were adapted from Stöffler et al. (2013). Thin black lines indicating lacustrine sedimentary layering are aesthetic and do not represent geologic data. Paleolacustrine sediment thickness from this lake stage (i.e., when $\delta^{34}S_{CRS} = 45.1‰$) is magnified three-fold (see left margin) with respect to the underlying suevite layer; thickness data are from the FBN 73 core only. For a detailed analysis of changes in the vertical extent of Ries crater sediments through time, see Arp et al. (2021).

pH, results in a $1000ln\alpha$ value of 2.5, where H_2S has a higher $\delta^{34}S$ than HS^- (Eldridge et al., 2016; Sakai, 1968). While the hydrothermal fluid composition described above is broadly consistent with the results from previous studies of the Ries crater system (e.g., Arp et al., 2013b; Muttik et al., 2010; Osinksi, 2005; Sapers et al., 2017), generating such a large fractionation would require fluid temperatures at ~100°C for the entirety of the protracted equilibration time. Further, changes to single parameters of the fluid

composition profoundly decrease the likelihood of this fractionation. Shifting the pH to ~9, which is compatible with the pH range suggested for the Ries system based on boron isotope measurements (Muttik et al., 2011), would increase the time necessary for an equilibration from ~407 kyr to an impossible ~869 Gyr. Decreases in ΣS by a factor of 10 also increase the time to equilibrium by a factor of 10 (Ohmoto and Goldhaber et al., 1997). Due to these rigid theoretical constraints, if hydrothermal equilibrium were ever reached at Ries crater, it would have been brief and occurred at temperatures where the equilibrium fractionation is much smaller (e.g., at 300°C, $1000ln\alpha = 19.8$; Eldridge et al., 2016). Such effects would be transient and likely overprinted beyond interpretation by larger, non-equilibrium fractionations caused by TSR or MSR. However, this remains a viable abiotic mechanism in acidic and/or high ΣS fluid environments where reductant scarcity prohibits non-equilibrium fractionation mechanisms.

Conclusion and Astrobiological Implications

In the present study, we tested the viability of stable sulfur isotopes as a biosignature in impact crater lakes through a detailed investigation of the Miocene Ries crater, which serves as an analog to early habitable locations on Mars and Earth. At Ries, elevated temperatures sustained by impact-induced hydrothermal activity allowed for the possibility of S isotope fractionation mechanisms that are rare in mesophilic environments (where $\delta^{34}S$ variation > 21‰ is often representative of microbial S cycling). After examining the observed $\delta^{34}S$ spread of ~77‰ at the Ries crater, we contend that TSR was at least as likely

as MSR to have been the primary $\delta^{34}S$ fractionation mechanism (**Fig. 1.8**). This conclusion is further supported by multiple lines of evidence, including impact breccia with TOC wt% versus CRS wt% and $\delta^{34}S_{CRS}$ versus CRS wt% relationships that are atypical of biological controls, as well as ambiguous pyrite textures. The hydrothermal system apparently dominated S isotope fractionation, as there is evidence (in the form of near-equivalent $\delta^{34}S$ in CRS, CAS, bulk-S, and kerogen-S samples) that lacustrine S cycling imparted little-to-no $\delta^{34}S$ fractionation during deposition of the most ^{34}S-enriched lacustrine pyrite (45‰). We have shown that a potential source of isotopically light SO_4^{2-} (e.g., oxidized pyrite of the Posidonia shale, or from other Jurassic and/or Triassic formations) from the catchment area of the lake would have allowed, via Rayleigh distillation of residual SO_4^{2-}, for TSR fractionation events of 21‰ to result in $\Delta^{34}S_{SO_4^{2-}\text{-}H_2S}$ distributions that match the observed Ries $\delta^{34}S$ spread. Additionally, spatiotemporal uncertainties inherent to impact-induced hydrothermal activity imply that $\delta^{34}S$ turnover via mechanisms such as H_2S volatilization is possible at the Ries crater given extensive timescales, regardless of its closed-basin nature.

Our overarching assessment that wide-ranging $\delta^{34}S$ in impact crater lakes need not be biological is in general agreement with *in-situ* Curiosity rover findings (Franz et al., 2017), although the specified mechanisms differ. Hydrothermal equilibration of aqueous S species at temperatures ~100°C is unlikely at Ries given constraints involving elevated fluid pH and hydrothermal activity duration (several 100 ky) (Arp et al., 2013b; Ohmoto and Goldhaber, 1997). However, this remains a viable fractionation mechanism at Gale crater, where fluid pH appears to have been acidic-to-circumneutral, and the crater's larger

diameter (154 km) implies longer-lasting hydrothermal activity (Abramov and Kring, 2005; Berger et al., 2017; McLennan et al., 2013; Rampe et al., 2020). Our study, however, suggests that impact-induced TSR of abiotically derived organic matter should also be a considered S-fractionation mechanism at Gale, Jezero, and other ancient craters on Mars and Earth. Exogenous delivery of abiotic organics may have been relatively widespread early in our solar system's lifetime (Sandford et al., 2020), and it is plausible that there was/is a subsurface abiotic organic reservoir on Mars (Eigenbrode et al., 2018; Yang et al., 2020) available to be incorporated into breccia during impact events and subsequently used as a reductant for TSR. TSR could have also proceeded on ancient Mars via alternative reducing species such as dissolved H_2 (Cai et al., 2022; Wordsworth et al., 2021) and has previously been proposed to explain the multiple sulfur isotope distribution of pyrite in Martian meteorite NWA 7533 (Lorand et al., 2020). Therefore, even with our multitude of well-preserved samples, wet chemical techniques, and Earth-bound instrumentation, our wide-ranging (> 21‰) $\delta^{34}S$ data from an impact crater paleolake suggest that biological processes need not be involved. In other words, wide $\delta^{34}S$ ranges can be abiological, and overarching geologic context is essential to any interpretation of such data. Thus, the potential ambiguities of sulfur isotope composition as a biosignature should be recognized in future studies of crater systems on Mars and Earth. Ultimately, any convincing arguments for past life on Mars or elsewhere within or beyond our solar system would likely have to be built on multiple parameters viewed within a comprehensive context.

References

Abramov, O., & Kring, D. A. (2005). Impact-Induced Hydrothermal Activity on Early Mars. *Journal of Geophysical Research*, 110(E12), E12S09.

Abramov, O., & Kring, D. A. (2007). Numerical Modeling of Impact-Induced Hydrothermal Activity at the Chicxulub Crater. *Meteoritics and Planetary Science*, 42(1), 93–112.

Arp, G. (1995). Lacustrine Bioherms, Spring Mounds, and Marginal Carbonates of the Ries-impact-crater (Miocene, southern Germany). *Facies*, 33(1), 35-89.

Arp, G. (2006). Sediments of the Ries Crater Lake (Miocene, Southern Germany). *Schriftenreihe der deutschen Gesellschaft für Geowissenschaften*, 45, 213–236.

Arp, G., Bielert, F., Hoffmann, V. E., & Löffler (2005). Palaeoenvironmental Significance of Lacustrine Stromatolites of the Arnstadt Formation ("Steinmergelkeuper", Upper Triassic, N-Germany). *Facies*, 51(1–4), 419–441.

Arp, G., Blumenberg, M., Hansen, B. T., Jung, D., Kolepka, C., Lenz, O., Nolte, N., Poschlod, K., Reimer, A., & Thiel, V. (2013a). Chemical and Ecological Evolution of the Miocene Ries Impact Crater Lake, Germany: A Reinterpretation Based on the Enkingen (SUBO 18) Drill Core. *Geological Society of America Bulletin*, 125(7–8), 1125–1145.

Arp, G., Dunkl, I., Jung, D., Karius, V., Lukács, R., Zeng, L., Reimer, A. & Head III, J.W. (2021a). A Volcanic Ash Layer in the Nördlinger Ries Impact Structure (Miocene, Germany): Indication of Crater Fill Geometry and Origins of Long-Term Crater Floor Sagging. *Journal of Geophysical Research: Planets*, 126(4).

Arp, G., Gropengießer, S., Schulbert, C., Jung, D., & Reimer, A., (2021b). Biostratigraphy and sequence stratigraphy of the Toarcian Ludwigskanal section (Franconian Alb, Southern Germany). *Zitteliana*, 95, 57-94.

Arp, G., Hansen, B. T., Pack, A., Reimer, A., Schmidt, B.C., Simon, K., & Jung, D. (2017). The Soda Lake—Mesosaline Halite Lake Transition in the Ries Impact Crater Basin (Drilling Löpsingen 2012, Miocene, Southern Germany). *Facies*, 63(1), 1.

Arp, G., Kolepka, C., Simon, K., Karius, V., Nolte, N., & Hansen, B.T. (2013b). New Evidence for Persistent Impact-Generated Hydrothermal Activity in the Miocene Ries Impact Structure, Germany. *Meteoritics and Planetary Science*, 48(12), 2491–2516.

Artemieva, N.A., Wünnemann, K., Krien, F., Reimold, W.U., & Stöffler, D. (2013). Ries Crater and Suevite Revisited-Observations and Modeling Part II: Modeling. *Meteoritics and Planetary Science*, 48(4), 590–627.

Barakat, A.O., Baumgart, S., Brocks, P., Scholz-Böttcher, B.M., & Rullkötter, J. (2012). Alkylated Phenol Series in Lacustrine Black Shales from the Nördlinger Ries, Southern Germany. *Journal of Mass Spectrometry*, 47(8), 987–994.

Barakat, A. O., Peakman, T. M., & Rullkötter, J. (1994). Isolation and Structural Characterization of 10-Oxo-Octadecanoic Acid in Some Lacustrine Sediments from the Nördlinger Ries (Southern Germany). *Organic Geochemistry*, 21(8–9), 841–847.

Barakat, A. O., & Rullkötter, J. (1995). Extractable and Bound Fatty Acids in Core Sediments from the Nördlinger Ries, Southern Germany. *Fuel, 74*(3), 416–425.

Barakat, A. O., & Rullkötter, J. (1997). A Comparative Study of Molecular Paleosalinity Indicators: Chromans, Tocopherols and C20 Isoprenoid Thiophenes in Miocene Lake Sediments (Nördlinger Ries, Southern Germany). *Aquatic Geochemistry, 3*(2), 169–190.

Barakat, A. O., Scholz-Böttcher, B. M., & Rullkötter, J. (2013). Lipids in a Sulfur-Rich Lacustrine Sediment from the Nördlinger Ries (Southern Germany) with a Focus on Free and Bound Sterols. *Geochemical Journal, 47*(4), 397–407.

Barkan, Y., Paris, G., Webb, S.M., Adkins, J.F., & Halevy, I. (2020). Sulfur isotope fractionation between aqueous and carbonate-associated sulfate in abiotic calcite and aragonite. *Geochimica et Cosmochimica Acta, 280*, 317–339.

Barlow, N. G. (2005). A Review of Martian Impact Crater Ejecta Structures and Their Implications for Target Properties. In: *Large Meteorite Impacts III*, Geological Society of America, pp. 433–442.

Baune, C., & Böttcher, M. E. (2010). Experimental Investigation of Sulphur Isotope Partitioning during Outgassing of Hydrogen Sulphide from Diluted Aqueous Solutions and Seawater. *Isotopes in Environmental and Health Studies, 46*(4), 444–453.

Berger, J.A., Schmidt, M.E., Gellert, R., Boyd, N.I., Desouza, E.D., Flemming, R.L., Izawa, M.R., Ming, D.W., Perrett, G.M., Rampe, E.B., & Thompson, L.M. (2017). Zinc and Germanium in the Sedimentary Rocks of Gale Crater on Mars Indicate Hydrothermal Enrichment Followed by Diagenetic Fractionation. *Journal of Geophysical Research: Planets, 122*(8), 1747–1772.

Berner, Z.A., Puchelt, H., Noeltner, T., & Kramar, U.T.Z. (2013). Pyrite Geochemistry in the Toarcian Posidonia Shale of South-West Germany: Evidence for Contrasting Trace-Element Patterns of Diagenetic and Syngenetic Pyrites. *Sedimentology, 60*(2), 548–573.

Böttcher, M. E., Brumsack, H.-J., & de Lange, G. J. (1998). Sulfate Reduction and Related Stable Isotope (34S, 18O) Variations in Interstitial Waters from the Eastern Mediterranean. In: *Proceedings of the Ocean Drilling Program, 160 Scientific Results*, Ocean Drilling Program.

Böttcher, M. E., & Schnetger, B. (2004). Direct Measurement of the Content and Isotopic Composition of Sulfur in Black Shales by Means of Combustion-Isotope-Ratio-Monitoring Mass Spectrometry (C-IrmMS). In: (P. de Groot, Ed.), *Handbook of Stable Isotope Analytical Techniques, Part I*, pp. 597–603.

Böttcher, M. E., Sievert, S. M., & Kuever, J. (1999). Fractionation of Sulfur Isotopes during Dissimilatory Reduction of Sulfate by a Thermophilic Gram-Negative Bacterium at 60 °C. *Archives of Microbiology, 172*(2), 125–128.

Brand, W. A., & Coplen, T. B. (2012). Stable Isotope Deltas: Tiny, yet Robust Signatures in Nature. *Isotopes in Environmental and Health Studies, 48*(3), 393–409.

Brunner, B., Bernasconi, S.M., Kleikemper, J., & Schroth, M.H. (2005). A Model for Oxygen and Sulfur Isotope Fractionation in Sulfate during Bacterial Sulfate Reduction Processes. *Geochimica et Cosmochimica Acta, 69*(20), 4773–4785.

Butler, I.B., Böttcher, M.E., Rickard, D., & Oldroyd, A. (2004). Sulfur isotope partitioning during experimental formation of pyrite via the polysulfide and hydrogen sulphide pathways: Implications for the interpretation of sedimentary and hydrothermal pyrite isotope records. *Earth and Planetary Science Letters, 228*(3-4), 495-509.

Cai, C., Li, H., Li, K., & Wang, D. (2022). Thermochemical sulfate reduction in sedimentary basins and beyond: A review. *Chemical Geology, 121018*.

Canfield, D. E. (2001). Biogeochemistry of Sulfur Isotopes. *Reviews in Mineralogy and Geochemistry, 43*.

Canfield, D. E., Farquhar, J., & Zerkle, A. L. (2010). High Isotope Fractionations during Sulfate Reduction in a Low-Sulfate Euxinic Ocean Analog. *Geology, 38*(5).

Canfield, D. E., Habicht, K. S., & Thamdrup, B. (2000). The Archean Sulfur Cycle and the Early History of Atmospheric Oxygen. *Science, 288*(5466), 658–661.

Canfield, D. E., Raiswell, R., Westrich, J. T., Reaves, C. M., & Berner, R. A. (1986). The Use of Chromium Reduction in the Analysis of Reduced Inorganic Sulfur in Sediments and Shales. *Chemical Geology, 54*(1–2), 149–155.

Caudill, C., Osinski, G. R., Greenberger, R. N., Tornabene, L. L., Longstaffe, F. J., Flemming, R. L., & Ehlmann, B. L. (2021). Origin of the Degassing Pipes at the Ries

Impact Structure and Implications for Impact-induced Alteration on Mars and Other Planetary Bodies. *Meteoritics & Planetary Science, 56*(2), 404–422.

Clark, B. C., Baird, A. K., Weldon, R. J., Tsusaki, D. M., Schnabel, L., & Candelaria, M. P. (1982). Chemical Composition of Martian Fines. *Journal of Geophysical Research, 87*(B12), 10059.

Cockell, C. S., Osinski, G., Sapers, H., Pontefract, A., & Parnell, J. (2020). Microbial Life in Impact Craters. *Current Issues in Molecular Biology, 38*.

Collins, A. (1975). Geochemistry of Oilfield Waters. Elsevier.

Crowe, S.A., Paris, G., Katsev, S., Jones, C., Kim, S.T., Zerkle, A.L., Nomosatryo, S., Fowle, D.A., Adkins, J.F., Sessions, A.L., & Farquhar, J. (2014). Sulfate Was a Trace Constituent of Archean Seawater. *Science, 346*(6210), 735–739.

Davidson, M.M., Bisher, M.E., Pratt, L.M., Fong, J., Southam, G., Pfiffner, S.M., Reches, Z., & Onstott, T.C. (2009). Sulfur Isotope Enrichment during Maintenance Metabolism in the Thermophilic Sulfate-Reducing Bacterium *Desulfotomaculum Putei*. *Applied and Environmental Microbiology, 75*(17), 5621–5630.

Deamer, D., Damer, B., & Kompanichenko, V. (2019). Hydrothermal Chemistry and the Origin of Cellular Life. *Astrobiology, 19*(12), 1523-1537.

Ding, T., Valkiers, S., Kipphardt, H., De Bievre, P., Taylor, P. D. P., Gonfiantini, R., & Krouse, R. (2001). Calibrated Sulfur Isotope Abundance Ratios of Three IAEA Sulfur Isotope Reference Materials and V-CDT with a Reassessment of the Atomic Weight of Sulfur. *Geochimica et Cosmochimica Acta, 65*(15), 2433–2437.

Di Vincenzo, G. (2022). High precision multi-collector $^{40}Ar/^{39}Ar$ dating of moldavites (Central European tektites) reconciles geochronological and paleomagnetic data. *Chemical Geology, 608*, 121026.

Eigenbrode, J. L., Summons, R. E., Steele, A., et al. (2018). Organic Matter Preserved in 3-Billion-Year-Old Mudstones at Gale Crater, Mars. *Science, 360*(6393), 1096–1101.

Elsgaard, L., Isaksen, M. F., Jørgensen, B. B., Alayse, A. M., & Jannasch, H. W. (1994). Microbial Sulfate Reduction in Deep-Sea Sediments at the Guaymas Basin Hydrothermal Vent Area: Influence of Temperature and Substrates. *Geochimica et Cosmochimica Acta, 58*(16), 3335–3343.

Eldridge, D. L., Guo, W., & Farquhar, J. (2016). Theoretical Estimates of Equilibrium Sulfur Isotope Effects in Aqueous Sulfur Systems: Highlighting the Role of Isomers in the Sulfite and Sulfoxylate Systems. *Geochimica et Cosmochimica Acta, 195*, 171–200.

Farmer, J. D. (2000). Hydrothermal Systems: Doorways to Early Biosphere Evolution. *GSA Today, 10*(7).

Fichtner, V., Strauss, H., Immenhauser, A., Buhl, D., Neuser, R. D., & Niedermayr, A. (2017). Diagenesis of Carbonate Associated Sulfate. *Chemical Geology, 463*, 61–75.

Förstner, V. U. (1977). Geochemische Untersuchungen an den Sedimenten des Ries-Sees (Forschungsbohrung Nördlingen 1973). *Geologica Bavarica, 75*, 13–19.

Franz, H. B., King, P. L., & Gaillard, F. (2019). Sulfur on Mars from the Atmosphere to the Core. In *Volatiles in the Martian Crust*.

Franz, H.B., McAdam, A.C., Ming, D.W., Freissinet, C., Mahaffy, P.R., Eldridge, D.L., Fischer, W.W., Grotzinger, J.P., House, C.H., Hurowitz, J.A., & McLennan, S.M. (2017). Large Sulfur Isotope Fractionations in Martian Sediments at Gale Crater. *Nature Geoscience, 10*(9), 658–662.

Fry, B., Gest, H., & Hayes, J. M. (1986). Sulfur Isotope Effects Associated with Protonation of HS^- and Volatilization of H_2S. *Chemical Geology, 58*(3), 253–258.

Füchtbauer, H., Von Der Brelie, G., Dehm, R., Förstner, U., Gall, H., & Höfling, R. (1977). Tertiary lake sediments of the Ries, research borehole Nördlingen 1973 - a summary. *Geologica Bavarica, 75*, 13–19.

Gill, B. C., Lyons, T. W., & Frank, T. D. (2008). Behavior of Carbonate-Associated Sulfate during Meteoric Diagenesis and Implications for the Sulfur Isotope Paleoproxy. *Geochimica et Cosmochimica Acta, 72*(19), 4699–4711.

Goldfarb, R. J., Newberry, R. J., Pickthorn, W. J., & Gent, C. A. (1991). Oxygen, hydrogen, and sulfur isotope studies in the Juneau gold belt, southeastern Alaska; constraints on the origin of hydrothermal fluids. *Economic Geology, 86*(1), 66–80.

Goudge, T. A., Mustard, J. F., Head, J. W., Fassett, C. I., & Wiseman, S. M. (2015). Assessing the Mineralogy of the Watershed and Fan Deposits of the Jezero Crater Paleolake System, Mars. *Journal of Geophysical Research: Planets, 120*(4).

Graup, G. (1999). Carbonate-Silicate Liquid Immiscibility upon Impact Melting: Ries Crater, Germany. *Meteoritics and Planetary Science, 34*(3), 425–438.

Grotzinger, J.P., Gupta, S., Malin, M.C., Rubin, D.M., Schieber, J., Siebach, K., Sumner, D.Y., Stack, K.M., Vasavada, A.R., Arvidson, R.E., & Calef III, F. (2015). Deposition, Exhumation, and Paleoclimate of an Ancient Lake Deposit, Gale Crater, Mars. *Science, 350*(6257).

Habicht, K. S., Gade, M., Thamdrup, B., Berg, P., & Canfield, D. E. (2002). Calibration of Sulfate Levels in the Archean Ocean. *Science, 298*(5602), 2372–2374.

Habicht, K. S., Salling, L., Thamdrup, B., & Canfield, D. E. (2005). Effect of Low Sulfate Concentrations on Lactate Oxidation and Isotope Fractionation during Sulfate Reduction by Archaeoglobus Fulgidus Strain Z. *Applied and Environmental Microbiology, 71*(7), 3770–3777.

Hamilton-Brehm, S.D., Gibson, R.A., Green, S.J., Hopmans, E.C., Schouten, S., van der Meer, M.T., Shields, J.P., Damsté, J.S., & Elkins, J.G. (2013). Thermodesulfobacterium Geofontis Sp. Nov., a Hyperthermophilic, Sulfate-Reducing Bacterium Isolated from Obsidian Pool, Yellowstone National Park. *Extremophiles, 17*(2), 251–263.

Harrison, A. G., & Thode, H. G. (1958). Mechanism of the Bacterial Reduction of Sulphate from Isotope Fractionation Studies. *Transactions of the Faraday Society, 54*, 84.

Hartmann, M., & Nielsen, H. (2012). $\delta^{34}S$ Values in Recent Sea Sediments and Their Significance Using Several Sediment Profiles from the Western Baltic Sea. Isotopes in *Environmental and Health Studies, 48*(1), 7–32.

Hays, L.E., Graham, H.V., Des Marais, D.J., Hausrath, E.M., Horgan, B., McCollom, T.M., Parenteau, M.N., Potter-McIntyre, S.L., Williams, A.J., & Lynch, K.L. (2017). Biosignature Preservation and Detection in Mars Analog Environments. *Astrobiology, 17*(4).

Hendrix, A.R., Hurford, T.A., Barge, L.M., Bland, M.T., Bowman, J.S., Brinckerhoff, W., Buratti, B.J., Cable, M.L., Castillo-Rogez, J., Collins, G.C., & Diniega, S. (2019). The NASA Roadmap to Ocean Worlds. *Astrobiology, 19*(1), 1-27.

Hoefs, J. (2021). Stable Isotope Geochemistry (3rd ed.). Springer International Publishing.

Hörz, F., Ostertag, R., & Rainey, D. A. (1983). Bunte Breccia of the Ries: Continuous Deposits of Large Impact Craters. *Reviews of Geophysics, 21*(8), 1667.

Hofmann, P., Leythaeuser, D., & Schwark, L. (2001). Organic Matter from the Bunte Breccia of the Ries Crater, Southern Germany: Investigating Possible Thermal Effects of the Impact. *Planetary and Space Science, 49*(8), 845–851.

Ivanov, B. A. (2004). Heating of the Lithosphere during Meteorite Cratering. *Solar System Research, 38*(4), 266–279.

Jankowski, B. (1977). Die Postimpakt-Sedimente in der Forschungsbohrung Nördlingen 1973. *Geologica Bavarica, 75*, 21–36.

Jørgensen, B. B., Isaksen, M. F., & Jannasch, H. W. (1992). Bacterial Sulfate Reduction Above 100°C in Deep-Sea Hydrothermal Vent Sediments. *Science, 258*(5089), 1756–1757.

Kacar, B., Garcia, A. K., & Anbar, A. D. (2021). Evolutionary History of Bioessential Elements Can Guide the Search for Life in the Universe. *ChemBioChem, 22*, 114–119.

Kaplan, I. R., & Rittenberg, S. C. (1964). Microbiological Fractionation of Sulphur Isotopes. *Journal of General Microbiology, 34*(2), 195–212.

Kenkmann, T., & Schönian, F. (2006). Ries and Chicxulub: Impact craters on Earth provide insights for Martian ejecta blankets. *Meteoritics & Planetary Science, 41*(10), 1587–1603.

King, P. L., & McLennan, S. M. (2010). Sulfur on Mars. *Elements, 6*(2).

Kirsimäe, K., & Osinski, G. R. (2012). Impact-Induced Hydrothermal Activity. In Impact Cratering (Osinski GR and Pierazzo E, Eds.), pp. 76–89.

Kring, D. A. (2000). Impact Events and Their Effect on the Origin, Evolution, and Distribution of Life. *GSA Today, 10*(8).

Kring, D. A., Whitehouse, M. J., & Schmieder, M. (2021). Microbial Sulfur Isotope Fractionation in the Chicxulub Hydrothermal System. *Astrobiology, 21*(1), 103–114.

Kutuzov, I., Rosenberg, Y. O., Bishop, A., & Amrani, A. (2020). The Origin of Organic Sulphur Compounds and Their Impact on the Paleoenvironmental Record. In Hydrocarbons, Oils and Lipids: Diversity, Origin, Chemistry and Fate (Wilkes H, Ed.). Handbook of Hydrocarbon and Lipid Microbiology.

Liaghati, T., Cox, M. E., & Preda, M. (2005). Distribution of Fe in Waters and Bottom Sediments of a Small Estuarine Catchment, Pumicestone Region, Southeast Queensland, Australia. *Science of the Total Environment, 336*(1–3), 243–254.

Léveillé, R. (2010). A Half-Century of Terrestrial Analog Studies: From Craters on the Moon to Searching for Life on Mars. *Planetary and Space Science, 58*(4).

Lorand, J.P., Labidi, J., Rollion-Bard, C., Thomassot, E., Bellucci, J.J., Whitehouse, M., Nemchin, A., Humayun, M., Farquhar, J., Hewins, R.H., & Zanda, B. (2020). The Sulfur Budget and Sulfur Isotopic Composition of Martian Regolith Breccia NWA 7533. *Meteoritics & Planetary Science, 55(9)*, 2097–2116.

Lyons, T. W., & Gill, B. C. (2016). Ancient Sulfur Cycling and Oxygenation of the Early Biosphere. *Elements, 6*(2), 93–99.

Ma, Q., Ellis, G. S., Amrani, A., Zhang, T., & Tang, Y. (2008). Theoretical Study on the Reactivity of Sulfate Species with Hydrocarbons. *Geochimica et Cosmochimica Acta, 72*(18), 4565–4576.

Machel, H. G. (1987). Some Aspects of Diagenetic Sulphate-hydrocarbon Redox Reactions. *Geological Society Special Publications, 36*(1), 15–28.

Machel, H. G. (2001). Bacterial and Thermochemical Sulfate Reduction in Diagenetic Settings — Old and New Insights. *Sedimentary Geology, 140*(1–2), 143–175.

Machel, H. G., Krouse, H. R., & Sassen, R. (1995). Products and Distinguishing Criteria of Bacterial and Thermochemical Sulfate Reduction. *Applied Geochemistry, 10(4)*, 373–389.

Mangold, N., Gupta, S., Gasnault, O., Dromart, G., Tarnas, J.D., Sholes, S.F., Horgan, B., Quantin-Nataf, C., Brown, A.J., Le Mouélic, S., & Yingst, R.A. (2021). Perseverance Rover Reveals an Ancient Delta-Lake System and Flood Deposits at Jezero Crater, Mars. *Science, 374*(6568).

Marini, L., Moretti, R., & Accornero, M. (2011). Sulfur Isotopes in Magmatic-Hydrothermal Systems, Melts, and Magmas. *Reviews in Mineralogy and Geochemistry, 73*(1), 423–492.

McLennan, S.M., Anderson, R.B., Bell III, J.F., Bridges, J.C., Calef III, F., Campbell, J.L., Clark, B.C., Clegg, S., Conrad, P., Cousin, A., & Des Marais, D.J. (2014). Elemental Geochemistry of Sedimentary Rocks at Yellowknife Bay, Gale Crater, Mars. *Science, 343*(6169).

Meshoulam, A., Ellis, G.S., Ahmad, W.S., Deev, A., Sessions, A.L., Tang, Y., Adkins, J.F., Liu, J., Gilhooly III, W.P., Aizenshtat, Z., & Amrani, A. (2016). Study of Thermochemical Sulfate Reduction Mechanism Using Compound Specific Sulfur Isotope Analysis. *Geochimica et Cosmochimica Acta, 188*, 73–92.

Mitchell, K., Heyer, A., Canfield, D. E., Hoek, J., & Habicht, K. S. (2009). Temperature Effect on the Sulfur Isotope Fractionation during Sulfate Reduction by Two Strains of the Hyperthermophilic Archaeoglobus Fulgidus. *Environmental Microbiology, 11*(12), 2998–3006.

Montano, D., Gasparrini, M., Gerdes, A., Della Porta, G., & Albert, R. (2021). In-Situ U-Pb Dating of Ries Crater Lacustrine Carbonates (Miocene, South-West Germany): Implications for Continental Carbonate Chronostratigraphy. *Earth and Planetary Science Letters, 568*, 117011.

Muttik, N., Kirsimäe, K., Newsom, H. E., & Williams, L. B. (2011). Boron Isotope Composition of Secondary Smectite in Suevites at the Ries Crater, Germany: Boron Fractionation in Weathering and Hydrothermal Processes. *Earth and Planetary Science Letters, 310*(3–4), 244–251.

Muttik, N., Kirsimäe, K., & Vennemann, T. W. (2010). Stable Isotope Composition of Smectite in Suevites at the Ries Crater, Germany: Implications for Hydrous Alteration of Impactites. *Earth and Planetary Science Letters, 299*(1–2), 190–195.

Newsom, H. E., Graup, G., Iseri, D. A., Geissman, J. W., Keil, K., Sharpton, V. L., & Ward, P. D. (1990). The Formation of the Ries Crater, West Germany; Evidence of Atmospheric Interactions during a Larger Cratering Event. In Global Catastrophes in Earth History; An Interdisciplinary Conference on Impacts, Volcanism, and Mass Mortality (pp. 195–206).

Newsom, H.E., Graup, G., Sewards, T., & Keil, K. (1986). Fluidization and Hydrothermal Alteration of the Suevite Deposit at the Ries Crater, West Germany, and Implications for Mars. *Journal of Geophysical Research, 91*(B13), E239.

Nielsen, H. (1985). Sulfur-Isotope Ratios in Strata-Bound Mineralizations in Central Europe. *Geological Jahrbuch D, 70*, 225-262.

Nielsen, H., Pilot, J., Grinenko, L. N., Grinenko, V. A., Lein, A. Y., Smith, J. W., & Pankina, R. G. (1991). Lithospheric Sources of Sulphur. In Stable Isotopes: Natural and Anthropogenic Sulphur in the Environment (pp. 65–132). SCOPE-43.

Nozaki, T., Nagase, T., Ushikubo, T., Shimizu, K., & Ishibashi, J. I. (2020). Microbial Sulfate Reduction Plays an Important Role at the Initial Stage of Subseafloor Sulfide Mineralization. *Geology, 49*(2), 222-227.

Ohfuji, H., & Rickard, D. (2005). Experimental Syntheses of Framboids—a Review. *Earth-Science Reviews, 71*(3–4), 147–170.

Ohmoto, H., & Goldhaber, M. B. (1997). Sulfur and Carbon Isotopes. Geochemistry of Hydrothermal Ore Deposits (3rd ed.).

Orr, W. L. (1974). Changes in Sulfur Content and Isotopic Ratios of Sulfur during Petroleum Maturation—Study of Big Horn Basin Paleozoic Oils. *AAPG Bulletin, 58*(11), 2295-2318.

Osinski, G. R. (2005). Hydrothermal Activity Associated with the Ries Impact Event, Germany. *Geofluids, 5*(3), 202–220.

Osinski, G. R., Cockell, C. S., Pontefract, A., & Sapers, H. M. (2020). The Role of Meteorite Impacts in the Origin of Life. *Astrobiology, 20*(9), 1121–1149.

Osinski, G. R., Grieve, R. A., Chanou, A., & Sapers, H. M. (2016). The "Suevite" Conundrum, Part 1: The Ries Suevite and Sudbury Onaping Formation Compared. *Meteoritics & Planetary Science, 51*(12), 2316–2333.

Osinski, G. R., Grieve, R. A. F., & Spray, J. G. (2004). The Nature of the Groundmass of Surficial Suevite from the Ries Impact Structure, Germany, and Constraints on Its Origin. *Meteoritics & Planetary Science, 39*(10), 1655–1683.

Osinski, G.R., Tornabene, L.L., Banerjee, N.R., Cockell, C.S., Flemming, R., Izawa, M.R., McCutcheon, J., Parnell, J., Preston, L.J., Pickersgill, A.E., & Pontefract, A. (2013). Impact-Generated Hydrothermal Systems on Earth and Mars. *Icarus, 224*(2).

Pache, M., Reitner, J., & Arp, G. (2001). Geochemical Evidence for the Formation of a Large Miocene "Travertine" Mound at a Sublacustrine Spring in a Soda Lake (Wallerstein Castle Rock, Nördlinger Ries, Germany). *Facies, 45*(1), 211–230.

Parnell, J., Boyce, A., Thackrey, S., Muirhead, D., Lindgren, P., Mason, C., Taylor, C., Still, J., Bowden, S., Osinski, G.R., & Lee, P. (2010). Sulfur Isotope Signatures for Rapid Colonization of an Impact Crater by Thermophilic Microbes. *Geology, 38*(3), 271–274.

Passier, H. F., Middelburg, J. J., de Lange, G. J., & Böttcher, M. E. (1999). Modes of Sapropel Formation in the Eastern Mediterranean: Some Constraints Based on Pyrite Properties. *Marine Geology, 153*(1–4), 199–219.

Pohl, J., Poschlod, K., Reimold, W. U., Meyer, C., & Jacob, J. (2010). Ries Crater, Germany: The Enkingen Magnetic Anomaly and Associated Drill Core SUBO 18. In Large Meteorite Impacts and Planetary Evolution IV.

Pohl, J., Stöffler, D., Gall, H. V., & Ernstson, K. (1977). The Ries Impact Crater. In Impact and Explosion Cratering (pp. 343–404).

Rampe, E.B., Blake, D.F., Bristow, T.F., Ming, D.W., Vaniman, D.T., Morris, R.V., Achilles, C.N., Chipera, S.J., Morrison, S.M., Tu, V.M., & Yen, A.S. (2020). Mineralogy and Geochemistry of Sedimentary Rocks and Eolian Sediments in Gale Crater, Mars: A Review after Six Earth Years of Exploration with Curiosity. *Geochemistry, 80*(2), 125605.

Reese, B. K., Anderson, M. A., & Amrhein, C. (2008). Hydrogen Sulfide Production and Volatilization in a Polymictic Eutrophic Saline Lake, Salton Sea, California. *Science of The Total Environment, 406*(1–2), 205–218.

Reimold, W. U., Hansen, B. K., Jacob, J., Artemieva, N. A., Wünnemann, K., & Meyer, C. (2012). Petrography of the Impact Breccias of the Enkingen (SUBO 18) Drill Core, Southern Ries Crater, Germany: New Estimate of Impact Melt Volume. *Geological Society of America Bulletin, 124*(1–2), 104–132.

Reimold, W. U., McDonald, I., Schmitt, R. T., Hansen, B., Jacob, J., & Koeberl, C. (2013). Geochemical Studies of the SUBO 18 (Enkingen) Drill Core and Other Impact Breccias from the Ries Crater, Germany. *Meteoritics & Planetary Science, 48*(9), 1531-1571.

Rickard, D. (2021). Geochemistry of Framboids. In Framboids (pp. 169–190).

Rullkötter, J., Littke, R., & Schaefer, R. G. (1990). Characterization of Organic Matter in Sulfur-Rich Lacustrine Sediments of Miocene Age (Nördlinger Ries, Southern Germany). In Geochemistry of Sulfur in Fossil Fuels (pp. 149–169).

Sakai, H. (1957). Fractionation of Sulphur Isotopes in Nature. *Geochimica et Cosmochimica Acta, 12*(1–2), 150–169.

Sakai, H. (1968). Isotopic Properties of Sulfur Compounds in Hydrothermal Processes. *Geochemical Journal, 2*(1), 29–49.

Sandford, S. A., Nuevo, M., Bera, P. P., & Lee, T. J. (2020). Prebiotic Astrochemistry and the Formation of Molecules of Astrobiological Interest in Interstellar Clouds and Protostellar Disks. *Chemical Reviews, 120*(11), 4616–4659.

Sapers, H.M., Osinski, G.R., Flemming, R.L., Buitenhuis, E., Banerjee, N.R., Tornabene, L.L., Blain, S., & Hainge, J. (2017). Evidence for a Spatially Extensive Hydrothermal System at the Ries Impact Structure, Germany. *Meteoritics & Planetary Science, 52*(2), 351–371.

Schaefer, B., Grice, K., Coolen, M.J., Summons, R.E., Cui, X., Bauersachs, T., Schwark, L., Böttcher, M.E., Bralower, T.J., Lyons, S.L., & Freeman, K.H. (2020). Microbial Life in the Nascent Chicxulub Crater. *Geology, 48*(4), 328-332.

Schaefer, B., Schwark, L., Böttcher, M. E., Smith, V., Coolen, M. J., & Grice, K. (2022). Paleoenvironmental Evolution during the Early Eocene Climate Optimum in the Chicxulub Impact Crater. *Earth and Planetary Science Letters, 589*, 117589.

Schwenzer, S. P., & Kring, D. A. (2009). Impact-generated Hydrothermal Systems Capable of Forming Phyllosilicates on Noachian Mars. *Geology, 37*(12), 1091-1094.

Seal, R. R. (2006). Sulfur Isotope Geochemistry of Sulfide Minerals. *Reviews in Mineralogy and Geochemistry, 61*(1), 633–677.

Sharp, Z. (2017). Principles of Stable Isotope Geochemistry (2nd ed.).

Sim, M. S., Bosak, T., & Ono, S. (2011). Large Sulfur Isotope Fractionation Does Not Require Disproportionation. *Science, 333*(6038).

Sim, M. S., Sessions, A. L., Orphan, V. J., & Adkins, J. F. (2019). Precise Determination of Equilibrium Sulfur Isotope Effects during Volatilization and Deprotonation of Dissolved H_2S. *Geochimica et Cosmochimica Acta, 248*, 242–251.

Squyres, S.W., Grotzinger, J.P., Arvidson, R.E., Bell III, J.F., Calvin, W., Christensen, P.R., Clark, B.C., Crisp, J.A., Farrand, W.H., Herkenhoff, K.E., & Johnson, J.R. (2004). In Situ Evidence for an Ancient Aqueous Environment at Meridiani Planum, Mars. *Science, 306*(5702), 1709–1714.

Stetter, K. O. (1988). Archaeoglobus Fulgidus Gen. Nov., Sp. Nov.: A New Taxon of Extremely Thermophilic Archaebacteria. *Systematic and Applied Microbiology, 10*(2), 172–173.

Stetter, K. O., Lauerer, G., Thomm, M., & Neuner, A. (1987). Isolation of Extremely Thermophilic Sulfate Reducers: Evidence for a Novel Branch of Archaebacteria. *Science, 236*(4803), 822–824.

Stöffler, D. (1977). Research Drilling Nördlingen 1973: Polymict Breccias, Crater Basement, and Cratering Model of the Ries Impact Structure. *Geologica Bavarica, 75*, 443–458.

Stöffler, D., Artemieva, N. A., Wünnemann, K., Reimold, W. U., Jacob, J., Hansen, B. K., & Summerson, I. A. (2013). Ries Crater and Suevite Revisited-Observations and Modeling Part I: Observations. *Meteoritics & Planetary Science, 48*(4), 515–589.

Stüeken, E. E., Tino, C., Arp, G., et al. (2020). Nitrogen Isotope Ratios Trace High-pH Conditions in a Terrestrial Mars Analog Site. *Science Advances, 6*(9). eaay3440.

Sturm, S., Wulf, G., Jung, D., & Kenkmann, T. (2013). The Ries Impact, a Double-Layer Rampart Crater on Earth. *Geology, 41*(5), 531–534.

Surkov, A., Böttcher, M. E., & Kuever, J. (2012). Sulphur Isotope Fractionation during the Reduction of Elemental Sulphur and Thiosulphate by Dethiosulfovibrio spp. *Isotopes in Environmental and Health Studies, 48*(1), 65–75.

Thode, H. G., Monster, J., & Dunford, H. B. (1961). Sulphur Isotope Geochemistry. *Geochimica et Cosmochimica Acta, 25*(3), 159–174.

Vaniman, D.T., Bish, D.L., Ming, D.W., Bristow, T.F., Morris, R.V., Blake, D.F., Chipera, S.J., Morrison, S.M., Treiman, A.H., Rampe, E.B., & Rice, M. (2014). Mineralogy of a Mudstone at Yellowknife Bay, Gale Crater, Mars. *Science, 343*(6169).

Viola, D., McEwen, A. S., Dundas, C. M., & Byrne, S. (2017). Subsurface Volatile Content of Martian Double-Layer Ejecta (DLE) Craters. *Icarus, 284*, 325–343.

von Engelhardt, W. (1997). Suevite Breccia of the Ries Impact Crater, Germany: Petrography, Chemistry and Shock Metamorphism of Crystalline Rock Clasts. *Meteoritics & Planetary Science, 32*(4), 545–554.

von Engelhardt, W. (1990). Distribution, Petrography and Shock Metamorphism of the Ejecta of the Ries Crater in Germany—a Review. *Tectonophysics, 171*(1–4), 259–273.

von Gehlen, K., & Nielsen, H. (1985). Sulfur Isotopes and the Formation of Stratabound Lead-Bearing Triassic Sandstones in Northeastern Bavaria. *Geologisches Jahrbuch, D, 70*, 212–223.

Watanabe, Y., Farquhar, J., & Ohmoto, H. (2009). Anomalous Fractionations of Sulfur Isotopes During Thermochemical Sulfate Reduction. *Science, 324*(5925).

Weber, A., & Jørgensen, B. B. (2002). Bacterial Sulfate Reduction in Hydrothermal Sediments of the Guaymas Basin, Gulf of California, Mexico. Deep Sea Research Part I: Oceanographic Research Papers, 49(5), 827–841.

Westrich, J. T., & Berner, R. A. (1984). The Role of Sedimentary Organic Matter in Bacterial Sulfate Reduction: The G Model Tested. *Limnology and Oceanography, 29*(2), 236–249.

Winkler, H. (1972). Das Grundwasser Im Nördlinger Ries Unter Berücksichtigung Der Hydrologischen Und Hydrochemischen Beziehungen Zum Speichergestein. Ludwig-Maximilians-Universität: München.

Wolf, M. (1977). Kohlenpetrographische Untersuchungen der See-Sedimente der Forschungsbohrung Nördlingen 1973 und Vergleich mit anderen Untersuchungsergebnissen aus dem Ries. *Geologica Bavarica, 75*, 127-138.

Wordsworth, R., Knoll, A. H., Hurowitz, J., Baum, M., Ehlmann, B. L., Head, J. W., & Steakley, K. (2021). A Coupled Model of Episodic Warming, Oxidation and Geochemical Transitions on Early Mars. *Nature Geoscience, 14*(3), 127–132.

Wortmann, U. G., Bernasconi, S. M., & Böttcher, M. E. (2001). Hypersulfidic Deep Biosphere Indicates Extreme Sulfur Isotope Fractionation during Single-Step Microbial Sulfate Reduction. *Geology, 29*(7), 647.

Yang, S., Schulz, H. M., Horsfield, B., Schovsbo, N. H., Grice, K., & Zhang, J. (2020). Geological Alteration of Organic Macromolecules by Irradiation: Implication for Organic Matter Occurrence on Mars. *Geology, 48*(7), 713–717.

Zhang, T., Amrani, A., Ellis, G. S., Ma, Q., & Tang, Y. (2008). Experimental Investigation on Thermochemical Sulfate Reduction by H2S Initiation. *Geochimica et Cosmochimica Acta, 72*(14), 3518-3530.

Chapter 2

Nitrogen isotope ratios trace high pH conditions in a terrestrial Mars analog site

Preface:

The contents of this chapter, have been published in a modified form as:

Stüeken, E. E.*, Tino, C.*, Arp, G., Jung, D., & Lyons, T. W. (2020). Nitrogen isotope ratios trace high-pH conditions in a terrestrial Mars analog site. Science advances, 6(9), eaay3440. *These authors contributed equally to this work.

Abstract

High-pH alkaline lakes are among the most productive ecosystems on Earth and prime targets in the search for life on Mars; however, a robust proxy for such settings does not yet exist. Nitrogen isotope fractionation resulting from NH_3 volatilization at high pH has the potential to fill this gap. To validate this idea, we analyzed samples from the Nördlinger Ries, a Miocene impact crater lake that displayed pH values up to 9.8 as inferred from mineralogy and aqueous modelling. Our data show a peak in $\delta^{15}N$ of +17‰ in the most alkaline facies, followed by a gradual decline to around +5‰, concurrent with the proposed decline in pH, highlight the utility of nitrogen isotopes as a proxy for high-pH conditions. In combination with independent mineralogical indicators for high alkalinity, nitrogen isotopes can provide much needed quantitative constraints on ancient atmospheric pCO_2 and thus climatic controls on early Earth and Mars.

Introduction

Jezero Crater, the designated landing site for the Mars 2020 rover, possesses smectite clays and carbonate sequences that imply circumneutral-to-alkaline aqueous conditions during the earliest portions of the crater's lacustrine history (Ehlmann et al., 2008; Goudge et al., 2015). However, while mineral associations mirror a combination of salinities, temperatures, redox and pH (e.g., Chevrier et al., 2007), a specific approximation of ancient pH conditions is not possible on this basis. Developing a method for distinguishing between circumneutral and high-pH environments is astrobiologically significant, because high-pH alkaline lakes are the most bioproductive natural aquatic systems on Earth, and their productivity is almost exclusively driven by Bacteria and Archaea (Grant and Jones, 2000). The Miocene Ries crater lake in southern Germany (**Fig. 2.1**) is an ideal testbed for testing and calibrating such proxies.

The Nördlinger Ries is widely recognized as an analog for Martian craters and specifically related ejecta fluidization, post-impact hydrothermal activity and aqueous sedimentation on early Mars (Arp et al., 2013; Kenkmann and Schönian, 2006; Osinski et al., 2013; Sturm et al., 2013). The Ries crater formed about 14.8 million years ago through an asteroid impact that excavated 500-650 m of Triassic-Jurassic and Tertiary sedimentary rocks and over 2 km of the underlying Variscan crystalline basement. The resulting transient cavity collapsed quickly, leaving behind a 600 m deep and 26 km wide depression that filled with water and sediments over time (Pohl et al., 1977) and hosted diverse biological assemblages throughout its approximately 0.3-2 million year history (Arp et al.,

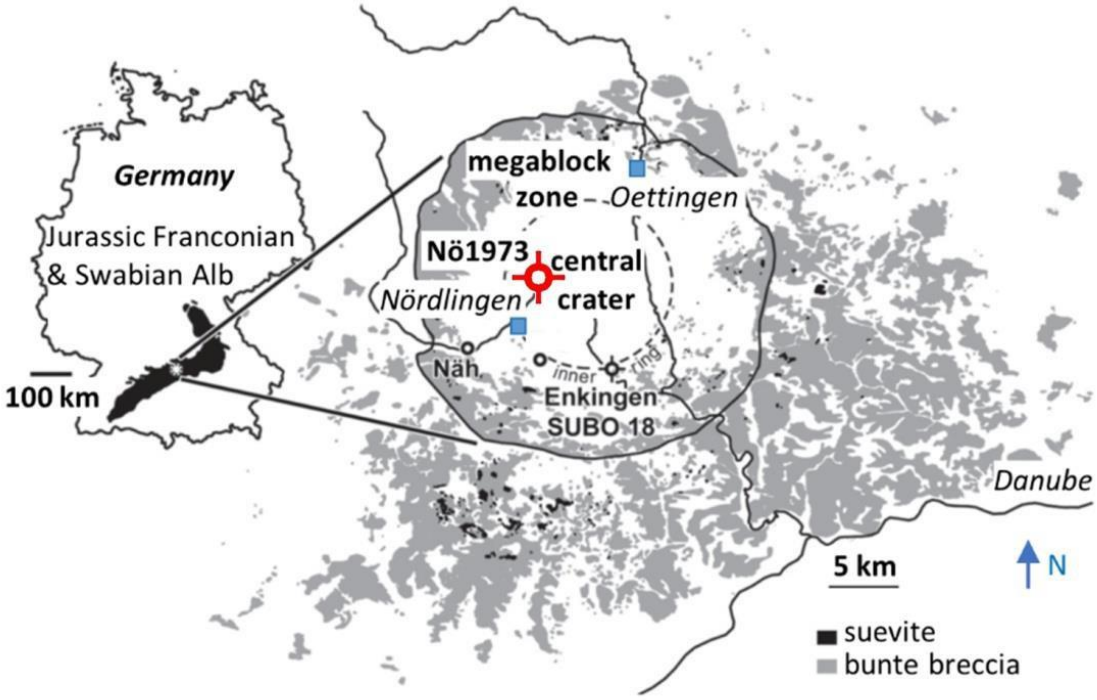

Figure 2.1 Map showing the location of the Ries crater and the Nördlingen 1973 drill hole. Adapted from Arp et al. (2013).

2013; Füchtbauer et al., 1977). Partial melting of target rocks enhanced physical and chemical weathering with significant effects on sediment composition (Arp et al., 2019) and lake water chemical evolution (Sturm et al., 2013) – differing from standard terrestrial lake basins but potentially analogous to Martian basins.

Specifically, the mineralogy of the sediments deposited within the crater on top of the crater suevite (a melt-bearing, polymict impact breccia) indicates that weathering of crystalline-rock-derived lithic breccias and glassy melt fragments had a substantial effect on the chemistry of the lake waters (Arp et al., 2013). In particular, the abundance of the zeolite minerals analcime and clinoptilolite in the laminite member of the lower sediment package and the near absence of diatom tests in this interval (**Fig. 2.2**), paired with co-

varying carbon and oxygen isotopes, have been taken as evidence for high alkalinity that resulted from silicate weathering and strongly evaporative conditions in a closed-basin lake (Arp et al., 2013; Füchtbauer et al., 1977; Rothe and Hoefs, 1977). Zeolites have also been detected on Mars where they are thought to have formed during aqueous alteration of volcanic glass (Ruff, 2004). Aqueous geochemical modelling of the Ries lake suggests a pH of up to 9.8 during this zeolite-rich interval (Arp et al., 2013). The lake likely became progressively more saline over time as the pH decreased when inflowing waters became chemically controlled by weathering of the Bunte Breccia and Jurassic sedimentary rocks (Arp et al., 2013). This model would have important implications for our understanding of habitats in Martian crater lakes. First, it is likely that weathering of suevite-like deposits on Mars, including impact and volcanic breccia, would result in high-pH waters in many fresh impact settings. This effect would likely be enhanced on Mars because the crust is relatively more mafic, and glasses of mafic composition have been shown to elevate the pH more strongly than silica-rich glasses (cf. Garrels and Mackenzie, 1967; Gislason and Eugster, 1987). Second, significant shifts in pH due to chemical lake evolution can be expected in terranes with layered composition, i.e., where rapidly weathering ash and melt fragments initially create high-pH conditions before weathering of more crystalline basement rocks shifts the pH towards neutral values, similar to the Ries crater. Indeed, although basaltic rocks prevail in many Martian regions at the surface, including Jezero crater, there is increasing indication of a more diverse lithologic crust composition including felsic magmatic rocks (Sautter et al., 2015). This observation also applies to Gale crater, which hosted a permanent, potentially habitable lake (Grotzinger et al., 2014). It is

therefore important to develop a geochemical proxy that is sensitive to high-pH conditions in the sedimentary record of Mars as well as the early Earth, where relatively unstable proxies such as zeolites and biomarkers may not be preserved. The relevance of these conditions is elevated by their strong impacts on life.

Boron isotopes are commonly used as a pH proxy in the marine realm, but this technique requires knowledge of the boron isotopic composition of the water column. Other proxies, such as rare earth elements or calcium isotopes also require additional parameters, such as source rock composition or alkalinity. In this study we tested nitrogen isotopes as an alternative approach. During diagenesis, degrading biomass releases NH_4^+, which partitions into NH_3 with a pKa of 9.2 at standard pressure and temperature. NH_3 is volatile and can escape into the atmosphere, as is observed in modern alkaline lakes during water column overturn (Jellison et al., 1993). This process imparts a large isotopic fractionation ($\varepsilon \approx \delta_{product} - \delta_{reactant}$) of -42‰ in $\delta^{15}N$ (= $[(^{15}N/^{14}N)_{sample}/(^{15}N/^{14}N)_{air} -1] \times 1000$), rendering the residual NH_4^+ isotopically heavy (Li et al., 2012). The fractionation decreases with temperature, but it is still as high as -33‰ at 70°C. High $\delta^{15}N$ values > 10‰ in sediments from evaporitic lakes have therefore been used as indicators of elevated pH during the time of deposition (Stüeken et al., 2015; Talbot and Johannessen, 1992; Collister and Hayes, 1973; Menzel et al., 2013). However, it is so far unknown if such large isotopic fractionation can also be produced by redox processes (e.g., denitrification) in stratified saline lakes under circum-neutral pH. The chemical trends inferred from the Ries crater (**Fig. 2.2**; Arp et al., 2013) can thus serve as an ideal natural laboratory to explore the utility

of $\delta^{15}N$ in consolidating a multitude of geochemical measurements into single, reliable proxy for high-pH conditions.

Sampling

We collected samples from the Nördlingen 1973 drill core (**Fig. 2.2**), which was drilled in the central crater and intersects most of the lacustrine sedimentary infill. The basal member, which sits directly on top of the suevite, is composed of sandstones and conglomerates of reworked suevite and basement rocks that may have been deposited in debris flows (Füchtbauer et al., 1977). This unit transitions into a laminated marl with bituminous shale intercalations (laminite member), representing a stratified permanent lake. The laminite member is followed by a greenish-grey poorly stratified marlstone (marl member), which has been interpreted as evidence of shallowing (Füchtbauer et al., 1977). The marlstone is capped by a grey claystone with thin allochthonous coal seams as well as gypsum pseudomorphs that likely represent highly fluctuating water depths and salinities (Arp et al., 2017). We selected samples from the top of the basal member to the middle of the clay member with a resolution of a few meters (**Table 2.1**).

Results

At the base of the laminite member, $\delta^{15}N$ shows a sharp increase over an interval of about 15 m from values around +3‰ to a maximum of +17‰ (**Table 2.1**, **Fig. 2.2**). The

values then decrease gradually towards +5‰ at the top of the core. The interval with the highest values (> +10‰) in the bituminous laminite member also contains a greater abundance of zeolites and much lower abundances of macrofossils (**Fig. 2.2**; Arp et al., 2013). The total nitrogen contents [TN] broadly covaries with total organic carbon [TOC] (**Fig. 2.3a**), indicating that most of the nitrogen is derived from buried organic matter. This relationship does not preclude the presence of clay-bound ammonium, which inevitably forms during diagenesis (Müller, 1977) and may explain some of the deviations in the TN-TOC cross-plot, but this process does not impart a significant isotopic fractionation (< 2‰; Robinson et al., 2012). Horizons with unusually high TOC correspond to bitumen enrichments in the laminite member and thin coal beds in the clay member. $\delta^{15}N$ does not covary with C/N ratios (**Fig. 2.3c**), indicating that $\delta^{15}N$ values have not suffered from metamorphic alteration (Stüeken et al., 2017), which is consistent with post-depositional geothermal heating to a maximum of 60°C as inferred from vitrinite reflectance (Wolf, 1977). The slight covariance between $\delta^{15}N$ and TN (**Fig. 2.3b**) is most likely a primary feature linked to environmental conditions that raised $\delta^{15}N$ while favoring biomass preservation under anoxic conditions, as indicated by concurrently high TOC (Fig. **2.3a**). $\delta^{13}C_{org}$ initially increases gradually up-section in the laminite member from about -27‰ to -20‰ before dropping back to a more constant value of around -26‰ in the overlying strata. This trend broadly agrees with previous measurements of $\delta^{13}C_{carb}$ (**Fig. 2.2**; Rothe and Hoefs, 1977), suggesting that primary producers are tracking the composition of dissolved CO_2, which likely becomes isotopically heavier as a result of evaporation (Horton et al., 2016).

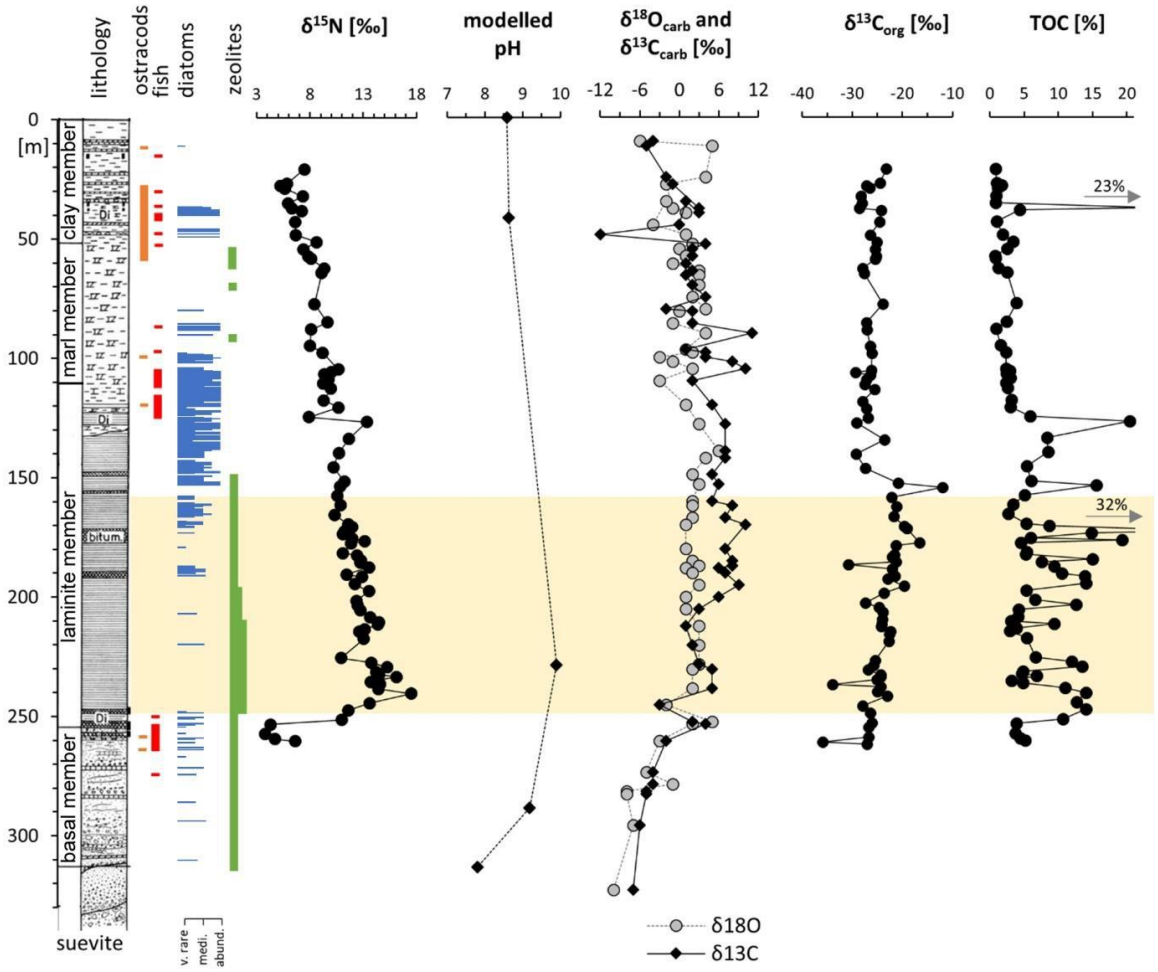

Figure 2.2 Stratigraphic trends in the Nördlingen 1973 drill core. Orange-shading indicates inferred hyperalkaline interval with coinciding high modelled pH and high $\delta^{15}N$, $\delta^{18}O_{carb}$, $\delta^{13}C_{carb}$ and TOC, scarcity of macrofauna and abundant diagenetic zeolite minerals. Lithostratigraphy is taken from Füchtbauer et al. (1977), $\delta^{18}O_{carb}$ and $\delta^{13}C_{carb}$ are taken from Rothe & Hoefs (1977), the pH model is taken from Arp et al. (2013). Diatom abundances according to Schauderna (1983).

Table 2.1 Geochemical data from core Nördlingen 1973. Average reproducibility for $\delta^{15}N$ and $\delta^{13}C$ are 0.4‰ (1SD) and 0.1‰, respectively. Average relative errors (1SD/mean) are 6.5% for TN and 4.4% for TOC. Notes highlight enrichment in organic carbon.

Depth [m]	Notes	$\delta^{15}N$ [‰]	$\delta^{13}C$ [‰]	TN [wt%]	TOC [wt%]
Claystone member (cm-scale laminated mud, dark gray):					
21.55		7.47	-23.23	0.04	0.88
27.55		5.86	-24.41	0.07	1.01
28.55		5.21	-27.23	0.10	1.68
29.55		5.65	-26.49	0.07	1.13
32.95		7.31	-28.25	0.09	0.95
35.95		5.92	-28.03	0.09	0.87
37.95	coal seam	6.31	-28.61	0.59	23.46
38.95		7.23	-24.18	0.17	4.37
43.58		6.62	-24.61	0.08	0.99
49.1		6.64	-26.37	0.12	1.87
Marl member (calcareous pale gray mudstone, massive to cm-scale lamination):					
52.1		8.63	-25.09	0.16	3.36
55.1		7.39	-25.45	0.14	2.56
58.1		7.84	-25.18	0.08	0.77
59.1		8.09	-25.42	0.06	0.82
63.1		9.35	-27.96	0.12	1.21
65.1		9.10	-27.62	0.16	2.51
78		8.43	-23.88	0.24	3.87

85.7		9.63	-27.14	0.14	2.43
88.7		8.11	-27.10	0.11	0.95
95.5		7.99	-26.41	0.10	1.54
98.5		9.20	-26.10	0.12	2.32
105.5		10.65	-26.17	0.16	2.39
106.5		10.02	-29.33	0.17	2.96
107.5		9.35	-26.38	0.16	2.46
109.5		9.75	-27.18	0.16	3.02
Laminite member (mm-scale plane laminated, carbonaceous to bituminous):					
111.5		9.24	-27.46	0.17	2.32
113.5		9.96	-25.57	0.13	2.59
118.5		9.29	-27.96	0.14	3.14
121.5		10.68	-27.14	0.14	3.00
125.5		7.91	-26.81	0.22	5.88
127.5	bituminous	13.33	-29.19	0.48	20.44
134.5		11.65	-23.53	0.36	8.32
140.5		10.70	-29.29	0.34	8.50
146.5		10.20	-27.42	0.24	5.42
152.5		11.23	-20.86	0.29	6.00
154.5	bituminous	10.80	-11.96	0.44	15.56
158.5		10.57	-22.12	0.23	5.05
162.5		10.85	-21.14	0.21	3.43
166.5		10.31	-21.70	0.18	2.70
170.5		11.58	-19.64	0.25	5.33

171.5		11.95	-19.10	0.38	8.65
173.5	bituminous	11.25	nd	0.31	31.82
174.5	bituminous	11.08	nd	0.28	14.84
176.5		11.94	nd	0.26	5.96
177.5	bituminous	13.12	-16.62	0.44	19.30
178.5		11.86	-21.23	0.24	4.51
182.5		11.10	-21.62	0.30	5.37
183.5		12.42	-22.07	0.27	5.21
185.5	bituminous	12.78	-21.26	0.55	14.96
186.5	bituminous	12.72	-30.84	0.37	7.57
188.5	bituminous	13.52	-21.99	0.43	9.39
191.5	bituminous	11.42	-21.48	0.53	10.50
192.5	bituminous	12.85	-22.90	0.43	13.90
195.5	bituminous	12.20	-19.65	0.38	13.98
198.5		13.53	-23.66	0.41	5.28
202.5		12.34	-27.38	0.65	6.62
204.5	bituminous	12.46	-24.65	0.78	12.58
206.5		12.73	-23.91	0.32	4.21
209.5		13.66	-24.03	0.30	4.14
211.5		14.48	-24.16	0.22	3.05
212.5		14.38	-24.20	0.58	9.36
214.5		13.13	-22.35	0.33	3.84
215.5		12.63	-22.57	0.30	2.95
218.5		13.05	-22.72	0.49	5.39

226.5		10.91	-25.47	0.82	6.64
228.5	bituminous	13.73	-25.76	0.61	11.98
230.5	bituminous	15.24	-26.84	0.61	13.50
232.5		14.19	-24.36	0.33	4.85
233.5		14.46	-24.32	0.34	4.71
234.5		16.09	-25.09	0.35	6.87
236.5		13.67	-34.00	0.30	3.14
237.5		14.56	-24.31	0.25	4.85
239.5	bituminous	14.39	-24.94	0.44	11.00
241.5	bituminous	17.47	-23.03	0.59	13.98
245.5	bituminous	13.60	-27.99	0.43	12.66
248.5	bituminous	11.60	-26.44	0.43	13.99
252.5	bituminous	10.95	-26.09	0.19	10.68
254.5		4.29	-26.73	0.12	3.85
Basal member (sandstone with interlaminated carbonaceous mudstone):					
258.5		3.82	-26.71	0.11	3.72
260.5		4.73	-35.97	0.13	4.45
261.5		6.64	-27.03	0.10	5.20

Discussion

Nitrogen isotopes can be fractionated by several biogeochemical processes. The major source of nitrogen to surface environments is biological N_2 fixation with a small fractionation of -4‰ to 0‰ (reviewed by Stüeken et al., 2016). The most important

mechanisms with fractionations of more than 10‰ include nitrification of NH_4^+ to NO_3^- (ε ≈ -1 to -25‰), reduction of NO_3^- to N_2 (denitrification, ε ≈ -5 to -30‰) or NH_4^+ (ε ≈ -30‰), biological assimilation of NH_4^+ (ε ≈ -4 to -27‰), and dissociation of NH_4^+ to NH_3 followed by volatilization of NH_3 gas (ε ≈ -42‰ at 25°C; Li et al., 2012). These fractionations can be recorded in the rock record if organisms that consume the products or residual reactants get buried in sediments. For example, in modern marine sediments, the average bulk nitrogen isotopic composition is +5‰ (Tesdal et al., 2013), which results from partial denitrification in suboxic waters, followed by assimilation of the residual isotopically enriched nitrate into biomass, which transfers this signature to sedimentary archives during burial.

The isotopic effect of nitrification, which occurs when some biomass is remineralized under oxic conditions, is rarely expressed because nitrification rapidly goes to completion at even micromolar levels of dissolved oxygen (Lipschultz et al., 1990). Only seasonal occurrences of partial nitrification have been reported from the Bering Sea and Lake Kinneret (Hades et al., 2009; Morales et al., 2014). It is important to note that this process generates two pools of isotopically distinct bioavailable nitrogen (nitrate and ammonium)

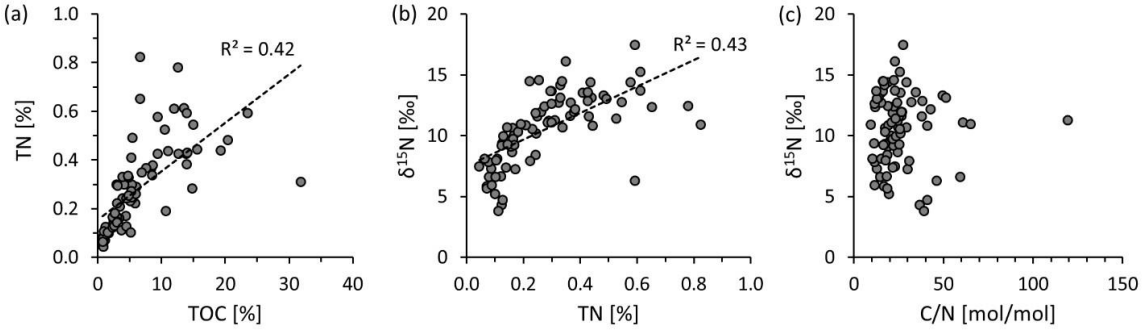

Figure 2.3 Carbon-nitrogen scatter plots. (a) Covariance between total organic carbon and total nitrogen. (b) Covariance between total nitrogen $\delta^{15}N$. (c) Lack of covariance between molar organic carbon to total nitrogen ratios and $\delta^{15}N$ indicating absence

and therefore can result in large isotopic heterogeneity. Similarly, partial assimilation of NH_4^+ creates isotopically light biomass and a residual pool of enriched NH_4^+, which may be assimilated elsewhere in the same basin. If partial assimilation of NH_4^+ dominates sedimentary nitrogen isotopes, one would expect a range from very negative to very positive values. In contrast, volatilization of NH_3 gas leaves behind a uniform, isotopically enriched pool of dissolved fixed nitrogen – similar to partial denitrification. The relatively high and fairly uniform $\delta^{15}N$ values of up to +17‰ in the Ries crater are therefore most plausibly explained by either denitrification or NH_3 volatilization, but the two mechanisms cannot be unambiguously distinguished from each other via $\delta^{15}N$ data alone.

The vast majority of Holocene lakes display $\delta^{15}N$ values in the range of +1 to +4‰ (McLaughlan et al., 2013), which is likely a reflection of widespread biological N_2 fixation in terrestrial and lacustrine environments with only minor secondary processing of fixed nitrogen. Significantly higher values up to +18‰ have to our knowledge only been reported from evaporitic modern lakes (Newell et al., 2017; Talbot and Johannessen, 1992). One possible explanation for those high values is partial loss of NH_3 under high-pH conditions. This mechanism requires an oxygen-deficient environment such that diagenetically produced NH_4^+ is not quantitatively oxidized before conversion to NH_3 and escape into the atmosphere. However, redox stratification also leaves open the possibility that the high $\delta^{15}N$ values from these environments are caused by denitrification rather than NH_3 escape.

In the case of the Ries crater sediments, $\delta^{15}N$ covaries with pH values modelled by Arp et al. (2013) (**Fig. 2.2**), who used modern groundwaters to infer the composition of

fluids in equilibrium with Ries-related impact facies. $\delta^{15}N$ also covaries with abundances of analcime and clinoptilolite, which form during alteration of glass – a process that is known to result in high alkalinity and high pH in experimental and natural settings (Gislason and Eugster, 1987; although the presence of these minerals alone is not diagnostic of a particular pH range). When the alkaline fluids generated by this water-glass interaction undergo evaporation, pH increases further because protons are consumed by reaction with HCO_3^- (Garrels and Mackenzie, 1967). To further test the plausibility of these processes, we constructed a model in Geochemist's Workbench® (see Methods) where we first let suevite glass react with water and then allowed the resulting fluid to evaporate (**Fig. 2.4a, 2.4b**). With the dissolution of only 0.4g/L of suevite glass (composition taken from Vennemann et al., 2001), the calculated pH of pure water buffered by atmospheric CO_2 increases to 8.3 (**Fig. 2.4a**). Subsequent evaporation raises the pH of this fluid to 9.3 (**Fig. 2.4b**). If the fluid is separated from the atmospheric CO_2 reservoir before reacting with the glass, as would be the case in the subsurface, the dissolution of 0.4g/L of glass would yield a pH of 10.2 (**Fig. 2.4a**). These values are consistent with previous models based on modern ground waters (Arp et al., 2013), and are high enough for the conversion of a significant fraction of NH_4^+ to NH_3 (**Fig. 2.4c**), followed by NH_3 volatilization and isotopic enrichment (**Fig. 2.4d**). The high $\delta^{15}N$ values in the lower bituminous laminite interval of the Ries crater (256-200 m core depth) are therefore consistent with the effects of high pH, enriching the information gained from the presence of clays, carbonates and zeolite minerals alone.

Arp et al. (2013) argued that the lake became progressively more saline over time (i.e., stratigraphically upwards in the core), but pH dropped when the major source rock of solutes switched from suevite and crystalline rocks to Bunte Breccia and Jurassic carbonate. A progressive increase in salinity and thus stagnation of the water column is supported by $\delta^{18}O_{carb}$ (**Fig. 2.2**; Rothe and Hoefs, 1977) and $\delta^{13}C_{org}$ (**Fig. 2.2**), which peak in the upper third of the bituminous laminite member (170-140 m core depth) and stay relatively elevated in the overlying marl member, consistent with high levels of evaporation

Figure 2.4 Model calculations and nitrogen behavior. (a) Model calculation of glass dissolution in nearly pure water with either fixed atmospheric *p*CO2 (buffered) or progressively consumed CO_2 (not buffered). The latter simulates a water-glass reaction in the subsurface. See appendix for details on input parameters. (b) Model calculation of evaporation of fluid after reaction with 0.4 g of glass from panel (a) and in constant equilibrium with atmospheric CO_2. Both scenarios of panel (a) result in the same evaporation effect, because the load of dissolved solids is the same. (c) pH-relationship of ammonium (NH_4^+) and ammonia (NH_3) at standard pressure and temperature. (d) Isotopic effect of NH_3 volatilization on residual dissolved NH_4^+ for kinetic and equilibrium fractionation models.

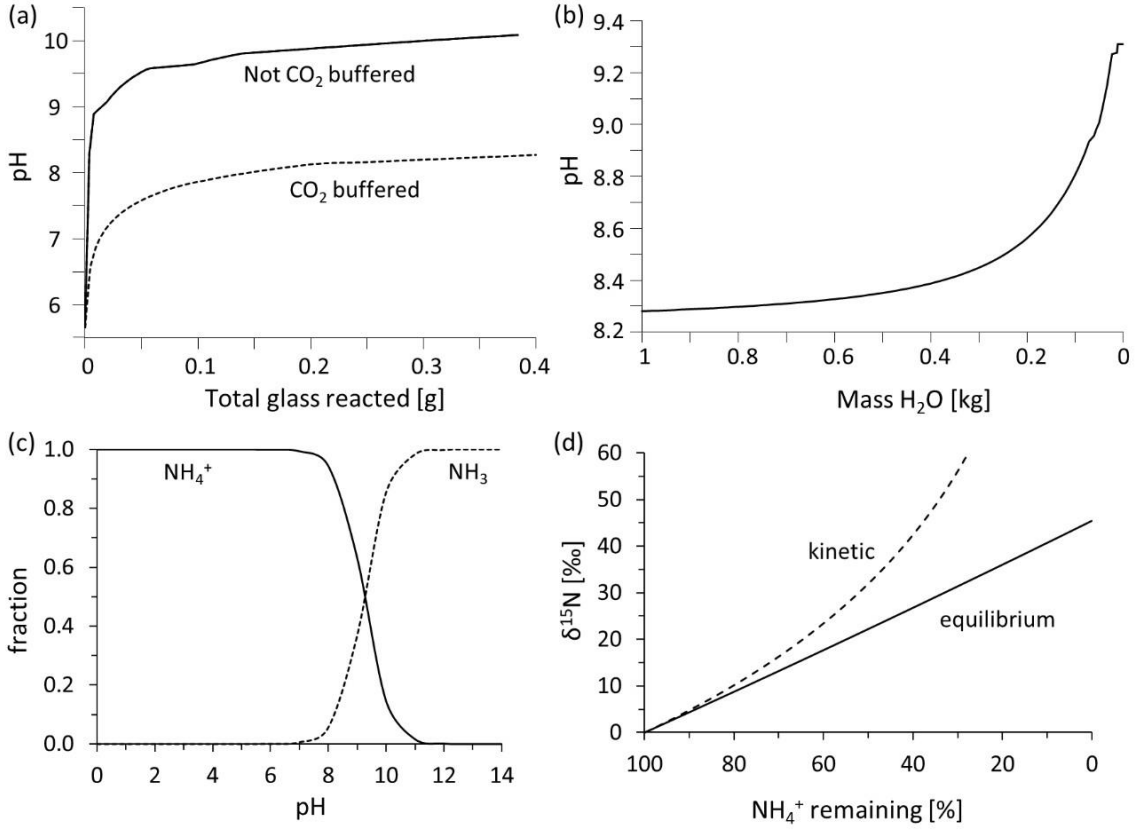

during this interval (Arp et al., 2013). Biomarker records further indicate anoxic bottom waters for major parts of the depositional history of the lake (Arp et al., 2013). The decline of $\delta^{15}N$ up-section despite a likely persistence of oxygen deficiency, starting from its peak at the base of the bituminous laminite member (256 m core depth), indicates that redox stratification was not the dominant cause of the strong isotopic enrichments in nitrogen isotopes lower in the core. Denitrification alone can therefore not explain these data. Instead, high pH conditions as inferred from the lower part of the core (256-200 m core depth) appear to have been necessary to generate $\delta^{15}N$ values significantly above +10‰. Our data thus provide strong evidence that $\delta^{15}N$ can serve as a pH indicator in paleolacustrine environments. The basic physicochemical nature of this proxy makes it readily extendable to Mars and high-pH bodies such as Enceladus and exoplanetary water worlds.

Conclusion

The nitrogen isotope record of the Miocene Ries crater lake shows unusually high $\delta^{15}N$ values up to +17‰ during an interval with independent mineralogical and paleontological evidence of high pH and redox stratification (Arp et al., 2013). $\delta^{15}N$ values decreased when the water chemistry of the lake transitioned to circum-neutral pH, despite a persistence of evidence for low oxygen conditions in lake bottom waters (monimolimnion). This combination of observations indicates that redox stratification was insufficient to generate $\delta^{15}N$ values above +10‰. Instead, high pH appears to have been

required, suggesting that NH_3 volatilization played a significant role in elevating $\delta^{15}N$. Our data are thus strong evidence that nitrogen isotopes can serve as a paleo-pH indicator around a threshold of ~9.2 – i.e., the pKa of the NH_4^+/NH_3 transformation. This proxy should be a valuable addition to future Mars exploration, because high-pH alkaline environments host the most bioproductive natural ecosystems on Earth (Grant and Jones, 2000), including the highest diversity of cyanobacteria (Zavarzin, 1993). The more mafic composition of the Martian crust compared to the crystalline basement (gneiss, granite, amphibolite) under the Ries crater should only serve to enhance the utility of this proxy, since weathering of mafic glass has a relatively stronger effect on raising the pH than felsic glass (Gislason and Eugster, 1987). Furthermore, numerous prebiotic reactions may have been facilitated in high-pH settings, including the formation of carbohydrates, the polymerization of HCN into amino acids, and the phosphorylation of nucleotides (Ferris and Hagan Jr., 1984; Kempe and Kazmierczak, 2002; Kim et al., 2011). Reduced, non-ammonium nitrogen compounds (e.g., HCN) have recently been observed within indigenous organic compounds of the Tissint meteorite (Steele et al., 2018). Such compounds may be indicative of electrochemical reduction of N_2 to NH_4^+ (Steele et al., 2018). These observations indicate that the nitrogen isotope ratios have the potential to serve as a powerful proxy for high pH on the Martian surface. $\delta^{15}N$ signals indicative of ammonia volatilization would allow distinguishing between high alkalinity and high pH. Such a distinction would have implications for atmospheric composition, because the co-occurrence of high total alkalinity based on mineralogical observations and circumneutral pH, under which ammonia volatilization is suppressed, would point towards relatively

elevated pCO_2, of at least 0.5 bar (Wordsworth et al., 2017). In contrast, a high pH, as suggested by high $\delta^{15}N$ values, would place an upper limit on pCO_2. An independent pH constraint would thus help address the longstanding problem of persistent liquid water despite a faint young Sun by helping constrain the amount of CO_2 in the ancient Martian atmosphere. $\delta^{15}N$ measurements in Martian sedimentary strata may be an important analytical tool in the upcoming era of sample return, helping to identify high-pH paleoenvironments with a high potential for habitability and an independent origin of life.

Materials and Methods

The outer rims of the core samples were trimmed with a manually operated rock chipper, and the interiors were hammered into sub-cm sized chips and dehydrated at 50°C for a minimum of 48 hours. The rock chips were then pulverized in a ball mill and stored in scintillation vials. For isotopic analyses, roughly 0.5 g of powder were decarbonated with 2 N HCl at 60°C overnight and washed three times with 18 MΩ DI-H_2O (Stüeken et al., 2015). The dried residues were weighed into tin capsules and analyzed for organic carbon and total nitrogen isotopes at the University of St Andrews, using an EA Isolink coupled to a MAT253 isotope ratio mass spectrometer via a Conflo IV. The data were calibrated with international reference materials USGS-40 and USGS-41. Long-term reproducibility was tracked with the rock standard SGR-1 (untreated), for which we obtained a $\delta^{15}N$ value of 17.4 ± 0.5‰ – in good agreement with previous studies (Dennen et al., 2006). Data are expressed in standard delta notation relative to VPDB for $\delta^{13}C_{org}$ and

relative to air for $\delta^{15}N$. To verify that acidification had no adverse effects on our isotopic data, a subset of samples was treated with 2N HCl a second time. The obtained results were within analytical precision of the first set of measurements with single acid treatments.

To test the plausibility of our interpretation, a geochemical model was constructed using the React module in Geochemist's Workbench. 1kg of H_2O in equilibrium with CO2 gas ($3.5 \cdot 10^{-4}$ bar) and O2 gas (0.2bar) in the Basis pane was reacted with suevite glass (Vennemann et al., 2001) simulated by SiO_2 (63.3mg), Al_2O_3 (14.7mg), FeO (5.2mg), MgO (3mg), CaO (4.3mg), Na_2O (2.7mg), and K_2O (2.8mg) in the Reactants pane. Elements were entered as oxides to simulate the amorphous nature of glass. For the model to run, the Basis needed to contain traces of each element, which were chosen as $SiO_{2(aq)}$ (0.1nM), Al^{3+} (0.1nM), Fe^{2+} (0.001nM), Mg^{2+} (1nM), Ca^{2+} (1nM), Na^{+} (1nM), K^{+} (1nM), Cl^{-} (1nM), and SO_4^{2-} (1nM). pH was used as a charge balance. These concentrations are so low that this is essentially pure water; changes in these concentrations by a factor of 10 had no effect on the outcome of the model. For models of a system that is buffered by the atmosphere, the fugacities of CO_2 and O_2 were fixed in the Reactants pane. Once the solution had equilibrated with the glass, the end composition of the new solution was transferred into the Basis. A new simulation was run where H_2O was progressively removed in the Reactants pane, simulating evaporation. Again, the fugacities of CO_2 and O_2 were fixed to simulate an atmosphere-buffered system. Results were plotted in Gtplot.

References

Arp, G., Blumenberg, M., Hansen, B.T., Jung, D., Kolepka, C., Lenz, O., Nolte, N., Poschlod, K., Reimer, A., & Thiel, V. (2013). Chemical and ecological evolution of the Miocene Ries impact crater lake, Germany: A reinterpretation based on the Enkingen (SUBO 18) drill core. *Geological Society of America Bulletin, 125*(7-8), 1125-1145.

Arp, G., Hansen, B.T., Pack, A., Reimer, A., Schmidt, B.C., Simon, K., & Jung, D. (2017). The soda lake-mesosaline halite lake transition in the Ries impact crater basin (drilling Löpsingen 2012, Miocene, southern Germany). *Facies, 63*, doi: 10.1007/s10347-10016-10483-10347.

Arp, G., Schultz, S., Karius, V., & Head III, J. W. (2019). Provenance, sedimentary particle impact preprocessing, and transport distances of conglomeratic constituents in the Miocene Ries impact crater: Implications for Gale Crater, Mars. *Icarus, 321*, 531-598.

Chevrier, V., Poulet, F., & Bibring, J. P. (2007). Early geochemical environment of Mars as determined from thermodynamics of phyllosilicates. *Nature, 448*(7157), 60-63.

Collister, J. W., & Hayes, J. M. (1973). In *Geochemical, biogeochemical, and sedimentological studies of the Green River formation, Wyoming, Utah, and Colorado* (Ed. M. L. Tuttle), U.S. Geological Survey, Denver, CO.

Dennen, K. O., Johnson, C. A., Otter, M. L., Silva, S. R., & Wandless, G. A. (2006). $\delta^{15}N$ and non-carbonate $\delta^{13}C$ values for two petroleum source rock reference materials and a marine sediment reference material. *U.S. Geological Survey Open-File Report 2006-1071*.

Ehlmann, B. L., Mustard, J.F., Fassett, C.I., Schon, S.C., Head III, J.W., Des Marais, D.J., Grant, J.A., & Murchie, S.L. (2008). Clay minerals in delta deposits and organic preservation potential on Mars. *Nature Geoscience, 1*(5), 355-358.

Ferris, J. P., & Hagan Jr., W. J. (1984). HCN and chemical evolution: the possible role of cyano compounds in prebiotic synthesis. *Tetrahedron, 40*(6), 1093-1120.

Füchtbauer, H., von der Brelie, G., Dehm, R., Förstner, U., Gall, H., & Höfling, R. (1977). Tertiary lake sediments of the Ries, research borehole Nördlingen 1973-A summary. *Geologica Bavarica, 75*, 13-19.

Garrels, R. M., & Mackenzie, F. T. (1967). In *Equilibrium concepts in natural water systems* (chap. 10, pp. 222-242). American Chemical Society.

Goudge, T. A., Mustard, J. F., Head, J. W., Fassett, C. I., & Wiseman, S. M. (2015). Assessing the mineralogy of the watershed and fan deposits of the Jezero crater paleolake system, Mars. *Journal of Geophysical Research: Planets, 120*(4), 775–808.

Gislason, S. R., & Eugster, H. P. (1987). Meteoric water-basalt interaction. I: A laboratory study. *Geochimica et Cosmochimica Acta, 51*(12), 2827-2840.

Grant, W. D., & Jones, B. E. (2000). Alkaline environments. *Encyclopaedia of Microbiology, 1*, 126-133.

Grotzinger, J. P., Sumner, D.Y., Kah, L.C., Stack, K., Gupta, S., Edgar, L., Rubin, D., Lewis, K., Schieber, J., Mangold, N., & Milliken, R. (2014). A habitable fluvio-lacustrine environment at Yellowknife Bay, Gale Crater, Mars. *Science, 343*(6169).

Hadas, O., Altabet, M. A., & Agnihotri, R. (2009). Seasonally varying nitrogen isotope biogeochemistry of particulate organic matter (POM) in Lake Kinneret, Israel. *Limnology and Oceanography, 54*(1), 75-85.

Horton, T. W., Defliese, W. F., Tripati, A. K., & Oze, C. (2016). Evaporation-induced ^{18}O and ^{13}C enrichment in lake systems: a global perspective on hydrologic balance effects. *Quaternary Science Reviews, 131*, 365-379.

Jellison, R., Miller, L. G., Melack, J. M., & Dana, G. L. (1993). Meromixis in hypersaline Mono Lake, California. II: Nitrogen fluxes. *Limnology and Oceanography, 38*(5), 1020-1039.

Kempe, S., & Kazmierczak, J. (2002). Biogenesis and early life on Earth and Europa: favored by an alkaline ocean? *Astrobiology, 2*(2), 123-130.

Kenkmann, T. and Schönian, F.(2006). Ries and Chicxulub: impact craters on Earth provide insights for Martian ejecta blankets. *Meteoritics & Planetary Sciences, 41*(10), 1587-1603.

Kim, H. J., Ricardo, A., Illangkoon, H.I., Kim, M.J., Carrigan, M.A., Frye, F., & Benner, S.A. (2011). Synthesis of carbohydrates in mineral-guided prebiotic cycles. *Journal of the American Chemical Society, 133*(24), 9457-9468.

Li, L., Sherwood Lollar, B., Li, H., Wortmann, U. G., & Lacrampe-Couloume, G. (2012). Ammonium stability and nitrogen isotope fractionations for NH_4^+-NH_3(aq)-NH_3(gas) systems at 20-70°C and pH of 2-13: applications to habitability and nitrogen cycling in low-temperature hydrothermal systems. *Geochimica et Cosmochimica Acta, 84*, 280-296.

Lipschultz, F., Wofsy, S.C., Ward, B.B., Codispoti, L.A., Friedrich, G., & Elkins, J.W. (1990). Bacterial transformations of inorganic nitrogen in the oxygen-deficient waters of

the Eastern Tropical South Pacific Ocean. *Deep Sea Research Part A: Oceanographic Research Papers, 37*(10), 1513-1541.

McLauchlan, K. K., Williams, J. J., Craine, J. M., & Jeffers, E. S. (2013). Changes in global nitrogen cycling during the Holocene epoch. *Nature, 495*(7441), 352-355.

Menzel, P., Gaye, B., Wiesner, M.G., Prasad, S., Stebich, M., Das, B.K., Anoop, A., Riedel, N., & Basavaiah, N. (2013). Influence of bottom water anoxia on nitrogen isotopic ratios and amino acid contributions of recent sediments from small eutrophic Lonar Lake, central India. *Limnology and Oceanography, 58*(3), 1061-1074.

Morales, L. V., Granger, J., Chang, B.X., Prokopenko, M.G., Plessen, B., Gradinger, R., & Sigman, D.M. (2014). Elevated $^{15}N/^{14}N$ in particulate organic matter, zooplankton, and diatom frustule-bound nitrogen in the ice-covered water column of the Bering Sea eastern shelf. *Deep Sea Research Part II: Topical Studies in Oceanography, 109*, 100-111.

Müller, P. J., & Taub, J. (1977). CN ratios in Pacific deep-sea sediments: Effect of inorganic ammonium and organic nitrogen compounds sorbed by clays. *Geochimica et Cosmochimica Acta, 41*(6), 765-776.

Newell, D. L., Jensen, J. L., Frantz, C. M., & Vanden Berg, M. D. (2017). Great Salt Lake (Utah) microbialite $\delta^{13}C$, $\delta^{18}O$, and $\delta^{15}N$ record fluctuations in lake biogeochemistry since the Late Pleistocene. *Geochemistry, Geophysics, Geosystems, 18*(9), 3631-3645.

Osinski, G. R., Tornabene, L.L., Banerjee, N.R., Cockell, C.S., Flemming, R., Izawa, M.R., McCutcheon, J., Parnell, J., Preston, L.J., Pickersgill, A.E., & Pontefract, A. (2013). Impact-generated hydrothermal systems on Earth and Mars. *Icarus, 224*, 347-363.

Pohl, J., Stoeffler, D., Gall, H. V., & Ernstson, K. (1977). In *Impact and explosion cratering: Planetary and terrestrial implications* (pp. 343-404). Pergamon Press.

Robinson, R. S., Kienast, M., Luiza Albuquerque, A., Altabet, M., Contreras, S., De Pol Holz, R., Dubois, N., Francois, R., Galbraith, E., Hsu, T.C., & Ivanochko, T. (2012). A review of nitrogen isotopic alteration in marine sediments. *Paleoceanography, 27*(4).

Rothe, P., & Hoefs, J. (1977). Isotopen-geochemische Untersuchungen an Karbonaten der Ries-See-Sedimente der Forschungbohrung Nördlingen 1973. *Geologica Bavarica, 75*, 59-66.

Ruff, S. W. (2004). Spectral evidence for zeolite in the dust on Mars. *Icarus, 168*, 131-143.

Sautter, V., Sautter, V., Toplis, M.J., Wiens, R.C., Cousin, A., Fabre, C., Gasnault, O., Maurice, S., Forni, O., Lasue, J., Ollila, A., & Bridges, J.C. (2015). In situ evidence for continental crust on early Mars. *Nature Geoscience, 8*(7), 605-609.

Schauderna, H. (1983). Die Diatomeenflora aus den miozänen Seeablagerungen im Nördlinger Ries. *Palaeontographica, 188*, 83-193.

Steele, A., Benning, L.G., Wirth, R., Siljeström, S., Fries, M.D., Hauri, E., Conrad, P.G., Rogers, K., Eigenbrode, J., Schreiber, A., & Needham, A. (2018). Organic synthesis on Mars by electrochemical reduction of CO_2. *Science Advances, 4*(6). eaat5118.

Stüeken, E. E., Buick, R., & Schauer, A. J. (2015). Nitrogen isotope evidence for alkaline lakes on late Archean continents. *Earth and Planetary Science Letters, 411*, 1-10.

Stüeken, E. E., Kipp, M. A., Koehler, M. C., & Buick, R. (2016). The evolution of Earth's biogeochemical nitrogen cycle. *Earth Science Reviews, 160*, 220-239.

Stüeken, E. E., Zaloumis, J., Meixnerová, J., & Buick, R. (2017). Differential metamorphic effects on nitrogen isotopes in kerogen extracts and bulk rocks. *Geochimica et Cosmochimica Acta, 217*, 80-94.

Sturm, S., Wulf, G., Jung, D., & Kenkmann, T. (2013). The Ries impact, a double-layer rampart crater on Earth. *Geology, 41*(5), 531-534.

Talbot, M. R., & Johannessen, T. (1992). A high-resolution palaeoclimatic record for the last 27,500 years in tropical west Africa from the carbon and nitrogen isotopic composition of lacustrine organic matter. *Earth and Planetary Science Letters, 110*(1-4), 23-37.

Tesdal, J. E., Galbraith, E. D., & Kienast, M. (2013). Nitrogen isotopes in bulk marine sediment: linking seafloor observations with subseafloor records. *Biogeosciences, 10*(1), 101-118.

Vennemann, T. W., Morlok, A., von Engelhardt, W., & Kyser, K. (2001). Stable isotope composition of impact glasses from the Nördlinger Ries impact crater, Germany. *Geochimica et Cosmochimica Acta, 65*(8), 1325-1336.

Wolf, M. (1977). Kohlenpetrographische Untersuchungen der See-Sedimente der Forschungsbohrung Nördlingen 1973 und Vergleich mit anderen Untersuchungsergebnissen aus dem Ries. *Geologica Bavarica, 75*, 127-138.

Wordsworth, R., Kalugina, Y., Lokshtanov, S., Vigasin, A., Ehlmann, B., Head, J., Sanders, C., & Wang, H. (2017). Transient reducing greenhouse warming on early Mars. *Geophysical Research Letters, 44*(2), 665-671.

Zavarzin, G. A. (1993). Epicontinental soda lakes as probable relict biotopes of terrestrial biota formation. *Microbiology, 62*(4), 473-479.

Chapter 3

Elevated $\delta^{15}N$ linked to inhibited nitrification coupled to ammonia volatilization in sediments of shallow alkaline-hypersaline lakes

Abstract

Alkaline lakes are among the most bioproductive aquatic ecosystems on Earth. The factors that ultimately limit productivity in these systems can vary, but nitrogen cycling in particular has been shown to be adversely affected by high salinity, evidently due to the inhibition of nitrifying bacteria (i.e., those that convert ammonic species to nitrogen oxides). The coastal plain of Coorong National Park in South Australia, which host several alkaline lakes along 130km of coastline, provides an ideal natural laboratory for examining how fine-scale differences in the geochemistry of such environments can lead to broad variations in nitrogen cycling through time, as manifest in sedimentary $\delta^{15}N$. Moreover, the lakes provide a gradient of aqueous conditions along which the effects that pH, salinity, and carbonate chemistry have on the sedimentary record can be assessed. We report a wide range of $\delta^{15}N$ values (3.8–18.6‰) measured in the sediments (0–35 cm depth) of five lakes of the Coorong region. Additional data include major element abundances, carbonate $\delta^{13}C$ and $\delta^{18}O$ values, and the results of principal component analyses. Stable nitrogen isotopes and Na wt% display positive correlation ($R^2 = 0.59$, $p < 0.001$) across all lake systems. Principal component analyses further support the notion that salinity impacts nitrogen cycling. We propose that the inhibition of nitrification at elevated salinity may lead to the accumulation of ammonic species, which, when exposed to the water column, are prone to

ammonia volatilization facilitated by elevated pH. This process is accompanied by a significant isotope fractionation effect, isotopically enriching the nitrogen that remains in the lake water. This nitrogen is eventually buried in the sediments, preserving a record of these combined processes. Analogous enrichments in the rock record may provide important constraints on past chemical conditions and their associated microbial ecologies. Specifically, ancient terrestrial aquatic systems with high $\delta^{15}N$ values attributed to denitrification and thus oxygen deficiency may warrant re-evaluation within this framework. Constraints on pH as provided by elevated $\delta^{15}N$ via ammonia volatilization may also inform critical aspects of restricted paleoenvironments and their suitability for a *de novo* origin of life.

Introduction

Closed-basin lacustrine environments provide a means of exploring the influence of differing water chemistries and a variety of physicochemical stressors (e.g., evapo-concentration) on surface biogeochemistry that are not encountered in the modern ocean. These settings can therefore serve as natural testbeds for calibrating biogeochemical proxies under a wider range of conditions, which were perhaps prevalent on the early Earth and/or on early Mars (Cohen, 2003). These endorheic settings are also of astrobiological interest due to their capacity for wet-dry cycles—thought by some to be a critical circumstance for the *de novo* emergence of life (Campbell et al., 2019; Damer & Deamer, 2020; Lahav et al., 1978)—and they may inform the mineralogical products of desiccation

events similar to those that occurred on Mars ~3-4 billion years ago (Fairén et al., 2023; Rapin et al., 2019; Stein et al., 2018). Alkaline lakes in particular have received heightened attention in recent years due to, among their many attributes (Chase et al., 2021; Raudsepp et al., 2023; Tutolo & Tosca, 2023), a propensity to accumulate vital ingredients for leading origin-of-life hypotheses (Toner & Catling, 2019, 2020), their unusually high primary productivity compared to other ecosystems (e.g., Jones et al., 1998), and their capacities to show extreme stable isotope enrichments (Stüeken et al., 2015; Stüeken, Tino et al., 2020; Tino et al., 2023). The latter may be a way to identify these systems in the rock record.

The elevation of (1) dissolved inorganic carbon, (2) salinity, and (3) pH—at least under the Earth's current atmospheric pCO_2 (Hurowitz et al., 2023)—are primary attributes that distinguish alkaline lakes from ordinary freshwater systems. Previous studies of nitrogen availability alkaline lakes have primarily focused on the effects of high pH on nitrogen chemistry. At pH 9.25, ammonia [NH_3] and ammonium [NH_4^+] are present in equal parts in solution (pK_a = 9.25, at standard conditions). As pH approaches and/or exceeds this value, a greater proportion of NH_3 volatilizes out of solution. This relationship favors volatilization of ^{14}N, imparting $\delta^{15}N$ fractionations of > 40‰ on the escaping NH_3 and leaving the residual NH_4^+ isotopically heavy (Li et al., 2012). While this fractionation decreases in magnitude with increases in temperature, it is still as high as ~33‰ at 70°C (Li et al., 2012). Values of $\delta^{15}N \geq$ ~10‰ in sediments from evaporitic lakes have therefore been used as indicators of elevated pH during the time of deposition (Collister & Hayes, 1991; Talbot & Johannessen, 1992; Menzel et al., 2013; Stüeken et al., 2015; Stüeken, Tino et al., 2020). Yet not all high-pH settings consistently exhibit this phenomenon (e.g.,

Muzuka et al., 2004; Xu et al., 2006), and the potentially overlapping effects of denitrification, which is redox-dependent (Hecky et al., 1996) but not directly pH-dependent, must always be considered. Therefore, an interplay of the multiple parameters associated with alkaline lakes, including but not exclusively pH, appears to be responsible for enabling elevated $\delta^{15}N$ in the rock record (Xia et al., 2022). Developing a more thorough understanding of these complexities is important for accurate applications of the $\delta^{15}N$ proxy to ancient sedimentary strata.

Here we leverage the Coorong region of South Australia as a natural laboratory to interrogate the effects of alkalinity and evaporation (i.e., hypersalinity) with respect to not only the generation of high $\delta^{15}N$ signals but also their long-term preservation. Key topics include (1) the balance of abiotic and biological controls on nitrogen speciation and potentially ammonia volatilization, (2) which stable isotopic systems can best inform aqueous restriction, and how varying degrees of restriction may alter the effectiveness of these proxies, and (3) whether principle component analyses can elucidate otherwise cryptic aspects of the N-cycling and proxy preservation in alkaline-hypersaline settings when multiple data are available. Our evaluations of restriction are targeted at determining sites and/or intervals of closed-basin behavior, in which evaporation is the dominant form of water removal (i.e., significantly exceeding groundwater seepage and within an environment lacking an evident outlet [endorheic]). This evaluation will be done primarily through examinations of multiple conventional stable isotope systems ($\delta^{13}C_{carb}$, and $\delta^{18}O_{carb}$), bulk sedimentary chemical abundances (total organic and inorganic carbon [TOC and TIC] and salinity-associated elements [Na, Sr, and K, among others]). Collectively,

these data provide context for interpreting the organic $\delta^{13}C_{org}$ and bulk $\delta^{15}N$ record (here measured on decarbonated sediments to concentrated the N content of organic matter and potential clays). Importantly, among our primary goals is an improved understanding of where and when elevated $\delta^{15}N$ signals best survive early diagenesis.

Site Description

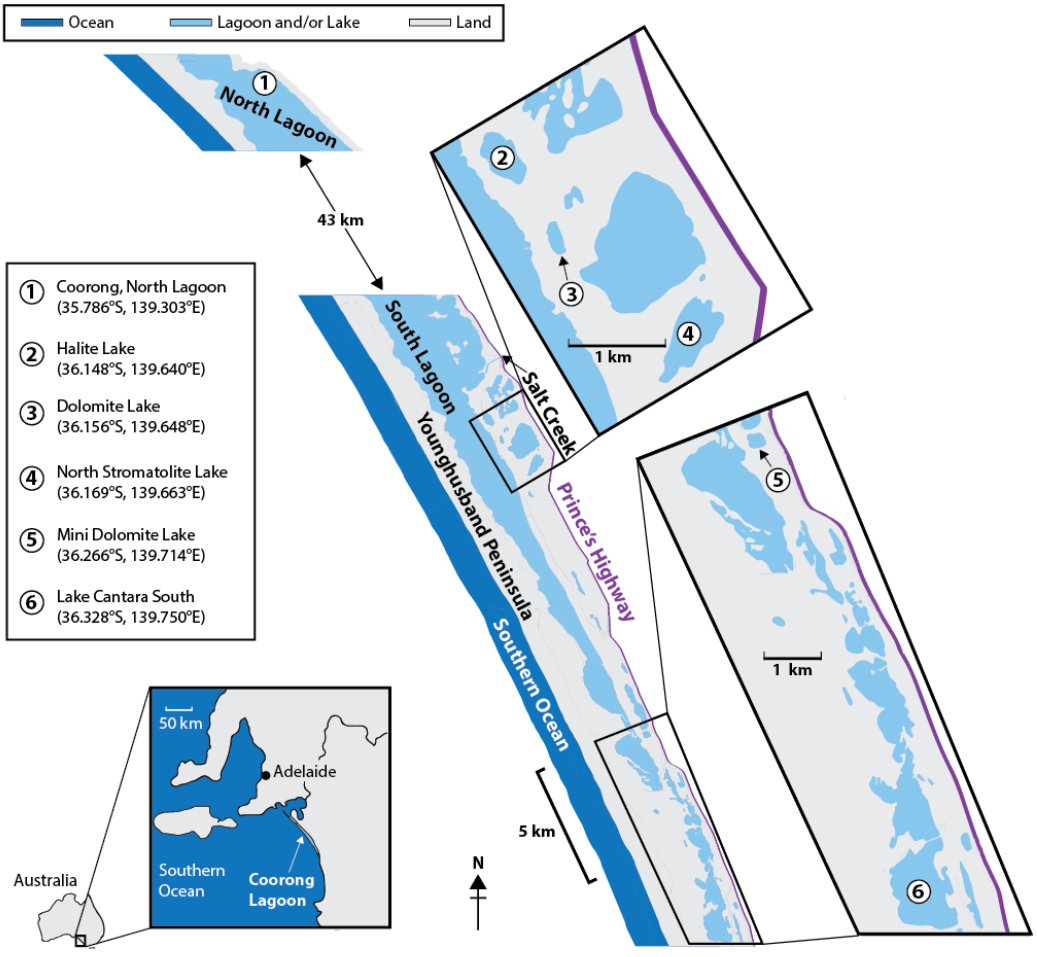

Figure 3.1 Geographical context for the studied portion of the Coorong region, including the locations of all field sites in this study. Adapted from Wright (1999).

The Coorong region in South Australia (**Fig. 3.1**) hosts several ephemeral lakes that span both an existing and historic pH gradient (von der Borch, 1965; De Deckker & Geddes, 1980; Wright, 1999; Wright & Wacey, 2005). Consequently, this area is well suited for determining which aspects of nitrogen cycling are most affected by pH and evapo-concentration and, in turn, for establishing links to persistent and preservable $\delta^{15}N$ enrichments if present. The Coorong is broadly defined by a shallow lagoon system that is separated from the Southern Ocean by the Younghusband Peninsula. It runs shore-parallel to the South Australian coastline for over 130 km (Webster, 2010). As a 'choked' lagoon, its narrow entryway effectively mutes the impact of tidal oscillations on water level fluctuation (Kjerfve, 1994). Over the past ~90 years, salinity has risen substantially, reaching over 15% (or >150 practical salinity units [PSU]) during the early austral autumn in the South Lagoon (Webster, 2010). The changing conditions are tied in part to the construction of dams in the 1930s, emplaced to prevent ocean waters from mixing with the nearby Lake Alexandrina (Wright & Wacey, 2005). These dams have exacerbated the effect of seawater input being less than the evaporation rate, particularly in the more-restricted, southern portion of the lagoon (Webster, 2010).

Several ephemeral lakes of varying biogeochemical compositions exist within ~ 2 km of the permanent lagoon itself (**Fig. 3.1**). Most of these lakes occupy interdunal furrows within a series of Pleistocene beach-dune ridges that formed during interglacial high stands over the last several hundred thousand years (Warren, 1988). Historically, these systems have been the subject of studies detailing the active, primary formation of dolomite [$CaMg(CO_3)_2$] (Mawson, 1929; Rosen et al., 1988; Warren, 1988, 1990; Wright, 1999),

which is rare on the modern Earth but forms in abundance in the Coorong lakes and is frequently present in the sedimentary rock record (Land, 1985). These lakes also contain Mg-carbonates (e.g., magnesite and hydromagnesite), a topic of interest in Mars research due to the apparent presence of these minerals at the Martian surface (Ehlmann et al., 2008), including Jezero crater (Horgan et al., 2020; Zastrow & Glotch, 2021). The ephemeral lake waters are fed by a combination of meteoric input (i.e., groundwater seepage and precipitation) and seawater intrusions (Rosen et al., 1988, 1989; Shao et al., 2018). Thus, diverse lake chemistries occur as a result of variations in both freshwater-seawater mixing and evaporation rates (Shao et al., 2018; Warren, 1990). It is this geochemical variation that we aim to leverage as a testbed for nitrogen cycling dynamics under extreme conditions.

In previous literature, the sedimentary package (~5-10 meters depth) below the lakes was subdivided into four units (Warren, 1988). The bottom two units (termed *basal* and *organic-rich*) vary in composition laterally as a function of a specific area's connectedness to the open ocean during the Pleistocene (Warren, 1988, 1990). Based relatively high siliciclastic contents (and thus lower carbonate contents), these units may not consistently reflect high pH and hypersaline conditions and are therefore not the subject of this study. The the *basal* and *organic-rich* units are overlain by so-called *Pelletal Laminated* unit, recording a time when the lakes were perennially subaqueous (Warren, 1988, 1990). The focus of our study is on the topmost or so-called *Massive* unit, which sits directly below modern surface waters. It is typically 40-60 cm thick and contains most of the Holocene dolomite in the region (Rosen et al., 1988; von der Borch, 1976)(Rosen et al., 1988; von

der Borch, 1976). The *Massive* unit is comprised of calcareous mudstones, wackestones, and pelletal packstones in a manner that is related to the energy of the overlying waters, with mudstones depositing in the deepest, lowest energy settings and packstones characterizing the higher energy margins (with wackestones in between) (Warren, 1988).

The three northernmost lakes in this study (Halite, Dolomite, and North Stromatolite) are part of the Salt Creek lake chain (**Fig. 3.1**). This area marks the Coorong's transition from a continuous body of water into a series of ephemeral lakes. The chain developed from a permanent, narrow estuarine lagoon that branched off of the greater lagoon, possibly as recently as the early Holocene, before sandy ridge development isolated the area (Warren, 1990). Moving southward, the permanent lagoon ends and becomes a series of ephemeral systems. Mini Dolomite Lake (also referred to as South South (sic) Stromatolite Lake in some previous literature) lies a few kilometers north of where that transition occurs. All four of the above-mentioned lakes sit atop calcrete-floor depressions within the same ~120 kya interdunal corridor (classified by Warren, 1990, as "Type 2a"). The fifth lake in this study, Cantara South Lake, resides even further southward and formed during a more recent breakup of the current lagoon system (classified as "Type 2b" in Warren, 1990). Previous studies have indicated that the *Massive* unit of each lake in this study area differs from the others in terms of their carbonate mineral assemblages (e.g., Warren, 1990; Raudsepp et al., 2022). This variation informed our sampling strategy because we aimed for geochemical diversity in our examination of the differing controls on nitrogen cycling.

Methods

Sample collection

Sediment cores were collected over two days in July 2018 (July 7 and 8, during the early austral winter), during a period of significant rainfall. As discussed below, this may impact the quality of the top-most sediment layer in each core. Five lakes were chosen with the intent of capturing a heterogeneous distribution of near-shore lake chemistry. The locations are, from north to south (**Fig. 3.1**): Halite Lake (36.148°S, 139.640°E), Dolomite Lake (36.156°S, 139.648°E), North Stromatolite Lake (36.169°S, 139.663°E), Mini Dolomite Lake (36.266°S, 139.714°E), and Lake Cantara South (36.328°S, 139.750°E). An additional core was taken from the North Lagoon (36.169°S, 139.663°E), providing a check to test whether our sampling and geochemical analyses produced results in line with previous studies and/or expected values. The pH of the surface waters in each sampling location was measured with a YSI professional Plus pH-ORP dual-sensor, although we note that the heavy rain at that time may compromise the utility of these data. Push cores were composed of clear, rigid polycarbonate tubing (2.75" outer diameter, 2.50" inner diameter). Each core was sliced into 2 cm sample increments. These were homogenized, transferred to 50 mL conical Falcon™ tubes, and frozen. Samples were freeze-dried, ground into dry powders with an agate mortar and pestle, and stored in scintillation vials prior to geochemical analyses.

Geochemical analyses

Total organic carbon [TOC] and total inorganic carbon [TIC] data were collected in the Lyons Biogeochemistry Laboratory at the University of California, Riverside [UCR]. Total Carbon [TC] was measured via combustion, and TIC was measured via acidification, both on an Eltra CS-500 carbon sulfur analyzer (with a precision better than ± 0.1 wt%; TOC and TIC values measured as < 0.1 wt% are reported as ≤ 0.1 wt%). TOC was then calculated as the difference between the measured TC and TIC.

All stable isotope ratios in this study were measured via continuous flow systems. For isotopic analyses on decarbonated samples ($\delta^{15}N$ and $\delta^{13}C_{org}$), 0.5-5 g of powder were treated with 1 N HCl at 50°C overnight and washed three times with 18 MΩ·cm^{-1} DI-H_2O (a variation of Stüeken et al., 2015). The dried residues were weighed into tin capsules and analyzed at the University of St Andrews on an EA Isolink coupled to a MAT253 isotope ratio mass spectrometer (IRMS) via a Conflo IV. This process also yielded total nitrogen (TN_{decarb} wt%) and C/N (mol/mol) of the decarbonated materials. The $\delta^{15}N$ and $\delta^{13}C_{org}$ data were calibrated with international reference materials USGS-40 and USGS-41 and displayed a precision of ± 0.47‰ or better, except in the case of the North Lagoon sample "NL-8", which yielded ± 1.15‰ for $\delta^{15}N$. Sample NS12 is not reported in this study due to near-zero TN_{decarb}. Values are reported in standard delta notation relative to Vienna Pee Dee Belemnite (V-PDB) for $\delta^{13}C_{org}$ and relative to air (AIR) for $\delta^{15}N$.

Stable isotopes of carbonates ($\delta^{18}O_{carb}$ and $\delta^{13}C_{carb}$) were analyzed at UCR by reacting with 104% phosphoric acid at 50°C in a Thermo Scientific GasBench II device, followed by CO_2 analysis with a Delta V Advantage IRMS. It is well established that this routine

acidification approach yields differing fractionation factors with respect to $\delta^{18}O_{carb}$ in calcite [$CaCO_3$] versus dolomite. Therefore, two sets of data were generated: one that assumed an exclusively dolomitic composition of carbonates and another that assumed an exclusively calcitic composition. A weighted average of the two values was taken based on Ca and Mg contents determined via ICP-MS to generate the reported data. Two calibration standards, NBS18 and NBS19, were used in the same run. The precision was 0.1‰ for $\delta^{13}C_{carb}$ and 0.2‰ for $\delta^{18}O_{carb}$ as reported relative to V-PDB and Vienna-Standard Mean Ocean Water [V-SMOW], respectively.

Bulk element abundances were measured via inductively coupled plasma mass spectrometry (ICP-MS) at University of St Andrews. Approximately 70 mg of each powdered sample were weighed into an acid-washed 15 ml centrifuge tube and mixed with 6.93ml of 10% (v/v) trace-metal grade HNO_3. The samples were left to react for 2 hours at room temperature. During that time, they were shaken manually every ca. 20 minutes. After 2 hours, the caps were loosened, and the centrifuged tubes were placed into an acid-proof oven at 70 °C for 1 hour. Next, the caps were retightened, and the samples were centrifuged at 3900 rpm for 15 minutes. From the supernatant, 50 µL were extracted with a pipette and mixed with 4.95 ml of 5% HNO_3 in a fresh centrifuge tube. Prior to analysis, 30 µL of each diluted sample were mixed with 1.47 ml of 2% HNO_3 inside an acid-washed 2 ml centrifuge tube. Analyses were carried out with an Agilent 7500 ICP-MS equipped with a Teflon spray chamber. Multi-element calibration standards were run at the start, in the middle, and at the end of the run to monitor and correct for drift. Reproducibility (relative error) for all elements was better than 12% and often better than 5%.

Principal component analyses (PCA)

Principle component analyses were executed in the programming language R using the integrated development environment RStudio. PCA is a commonly used statistical approach with applications in many disciplines, including stable isotope ecology. For fundamental information on PCA, see Meglen (1992) and Bro & Smilde (2014). In all PCAs in this study, the data are overlain by color-coded ellipses that represent the 95% confidence interval. The rationale for the variety of executed PCAs in this study is provided in this chapter's **Discussion**.

Results

All stable isotope measurements are reported in **Table 3.1**; abundances and ratios are listed in **Tables 3.2 and 3.3**. **Figure 3.2** provides correlation plots of all reported variables at sampling depths > 4 cm. Filtering data by this sample depth tends to increase Pearson correlation coefficients (r). We suspect that the uppermost 4 cm display inconsistencies caused by rainwater dilution and high microbial respiration rates (see **Discussion** of this chapter). For the rest of the study, we therefore focus on sediments at > 4 cm depth, as long-term preservation of biogeochemical signals is the focus of this study.

Table 3.1 Stable isotope ratio values ($\delta^{15}N$, $\delta^{13}C_{org}$, $\delta^{13}C_{carb}$, and $\delta^{18}O_{carb}$) from all sample sites. Reproducibilities (1SD) are: ± 0.5‰ or better for $\delta^{15}N$ and $\delta^{13}C_{org}$, except for sample "NL-8" which showed ± 1.2‰; ± 0.1‰ or better for $\delta^{13}C_{carb}$ and ± 0.2‰ or better for $\delta^{18}O_{carb}$.

Identifier	**$\delta^{15}N$ (‰)**	**$\delta^{13}C_{org}$ (‰)**	**$\delta^{13}C_{carb}$ (‰)**	**$\delta^{18}O_{carb}$ (‰)**	**Depth (cm)**
Cantara South Lake:					
CS1	6.9	-16.4	-0.3	33.6	0 – 2
CS2	7.2	-17.7	0.5	34.5	2 – 4
CS3	7.5	-18.3	0.7	34.9	4 – 6
CS4	8.0	-18.9	0.7	35.4	6 – 8
CS5	8.1	-19.1	0.7	35.3	8 – 10
CS6	10.1	-19.5	0.0	35.8	10 – 12
CS7	9.2	-19.1	0.1	35.6	12 – 14
CS8	9.2	-18.7	0.0	35.1	14 – 16
CS9	9.6	-18.4	0.2	35.2	16 – 18
CS10	9.0	-17.6	0.0	35.3	18 – 20
CS11	8.0	-17.4	0.2	34.8	20 – 22
CS12	5.9	-16.7	0.4	35.3	22 – 24
CS13	7.3	-17.5	0.3	34.9	24 – 26
Dolomite Lake:					
DL1	7.9	-22.6	-2.6	36.9	0 – 2
DL2	8.7	-22.8	-2.9	37.3	2 – 4
DL3	9.4	-22.5	-3.2	36.3	4 – 6
DL4	8.7	-21.8	-2.9	36.0	6 – 8
DL5	8.6	-21.6	-2.1	36.0	8 – 10

DL6	9.1	-20.8	-1.7	35.9	10 – 12
DL7	8.7	-20.7	-1.5	35.9	12 – 14
DL8	8.3	-20.9	-1.2	36.4	14 – 16
DL9	8.9	-20.7	-1.2	35.8	16 – 18
DL10	6.7	-21.0	-0.8	36.0	18 – 20
DL11	8.4	-21.0	-0.8	35.8	20 – 22
DL12	7.3	-21.3	-0.6	36.5	22 – 24
DL13	5.7	-20.5	0.7	35.6	24 – 26
DL14	4.0	-20.7	1.1	35.6	26 – 28
DL15	5.6	-21.8	0.3	35.7	28 – 30
DL16	3.8	-20.9	0.6	36.1	30 – 32
Halite Lake:					
HL1	10.7	-20.3	3.1	34.8	0 – 2
HL2	12.9	-20.9	3.6	34.7	2 – 4
HL3	12.8	-19.5	4.1	35.1	4 – 6
HL4	13.1	-19.6	5.0	35.0	6 – 8
HL5	13.2	-19.6	4.8	35.6	8 – 10
HL6	14.7	-19.6	4.5	34.6	10 – 12
HL7	17.9	-20.7	4.2	35.0	12 – 14
HL8	17.6	-20.3	4.5	34.3	14 – 16
HL9	17.8	-19.0	3.7	34.4	16 – 18
HL10	17.7	-19.4	3.4	33.8	18 – 20
HL11	17.9	-19.3	3.1	33.7	20 – 22

HL12	16.8	-20.0	2.4	33.4	22 – 24
HL13	18.3	-20.4	1.7	33.5	24 – 26
HL14	17.6	-20.3	1.5	33.2	26 – 28
HL15	18.6	-21.0	0.7	33.4	28 – 30
Mini Dolomite Lake:					
MD1	8.6	-20.7	1.3	36.1	0 – 2
MD2	9.3	-21.2	1.3	37.0	2 – 4
MD3	10.2	-21.8	1.4	36.6	4 – 6
MD4	10.6	-22.1	0.6	35.8	6 – 8
MD5	10.0	-21.1	0.2	35.3	8 – 10
MD6	10.4	-20.7	-0.1	34.6	10 – 12
MD7	10.9	-20.7	0.1	34.6	12 – 14
MD8	10.6	-20.0	0.4	34.6	14 – 16
MD9	10.4	-20.5	0.7	35.7	16 – 18
MD10	10.1	-19.7	1.2	35.5	18 – 20
North Stromatolite Lake:					
NS1	9.0	-22.4	1.4	34.7	0 – 2
NS2	9.6	-22.8	1.8	35.6	2 – 4
NS3	11.6	-24.8	1.7	35.3	4 – 6
NS4	11.9	-25.7	1.5	36.0	6 – 8
NS5	12.0	-24.4	1.3	34.8	8 – 10
NS6	12.9	-24.7	1.5	34.2	10 – 12
NS7	13.7	-23.3	1.5	34.1	12 – 14

NS8	14.0	-22.7	1.7	35.4	14 – 16
NS9	12.8	-23.4	2.0	35.0	16 – 18
NS10	13.4	-23.5	1.7	35.4	18 – 20
NS11	13.7	-22.5	2.7	35.6	20 – 22
NS13	11.7	-22.0	2.1	35.2	24 – 26
NS14	10.4	-23.3	1.3	37.0	26 – 28
NS15	9.5	-21.7	1.1	36.0	28 – 30
North Lagoon:					
NL1	7.5	-25.3	-0.3	32.2	0 – 2
NL2	6.9	-25.4	-1.0	32.5	2 – 4
NL3	7.4	-24.5	-1.0	32.7	4 – 6
NL4	6.2	-25.2	-1.0	31.7	6 – 8
NL5	6.9	-25.2	-0.5	32.0	8 – 10
NL6	8.2	-25.1	-1.1	30.6	10 – 12
NL7	7.6	-25.1	0.0	31.9	12 – 14
NL8	7.4	-25.7	0.8	31.8	14 – 16
NL9	6.5	-24.6	0.8	32.1	16 – 18

Table 3.2 Nitrogen and carbon contents (TN_{decarb}, TIC, TOC, and C/N) of all sample sites in this study. Reproducibilities (1SD) are: ± 0.06% or better for TN_{decarb}, better than ± 0.1% for both TIC and TOC. C/N (mol/mol) is derived directly from measurement of decarbonated materials combusted in an elemental analyzer prior to isotope ratio measurement; it is not the ratio of TOC to TN_{decarb}.

Identifier	**TN_{decarb} (wt%)**	**TIC (wt%)**	**TOC (wt%)**	**C/N (mol/mol)**	**Depth (cm)**
Cantara South Lake:					
CS1	1.18	6.4	7.3	24.6	0 – 2

CS2	0.14	7.7	1.1	16.4	2 – 4
CS3	0.09	8.4	0.8	16.0	4 – 6
CS4	0.05	8.9	0.3	15.0	6 – 8
CS5	0.03	9.0	0.4	15.0	8 – 10
CS6	0.18	9.3	1.0	13.6	10 – 12
CS7	0.35	9.6	0.7	14.3	12 – 14
CS8	0.33	9.5	0.9	14.9	14 – 16
CS9	0.24	9.4	0.7	16.7	16 – 18
CS10	0.32	8.9	1.1	17.4	18 – 20
CS11	0.49	9.0	1.3	19.0	20 – 22
CS12	1.10	8.5	2.8	17.2	22 – 24
CS13	0.65	8.8	1.5	18.5	24 – 26
Dolomite Lake:					
DL1	0.07	10.3	0.5	12.7	0 – 2
DL2	0.05	10.4	0.3	13.1	2 – 4
DL3	0.04	10.2	0.1	14.5	4 – 6
DL4	0.06	9.2	0.8	14.7	6 – 8
DL5	0.04	8.9	0.5	16.0	8 – 10
DL6	0.06	8.3	0.5	16.5	10 – 12
DL7	0.03	8.7	0.2	16.5	12 – 14
DL8	0.01	8.3	0.4	20.0	14 – 16
DL9	0.01	8.3	0.1	20.4	16 – 18
DL10	0.02	8.5	0.0	18.3	18 – 20

DL11	0.02	9.3	0.0	19.0	20 – 22
DL12	0.02	9.1	0.0	20.4	22 – 24
DL13	0.01	6.1	0.2	19.6	24 – 26
DL14	0.02	4.3	0.3	23.6	26 – 28
DL15	0.01	5.4	0.2	22.0	28 – 30
DL16	0.01	2.1	0.0	23.6	30 – 32
Halite Lake:					
HL1	0.15	6.5	1.5	10.3	0 – 2
HL2	0.08	6.1	0.9	12.4	2 – 4
HL3	0.28	8.6	0.8	11.1	4 – 6
HL4	0.40	8.0	0.8	11.9	6 – 8
HL5	0.64	8.0	1.0	11.2	8 – 10
HL6	0.71	7.5	1.3	11.6	10 – 12
HL7	0.24	8.0	0.9	13.4	12 – 14
HL8	0.59	8.2	1.0	13.2	14 – 16
HL9	1.67	8.5	1.2	12.9	16 – 18
HL10	0.33	8.7	1.3	13.5	18 – 20
HL11	0.48	8.7	1.1	13.2	20 – 22
HL12	0.84	8.7	0.9	15.8	22 – 24
HL13	0.56	8.2	1.5	16.9	24 – 26
HL14	0.74	7.6	2.1	18.3	26 – 28
HL15	0.71	7.8	1.1	18.8	28 – 30

Mini Dolomite Lake:

MD1	0.04	8.7	1.0	17.7	0 – 2
MD2	0.15	10.1	1.0	18.3	2 – 4
MD3	0.08	9.5	1.1	16.2	4 – 6
MD4	0.06	9.0	0.6	13.8	6 – 8
MD5	0.15	9.1	1.0	13.8	8 – 10
MD6	0.15	9.0	0.7	15.6	10 – 12
MD7	0.14	8.8	0.7	15.7	12 – 14
MD8	0.14	8.4	1.1	16.4	14 – 16
MD9	0.11	9.4	0.6	16.3	16 – 18
MD10	0.05	9.8	0.4	18.3	18 – 20

North Stromatolite Lake:

NS1	0.06	8.4	0.3	13.1	0 – 2
NS2	0.04	8.4	0.4	16.4	2 – 4
NS3	0.04	8.1	0.4	17.4	4 – 6
NS4	0.05	8.0	0.4	19.8	6 – 8
NS5	0.03	7.6	0.2	18.3	8 – 10
NS6	0.03	7.9	0.4	20.9	10 – 12
NS7	0.04	8.5	0.3	19.8	12 – 14
NS8	0.03	8.4	0.2	19.4	14 – 16
NS9	0.06	8.8	0.3	19.3	16 – 18
NS10	0.04	8.9	0.1	19.8	18 – 20
NS11	0.06	9.5	0.2	20.3	20 – 22

NS13	0.02	8.5	0.1	21.9	24 – 26
NS14	0.03	8.1	0.5	23.0	26 – 28
NS15	0.05	7.7	0.7	21.3	28 – 30
North Lagoon:					
NL1	0.16	2.4	2.1	14.0	0 – 2
NL2	0.22	3.4	2.1	12.9	2 – 4
NL3	0.03	3.4	0.7	14.0	4 – 6
NL4	0.02	3.0	0.5	15.9	6 – 8
NL5	0.01	2.3	0.4	17.5	8 – 10
NL6	0.02	2.9	0.3	16.0	10 – 12
NL7	0.01	2.4	0.2	18.0	12 – 14
NL8	0.01	1.8	0.2	16.4	14 – 16
NL9	0.01	2.2	0.1	15.8	16 – 18

Table 3.3 All reported ICP-MS major element abundances (Na, Mg, K, Ca, and Sr) in this study. Reproducibilities (1SD) are: ± 0.26% or better for Na; ± 0.86% or better for Mg; ± 0.32% or better for K; ± 1.04% or better for Ca; and ± 0.07% or better for Sr.

Identifier	**Na (wt%)**	**Mg (wt%)**	**K (wt%)**	**Ca (wt%)**	**Sr (wt%)**	**Depth (cm)**
Cantara South Lake:						
CS1	5.79	4.52	0.55	11.62	0.40	0 – 2
CS2	1.05	2.66	0.23	10.77	0.24	2 – 4
CS3	2.10	6.37	0.39	18.78	0.66	4 – 6
CS4	3.60	10.82	0.51	28.25	1.06	6 – 8
CS5	1.78	5.73	0.20	13.95	0.70	8 – 10

CS6	3.20	7.02	0.21	14.14	0.80	10 – 12
CS7	3.87	7.32	0.34	14.97	0.80	12 – 14
CS8	3.81	6.51	0.36	15.55	0.54	14 – 16
CS9	3.86	6.69	0.16	15.48	0.47	16 – 18
CS10	4.40	6.29	0.17	15.44	0.79	18 – 20
CS11	4.81	6.65	0.17	16.21	0.42	20 – 22
CS12	5.52	6.36	0.28	16.08	0.46	22 – 24
CS13	5.23	7.18	0.50	16.01	0.40	24 – 26

Dolomite Lake:

DL1	0.91	9.36	0.24	11.30	0.22	0 – 2
DL2	1.45	9.35	0.27	11.53	0.18	2 – 4
DL3	1.82	9.14	0.05	11.67	0.20	4 – 6
DL4	2.53	6.66	0.23	12.01	0.23	6 – 8
DL5	2.05	5.24	0.11	12.06	0.26	8 – 10
DL6	1.67	4.21	0.08	12.69	0.28	10 – 12
DL7	1.76	3.49	0.01	13.47	0.25	12 – 14
DL8	1.57	3.17	0.13	13.96	0.26	14 – 16
DL9	1.38	2.69	0.13	12.98	0.25	16 – 18
DL10	1.65	2.97	0.07	17.03	0.26	18 – 20
DL11	1.95	3.83	0.00	17.60	0.27	20 – 22
DL12	1.72	3.19	0.08	18.21	0.26	22 – 24
DL13	1.93	1.33	0.15	14.62	0.27	24 – 26

DL14	1.91	0.92	0.17	10.39	0.25	26 – 28
DL15	1.80	1.28	0.16	13.64	0.18	28 – 30
DL16	1.12	0.46	0.14	4.82	0.09	30 – 32
Halite Lake:						
HL1	8.99	4.83	0.26	10.26	1.32	0 – 2
HL2	4.94	6.48	0.00	7.37	0.97	2 – 4
HL3	5.09	9.77	0.00	9.96	1.49	4 – 6
HL4	6.63	11.27	0.19	7.24	1.19	6 – 8
HL5	6.84	11.95	0.12	7.98	1.22	8 – 10
HL6	9.27	11.03	0.53	9.16	1.49	10 – 12
HL7	9.56	13.56	0.65	10.89	1.53	12 – 14
HL8	8.43	12.11	0.73	10.48	1.47	14 – 16
HL9	9.57	7.96	0.97	16.79	2.14	16 – 18
HL10	7.38	3.16	0.96	16.20	1.68	18 – 20
HL11	6.83	2.28	0.84	19.50	1.75	20 – 22
HL12	7.59	2.34	0.74	15.27	1.32	22 – 24
HL13	6.33	1.83	0.66	13.62	1.10	24 – 26
HL14	6.26	2.35	0.95	15.17	1.68	26 – 28
HL15	7.27	2.24	0.81	13.49	1.65	28 – 30
Mini Dolomite Lake:						
MD1	1.07	8.52	0.24	10.96	0.64	0 – 2
MD2	1.63	11.40	0.28	11.94	0.80	2 – 4

MD3	2.09	11.36	0.42	12.62	0.76	4 – 6
MD4	2.18	9.29	0.22	12.11	0.57	6 – 8
MD5	2.66	9.32	0.23	12.69	0.45	8 – 10
MD6	2.70	7.61	0.23	11.72	0.38	10 – 12
MD7	3.78	9.55	0.52	14.72	0.49	12 – 14
MD8	3.29	7.61	0.31	13.03	0.44	14 – 16
MD9	2.60	6.85	0.28	15.10	0.56	16 – 18
MD10	2.26	4.84	0.34	17.36	0.63	18 – 20

North Stromatolite Lake:

NS1	1.55	5.76	0.16	16.25	1.79	0 – 2
NS2	3.91	7.20	0.22	23.01	2.35	2 – 4
NS3	3.66	7.67	0.24	21.06	2.25	4 – 6
NS4	3.39	6.94	0.26	20.69	2.16	6 – 8
NS5	4.22	8.83	0.13	21.68	2.25	8 – 10
NS6	2.43	7.69	0.19	7.80	0.60	10 – 12
NS7	3.99	11.28	0.16	12.49	0.92	12 – 14
NS8	3.00	5.68	0.31	9.96	0.88	14 – 16
NS9	3.98	7.66	0.28	19.02	1.69	16 – 18
NS10	1.40	5.53	0.11	13.87	1.59	18 – 20
NS11	2.34	5.94	0.23	13.78	1.59	20 – 22
NS13	1.83	3.02	0.11	9.46	1.10	24 – 26
NS14	5.00	7.12	0.20	22.45	2.70	26 – 28

NS15	2.49	4.54	0.15	13.67	1.61	28 – 30
North Lagoon:						
NL1	0.85	0.49	0.69	3.83	0.08	0 – 2
NL2	0.87	0.50	0.83	5.43	0.09	2 – 4
NL3	0.54	0.38	0.57	5.23	0.09	4 – 6
NL4	0.43	0.34	0.60	4.61	0.07	6 – 8
NL5	0.30	0.28	0.80	3.70	0.05	8 – 10
NL6	0.30	0.24	0.11	5.13	0.05	10 – 12
NL7	0.24	0.14	0.09	4.41	0.04	12 – 14
NL8	0.28	0.17	0.13	3.57	0.03	14 – 16
NL9	0.33	0.18	0.08	5.36	0.05	16 – 18

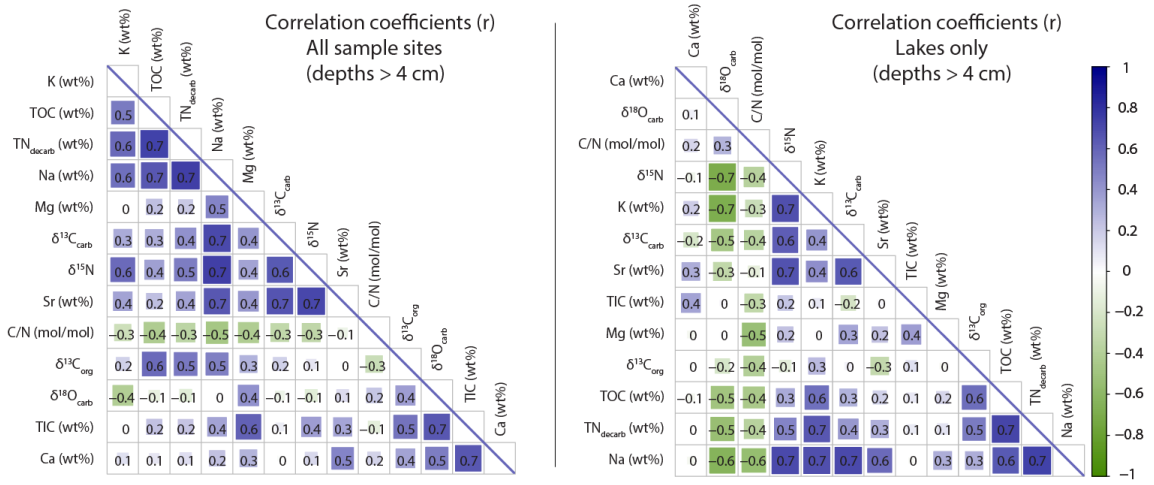

Figure 3.2 Correlation plots for the 13 different geochemical parameters measured in this study. Only sample depths > 4 cm are included in this plot; this filter tends to increase Pearson correlation coefficients (r) because it may serve to eliminate inconsistencies caused by high microbial respiration rates and/or rainwater dilution near to the surface.

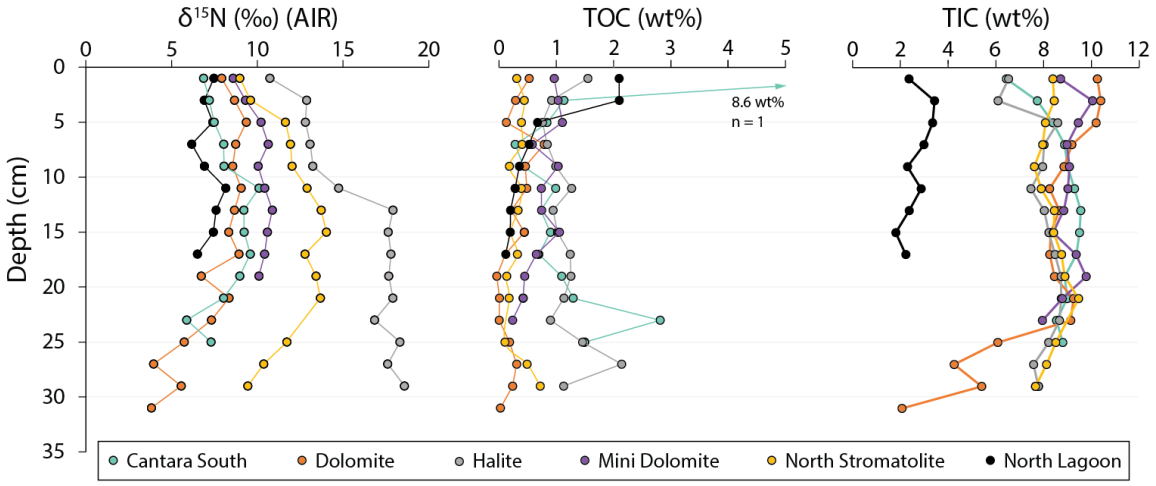

Figure 3.3 Geochemical trends ($\delta^{15}N$, TOC, and TIC) with depth at all study sites. Individual sites are distinguished by color-coding. There is high intersystem variability in $\delta^{15}N$. The North Lagoon site (black) functions as an endmember because it not a lake and is fed directly by the open ocean.

Stable nitrogen and carbon isotopes of decarbonated sediments

Across all sites, $\delta^{15}N$ ranges from 3.8‰ to 18.6‰ **(Fig. 3.3),** while $\delta^{13}C_{org}$ spans -25.7‰ to -16.4‰. The $\delta^{15}N$ data exhibit at a narrower range in the top 4 cm of sediment, potentially due to isotopic dilution via meteoric nitrate introduced by heavy rainfall during the sampling period. At North Lagoon (mean $\delta^{15}N = 7.2‰$, $n = 9$, $\sigma = 0.6‰$), which serves as an end member because it is fed directly by the open ocean with only minor freshwater input, values span from 6.2‰ to 8.2‰. This is a slight enrichment from the average modern marine nitrate (NO_3^-) value of ~5‰ but lower than values reported from marine upwelling zones (9-12‰) (Tesdal et al., 2013). Carbon isotopes of the decarbonated materials ($\delta^{13}C_{org}$) at North Lagoon are invariant (mean = -25.1‰, n = 9, σ = 0.4‰) and the lowest of all sample sites.

Halite Lake (mean $\delta^{15}N = 15.8‰$, $n = 15$, $\sigma = 2.5‰$) exhibits the highest $\delta^{15}N$; values broadly increase with depth before reaching a maximum of 18.6‰ at the base of the core

(28-30cm). Carbon isotope values at Halite are, on average, the second highest of any site (mean $\delta^{13}C_{org}$ = -20.0‰, n = 15, σ = 0.6‰). North Stromatolite is the only other system to consistently display $\delta^{15}N$ > 11‰ (mean = 11.9‰, n = 15, σ = 1.6‰), with an apparent trend that starts at 9.0‰ and increases with depth until reaching 14.0‰ at 14-16cm before descending back to 9.5‰ at the bottom of the core. The $\delta^{13}C_{org}$ data there (mean = -23.4‰, n = 15, σ = 1.1‰) are the lowest of any sampled lake, with a minimum of -25.7‰ at 6-8cm before consistent increases lead to a maximum of -21.7‰ at the bottom of the core. Dolomite Lake (mean $\delta^{15}N$ = 7.5‰, n = 16, σ = 1.7‰) shows $\delta^{15}N$ that increases from 7.9‰ at the surface to a maximum of 9.4‰ at 4-6 cm depth. Values persist in the range of 6.7‰ to 9.1‰ before decreasing to 5.7‰ at 24-26 cm and eventually reach a minimum of 3.8‰ at 30-32 cm. The $\delta^{13}C_{org}$ values at Dolomite (mean = -21.4‰, n = 16, σ = 0.7‰) range between -22.8‰ to -20.5‰, in line with the average value of all lake samples (mean = -20.8‰, n = 68, σ = 1.9‰). At Cantara South (mean $\delta^{15}N$ = 8.2‰, n = 13, σ = 1.2‰), $\delta^{15}N$ increases from 6.9‰ at the surface to a maximum of 10.1‰ at 10-12cm depth; values are ≥ 9‰ until 20cm and then fall to a minimum of 5.9‰ at 22-24cm. The $\delta^{13}C_{org}$ data at Cantara South are the lowest at any site (mean = -18.1‰, n = 13, σ = 0.9‰). Mini Dolomite Lake (mean $\delta^{15}N$ = 10.1‰, n = 10, σ = 0.7‰) has $\delta^{15}N$ = 8.6‰ at the surface followed by data that are clustered between 10.0‰ and 10.9‰ for the remainder of the core. The carbon isotopes there fit within a small range between -19.7‰ and -22.1‰ (mean $\delta^{13}C_{org}$ = -21.4‰, n = 10, σ = 0.7‰).

Total organic and inorganic carbon, total nitrogen, C/N ratios

Total organic carbon is either uniformly below 2 wt% or tends to exceed that value only near the sediment-water interface. The North Lagoon contains 2.1 wt% TOC from 0-4 cm followed by an abrupt decrease to 0.7 wt% at 4-6 cm and eventually a minimum of 0.1 wt% at the bottom of the core. Cantara South possesses the highest TOC, both at the surface (7.3 wt% at 0-2 cm depth) and overall (mean = 1.5 wt%, n = 13, σ = 1.8%). Halite Lake has the second highest average TOC (mean = 1.2 wt%, n = 15, σ = 0.3%) and is notable for its relatively consistent values that range 0.8 wt% to 2.1 wt%. Dolomite and North Stromatolite have uniformly low TOC contents (≤ 0.8 wt% in all samples), while Mini Dolomite is elevated by comparison (mean = 0.8 wt%, n = 10, σ = 0.2%).

These historically carbonate-bearing sediments have TIC values that are elevated compared to most terrestrial or marine settings. Average TIC contents, from highest to lowest, are: Mini Dolomite (mean = 9.2 wt%, n = 10, σ = 0.5%), Cantara South (mean = 8.7 wt%, n = 13, σ = 0.8%), North Stromatolite (mean = 8.3 wt%, n = 15, σ = 0.5%), Dolomite (mean = 7.9 wt%, n = 15, σ = 2.2%), and Halite (mean = 7.9 wt%, n = 15, σ = 0.8%). For reference, TIC in pure calcite and dolomite are 12.0% and 13.0%, respectively. Dolomite Lake displays a decrease from 9.1 wt% to 2.1 wt% over the final 10cm core. This decrease coincides with a 3.5‰ decrease in $\delta^{15}N$. The North Lagoon contains significantly less TIC compared to the other studied lakes (mean = 2.6 wt%, n = 9, σ = 0.5%).

The total nitrogen content (TN_{decarb}) correlates with TOC (R^2 = 0.42, n = 77, $p < 0.001$) across all samples, indicating that most of the nitrogen is preserved within organic matter. Halite Lake displays the highest average TN_{decarb} value (mean = 0.56 wt%, n = 15,

σ = 0.37 wt%), including a maximum of 1.67 wt%. Cantara South (TN_{decarb} mean = 0.40 wt%, n = 13, σ = 0.36 wt%) exhibits elevated TN_{decarb} contents (1.18 wt%) at the surface before decreasing to a minimum of 0.03 wt% at 8-10cm depth. TN_{decarb} is uniformly low (≤ 0.22 wt%) at the Dolomite, Mini Dolomite, North Stromatolite, and North Lagoon sites. The following are the average C/N ratios (mol/mol, where C is short for TOC) of those same decarbonated materials, from least to greatest: Halite (mean = 13.6, n = 15, σ = 2.5), North Lagoon (mean = 15.6, n = 9, σ = 1.6), Mini Dolomite (mean = 16.2, n = 10, σ = 1.5), Cantara South (mean = 16.8, n = 13, σ = 2.7), Dolomite (mean = 18.2, n = 16, σ = 3.4), and North Stromatolite (mean = 19.3, n = 15, σ = 2.4). Notable observations include increasing C/N with depth at the Halite, Dolomite, and North Stromatolite sampling sites.

Bulk element abundances via ICP-MS

While elevated Ca and Mg values can be expected in these known Ca- and Mg-bearing carbonate sediments, all lake sites are enriched in Na, K, and Sr (henceforth grouped as salinity-associated elements [SAE]). Generally, TN_{decarb} is correlated with Na and K to the same extent (**Fig. 3.2**), which implies that K is mostly salt-bound as opposed to clay-bound. There are significant differences in SAEs among the studied lake sites. For example, the difference between the highest average Na content at Halite (mean = 7.40 wt%, n = 15, σ = 1.45%) and the lowest at Dolomite (mean = 1.70 wt%, n = 16, σ = 0.37%) is 6.7 wt%. The other three lakes span a middle range (Mini Dolomite [mean = 2.43 wt%, n = 10, σ = 0.74%], North Stromatolite [mean = 3.08 wt%, n = 15, σ = 1.06%], Cantara South [mean = 3.77 wt%, n = 13, σ = 1.39%]). The $\delta^{15}N$ values across all sites correlate

with Na (R^2 = 0.53, $p < 0.001$) and Sr (R^2 = 0.46, $p < 0.001$), and coefficients of determination increase (R^2 = 0.59, $p < 0.001$ for Na and R^2 = 0.51, $p < 0.001$ for Sr; **Fig. 3.4**) when considering depths > 4 cm only.

Stable carbon and oxygen isotopes of carbonates

There are no extreme depletions or enrichments in $\delta^{13}C_{carb}$ (ranging -3.2‰ to 5.0‰) or $\delta^{18}O_{carb}$ (ranging 30.6‰ to 37.3‰) at any site. The North Lagoon samples approximate values expected from a marine environment ($\delta^{13}C_{carb}$ mean = -0.4‰, n = 9, σ = 0.7‰; $\delta^{18}O_{carb}$ mean = 31.9‰, n = 9, σ = 0.6‰). All lake sites show elevated values by comparison, except for $\delta^{13}C_{carb}$ at Dolomite, which is lower (mean = -1.2‰, n = 16, σ = 1.3‰). Conversely, Dolomite Lake contains the highest $\delta^{18}O_{carb}$ (mean = 36.1‰, n = 16, σ = 0.4‰), while Halite has the highest average $\delta^{13}C_{carb}$ by a margin of 1.7‰ (mean = 3.4‰, n = 15, σ = 1.3‰).

Coupled $\delta^{13}C_{carb}$ and $\delta^{18}O_{carb}$ data from carbonates (**Fig. 3.5**) show correlation in only two systems: Halite (R^2 = 0.78, $p < 0.001$) and Mini Dolomite (R^2 = 0.74, $p < 0.05$). Mini Dolomite also displays a relationship between Na and $\delta^{18}O_{carb}$ (R^2 = 0.65, $p < 0.05$). When Halite and North Lagoon samples are grouped, relationships are apparent between $\delta^{13}C_{carb}$-$\delta^{18}O_{carb}$ (R^2 = 0.85, $p < 0.001$) and Na-$\delta^{18}O_{carb}$ (R^2 = 0.69, $p < 0.001$). Across all lake systems, there is a moderate relationship between Na and $\delta^{18}O_{carb}$ (R^2 = 0.41, $p < 0.001$).

Discussion

Geochemistry of the Coorong lakes

A high degree of variation in $\delta^{15}N$ exists at the studied lakes (**Fig. 3.3**), despite their proximity to one another and several first-order geologic similarities. These systems have been alkali-saline and shallow (< 10 cm water column, excluding Cantara South) for at least several hundred years, including the interval captured by our data (i.e., the *Massive* unit of Warren [1988]; see Raudsepp et al. [2022] for radiocarbon dating of North Stromatolite Lake and other proximal systems). Thus, the differences in sedimentary chemistry observed among the studied lakes may offer direct insights into which geochemical parameters are connected to the preservation of elevated $\delta^{15}N$. When the lakes are ordered from lowest to greatest $\delta^{15}N$, they show a gentle gradient and by extension a framework for discussing $\delta^{15}N$-amplifying characteristics that are otherwise obscure. Many of the observed trends would likely be more difficult to detect with an approach that focuses on only one lake.

Linkages between nitrogen cycling and salinity

The link between $\delta^{15}N$ and SAEs (**Fig. 3.2 and 3.4**) is strong in the Coorong lake sediments, motivating our discussion of the possible effects of salinity on nitrogen cycling. Importantly, there is extensive independent empirical evidence that the stability and abundance of reduced nitrogen (e.g., NH_4^+) increase with salinity in hypersaline lakes, solar salterns, experimental cultures, estuaries, and the Coorong Lagoon itself (Isaji et al., 2019; Koops et al., 1990; Mosley et al., 2023; Post, 1977; Priestley et al., 2022; Rysgaard

et al., 1999). This accumulation of reduced N may have multiple causes. At extremely high salinities (> 100 PSU), this relationship is perhaps most parsimoniously explained by physiological salinity limits of nitrifying bacteria (i.e., those that oxidize reduced nitrogen to nitrogen oxide species [NO_x] as a means of metabolism) (Koops et al., 1990; Oren, 1999). At salinities ranging 35-100 PSU, lower rates of nitrification may be related to the well-established relationship between increased salinity and decreases in dissolved O_2 (e.g., Garrels & Christ, 1965). However, Rysgaard et al. (1999) documented in Randers Fjord estuary in Denmark that even salinity shifts in the range of 0-30 PSU may present physiological impairment of microbial nitrification within sediments. This impairment would act in concert with the observation that prevalent cations (e.g., Na^+) can replace NH_4^+ in clays and thus reduce NH_4^+ adsorption and lead to sedimentary efflux of ammonic species into the water column. The net consequence of these two effects is enhanced ammonium buildup in the water column.

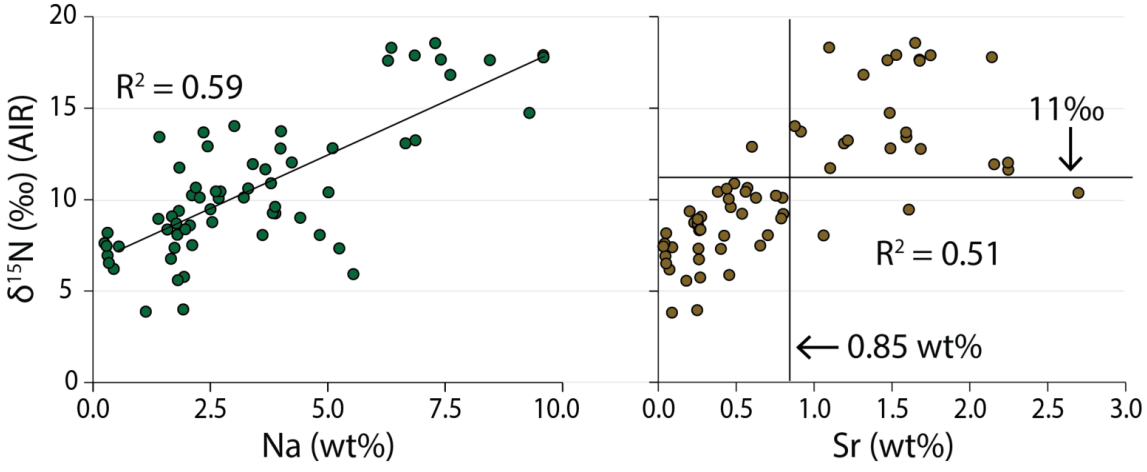

Figure 3.4 Scatterplots of $\delta^{15}N$ data vs Na and Sr, from depths > 4 cm. There is a statistically moderate relationship between both $\delta^{15}N$ vs Na (wt%) and $\delta^{15}N$ vs Sr (wt%). There is also an apparent threshold in the $\delta^{15}N$ vs Sr (wt%) data, where 96% of samples with $\delta^{15}N$ > 11‰ also have Sr > 0.85 wt%.

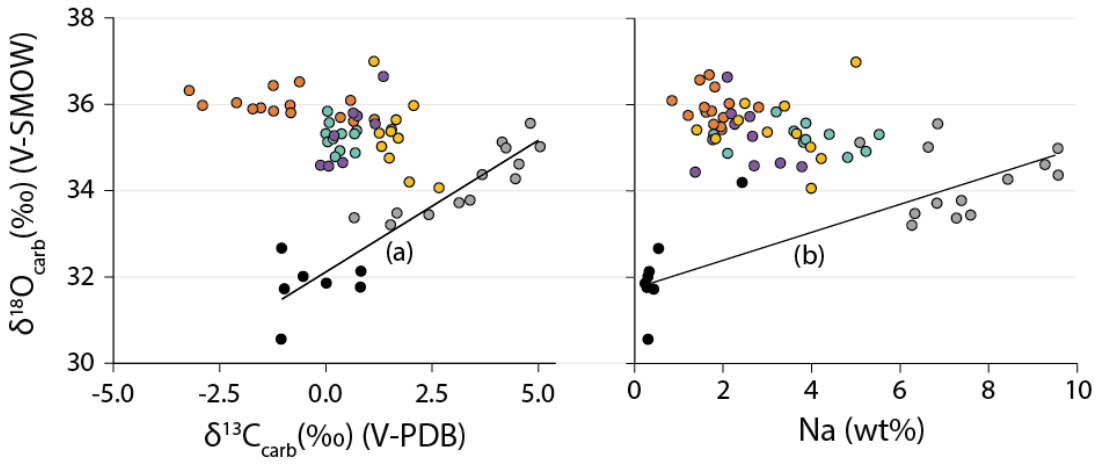

Sample Site	R^2 ($\delta^{18}O_{carb}$ vs. $\delta^{13}C_{carb}$)	R^2 ($\delta^{18}O_{carb}$ vs. Na wt%)
Cantara South	0.08	0.03
Dolomite	0.20	0.04
Halite	**0.78**	0.01
Mini Dolomite	**0.74**	**0.65**
North Stromatolite	0.01	0.02
North Lagoon	0.04	0.29
Halite + North Lagoon	**0.85 (a)**	**0.69 (b)**
All lakes (no lagoon)	0.21	**0.41**

Figure 3.5 (Top) Scatterplots of $\delta^{18}O_{carb}$ vs $\delta^{13}C_{carb}$ and $\delta^{18}O_{carb}$ vs Na wt%, from depths > 4 cm. (Bottom) Coefficients of determination for the variables of interest at each sample site, as well as across all lakes. (a) Halite lake and North Lagoon display a statistically strong relationship in $\delta^{18}O_{carb}$ vs $\delta^{13}C_{carb}$ space, indicating that Halite lake may be evolved form a seawater source. This is in agreement with previous sedimentological and mineralogical evidence (Warren, 1990).

The effects of hypersalinity on nitrifying bacteria have been experimentally quantified. Perhaps the most straightforward example is Koops et al. (1990), where three *Nitrosomonas* species (obligate NH_x oxidizers; *N. halophilus, N. mobilis*, and *N. oceanus*) were isolated from hypersaline environments. Salt (Na-Cl type) tolerances varied, but the highest tolerance was seen with *N. halophilus*, which exhibited optimum nitrification rates at 700 mM NaCl (40.9 PSU). Importantly, as 1700 mM NaCl (99 PSU) was approached,

NO_2^- production by nitrification was significantly diminished to near-zero. These observations are in strong agreement with classic observations of the complete absence of NO_x in large portions of Great Salt Lake (Utah, USA; Post, 1977) and a dearth of these species (maximum of 20 μg/L) in the Dead Sea (Jordan Rift Valley; Nissenbaum, 1975).

How hypersalinity influences $\delta^{15}N$ preservation in sediments (i.e., nitrogen bound to buried organic matter and possibly clays) is not as well studied. To interpret elevated isotope ratios found in solar salterns (Trapani, Italy), Isaji et al. (2019) presented a model of residually increased surface $\delta^{15}N$. Specifically, progressive ammonium assimilation in the subsurface may isotopically enrich surface ammonium ($\delta^{15}N \approx 34.0‰$ in the surface brine). At a certain depth, the respiration of organic matter liberates organic N (e.g., R-NH_2) as NH_4^+. A series of microbial primary producers then assimilate the ammonium in a fashion that preferentially uptakes ^{14}N over ^{15}N and leaves ^{15}N-enriched ammonium to interact with the surface environment. At that point, evapo-concentration of the hypersaline waters aids in the volatilization of NH_3.

There are at least two critical distinctions between the systems described above versus those in this study. Specifically, Coorong lake sediments have much greater carbonate contents and historically higher measured pH values, with some intervals reaching at least pH of 9.26 and theoretically up to 10.20 based on mineralogical constraints (von der Borch, 1965; Wright, 1999).

Assessing closed-basin behavior and its relationship with $\delta^{15}N$ enrichment

It is critical to evaluate for endorheic behavior at each study site, as this informs the potential for unidirectional escape of gaseous NH_3 that outbalances total N input. This scenario would allow for heavily skewed residual $\delta^{15}N$ at a given lake. The positive covariation of $\delta^{13}C_{carb}$ and $\delta^{18}O_{carb}$ is a common indicator for closed-basin lacustrine systems (Talbot, 1990). This relationship occurs because residual $\delta^{18}O_{carb}$ is driven up by evaporation of H_2O while CO_2 degasses due to corresponding increases in salinity, which generates a $\delta^{13}C_{carb}$ isotope effect resulting from the preferential loss of ^{12}C. By that measure, $\delta^{13}C_{carb}$-$\delta^{18}O_{carb}$ covariation evidence of closed-basin behavior is surprisingly infrequent across our study sites. Only Halite and Mini Dolomite lakes display the expected $\delta^{13}C_{carb}$-$\delta^{18}O_{carb}$ correlation (**Fig. 3.5**). This lack of $\delta^{13}C_{carb}$-$\delta^{18}O_{carb}$ covariation in the other lakes is surprising because they currently appear endorheic. Specifically, North Stromatolite and Dolomite are ephemeral on annual timescales (i.e., they undergo desiccation, which should increase isotopic covariation with salinity increases), and Cantara South does not show evidence an outlet (i.e., is endorheic).

Changes in water sourcing through time may explain the infrequency of $\delta^{13}C_{carb}$-$\delta^{18}O_{carb}$ correlation. The South Lagoon itself is known to receive a significant influx of brackish meteoric waters flowing towards the coast (≥ 40%; Shao et al., 2018). If this meteoric water source varies in its impact among the studied Lakes, it may have shifted $\delta^{13}C_{carb}$-$\delta^{18}O_{carb}$ relationships away from straightforward covariation in some of these settings. The sites with strong $\delta^{13}C_{carb}$-$\delta^{18}O_{carb}$ correlation (Halite and Mini Dolomite), in contrast, may be the result of relatively consistent water sources through time.

In any case, Halite has the highest observed $\delta^{15}N$ values and displays a clear history of closed-basin behavior in its $\delta^{13}C_{carb}$ and $\delta^{18}O_{carb}$ data. Importantly, Halite Lake likely evaporated from seawater and/or saline lagoon water, as opposed to freshwater (**Fig. 3.5**, relationship [**a**]). This interpretation is in agreement with previous sedimentological and mineralogical evidence (Warren, 1990) and may explain its extreme elevation in SAEs—Na and Sr in particular—presumably related to evapo-concentration. While Halite and Mini Dolomite lakes are both restricted, only Halite exhibits $\delta^{15}N > 11‰$. A direct evaluation of the two systems within the context of a statistical approach may allow us to shed additional light on these relationships.

Evaluating the value of principle component analyses at the Coorong

Principal component analysis (PCA) provides a means of visualizing and quantifying otherwise obscure but often meaningful trends within large datasets (Bro & Smilde, 2014). We have taken a multi-step approach resulting in four PCAs (**Fig. 3.6**)—where one PCA informs the next—to elucidate drivers of elevated $\delta^{15}N$ at the Coorong lakes. The first PCA (**Fig. 3.6a**) takes all sample sites into consideration, including the North Lagoon. The inclusion of the North Lagoon end member serves to verify the approach, as the PCA noticeably separates this non-lacustrine setting (bottom left of plot). The top-loading scores (i.e., the *r* value of a given variable versus its corresponding principal component value) for PC1 indicate that $\delta^{15}N$ and SAEs are the major discriminators in the dataset.

Removing the North Lagoon samples to create a lakes-only PCA (**Fig. 3.6b**) provides more insight. There is greater separation of Halite and Dolomite lakes from the other systems across PC1, establishing them as end members based primarily on differences in K, Na, $\delta^{15}N$, TN_{decarb}, and $\delta^{18}O_{carb}$. This outcome affirms that nitrogen chemistry and its response to high salinity is a strong discriminator of these systems. These results highlight that the complex nature of nitrogen cycling at these sites is deeply informed by these contextual data.

In the third PCA (**Fig. 3.6c**), $\delta^{15}N$ is removed as an input. Unlike the previous PCAs, which were visually binned by lake system, the results in this case are binned instead by whether $\delta^{15}N$ is greater than or less than 11‰. This cutoff is established by (1) a boundary observed in our Sr vs. $\delta^{15}N$ plot (**Fig. 3.4**) and (2) a threshold that is not exceeded at Mini Dolomite Lake, despite strong evidence of being consistently endorheic through time (**Fig. 3.5)**. We also note that values greater than 11‰ are extremely rare in the marine realm (e.g., Tesdal et al., 2013), further highlighting that they represent a distinct hierarchy of biogeochemical processes. By changing $\delta^{15}N$ from an input to a sampling bin, the aim is to determine which variables are most affecting nitrogen isotope fractionation. However, this PCA lacks the resolving power of the previous two (i.e., there is significant overlap between the two bins). One reason for this overlap may be the confounding nature of North Stromatolite Lake, which exceeds 11‰ at most depths but otherwise shows no clear history of being endorheic or having contributions of marine or lagoon water. Despite such ambiguities, Stromatolite Lake does share one major similarity to Halite Lake (beyond $\delta^{15}N > 11‰$): high Sr compared to all other sites in this study. Thus, the process that led

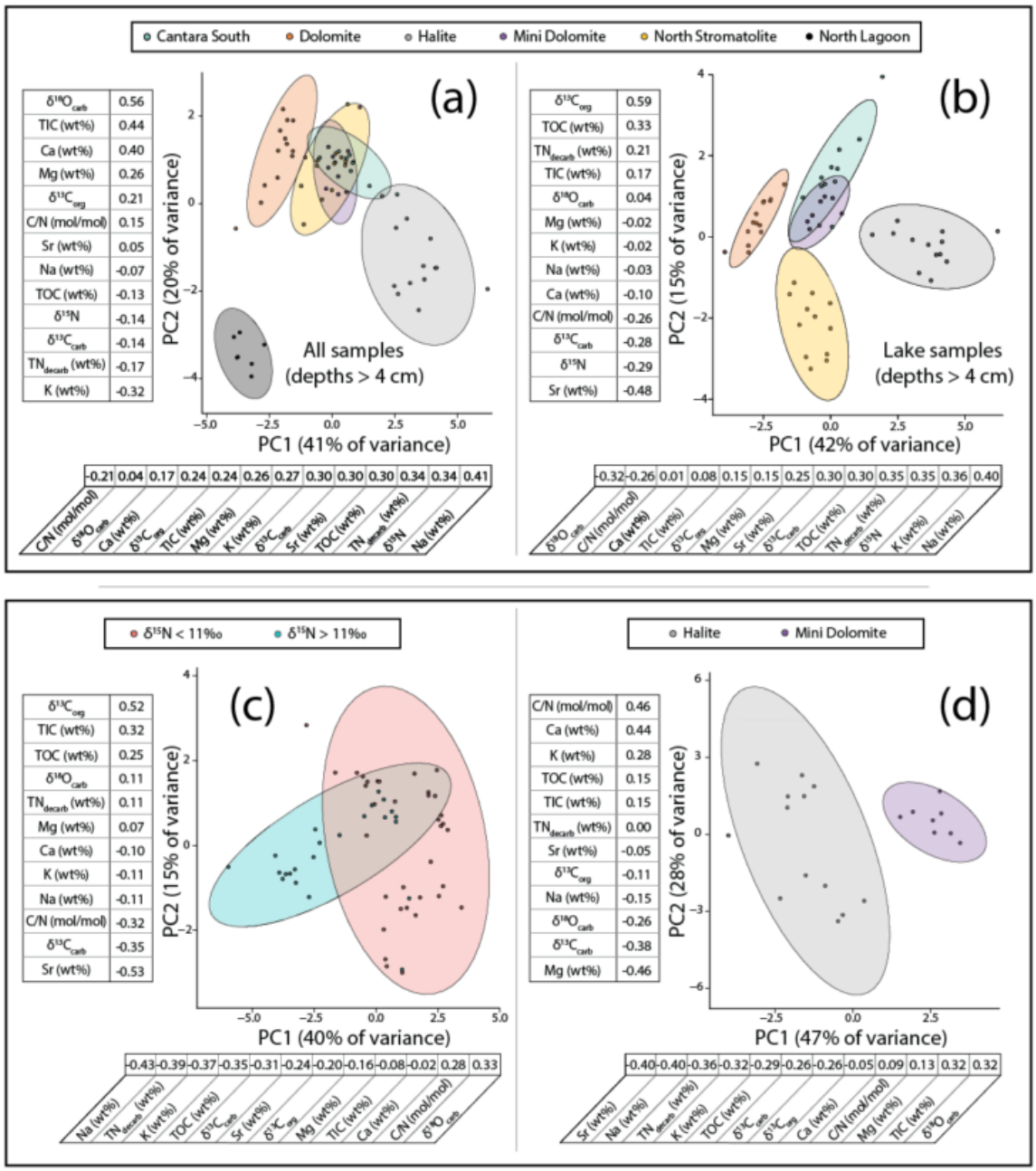

Figure 3.6 A stepwise series (a–d) of principal component analyses (PCAs). Color-coded ellipses that represent 95% confidence interval. The values placed above and below the x- and y-axes—each associated with a specific variable—are loading scores. Loading scores are equivalent to the r value of a given variable versus its corresponding principal component value; they serve as a general indicator of which variables have the strongest influence on the position of a given data point in principal component space. The rationale and significance of each PCA are described in the **Discussion** section of this chapter.

to elevated Sr contents may be related to the process that caused N isotope enrichment in these systems. The fourth PCA (**Fig. 3.6d**) confirms this conclusion. Halite and Mini

Dolomite show the greatest degree of closed-basin behavior as manifest in C and O isotope trends, yet Mini Dolomite never exceeds $\delta^{15}N > 11‰$. As such, PCA of the two systems may offer considerable insight. The results indicate that Sr is as strong a differentiator as Na and that Sr is more influential on $\delta^{15}N$ than K. Moreover, the loading score of Sr has increased in absolute value from 0.25 and 0.24 in PCAs 2 and 3, respectively, to 0.40 in PCA 4.

Altogether, the PCA results provide at least two key insights. First, nitrogen chemistry is among the strongest differentiators in these systems. This is important because it implies that elevated $\delta^{15}N$ could function as a proxy for hypersalinity, provided organic matter degradation and endorheic behavior are indicated by independent lines of evidence. Second, a dissolved Sr threshold (here inferred from Sr wt% in the solid phase) may be the most critical inhibitor of nitrification. The possible effects of Sr toxicity on nitrogen cycling(and on microbial nutrient cycling in general) have not been described previously to our knowledge, and thus our study points to a potentially fruitful new avenue of fundamental research.

A proposed mechanism for elevated $\delta^{15}N$ at Halite Lake

We propose a mechanism for $\delta^{15}N$ elevation that builds off previous literature while incorporating new insights from the Coorong lakes. Our conceptual model presented in schematic **Figure 3.7** is similar to that of Isaji et al. (2019) but differs in multiple key ways, including deep consideration of organic matter degradation and cation substitution in clays (e.g., Rysgaard et al. 1999; Wacey et al. 2007). First, photosynthesis results in biomass

Figure 3.7 A proposed schematic of hypersaline nitrogen cycling that results in elevated $\delta^{15}N$. The mechanism is described in detail in the **Discussion** section and is broadly adapted from Isaji et al. (2019), although there are several key differences. These differences include a holistic consideration of organic matter degradation, cation substitution in clays, and the recognition of a possible Sr toxicity threshold.

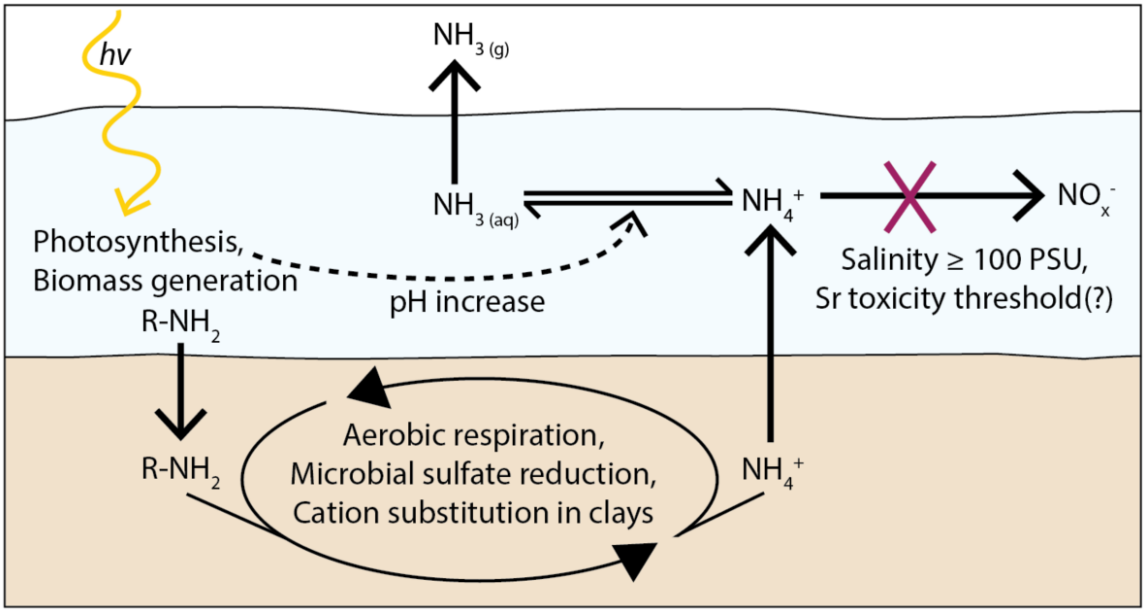

generation. The primary production in these lakes is driven by both cyanobacteria and algae. Cyanobacteria are evidenced by (1) a variety of stromatolitic features across these systems and suggestions from (2) biogenic dolomite morphologies observed under scanning electron microscopy (von der Borch, 1976; Wright, 1999). Evidence of algae includes C/N ratios measured in our study (**Table 3.2**), which in some cases align with those of algae from a regional ecology survey (C/N in the range of 10-20; Krull et al., 2009). Nitrogen is assimilated during photosynthesis and buried as biomass. Then, organic matter breakdown remineralizes assimilated N as ammonium and delivers it back to the water column (Berner, 1980; Isaji et al., 2019). In the Coorong lakes, microbial sulfate reduction (MSR) has been shown to occur within the uppermost sediment layers of these lakes (0-10 cm depth; Wacey et al., 2007), but sulfate reduction cannot easily be coupled to ammonium oxidation due to unfavorable thermodynamics. Hence, ammonium is

generated during MSR and readily supplied back to the water column. We also posit that hypersalinity exacerbates ammonium release to the water column due to salinity-associated cation substitution in clays at the sediment-water interface, as discussed above (Rysgaard et al., 1999).

Once formed, ammonium is relatively stable in the hypersaline water column (e.g., Isaji et al., 2019). Here we invoke a salinity threshold of 100 PSU, which is based on documented physiological limitations of hypersaline nitrifiers (~99 PSU; Koops et al., 1990). Given that the south lagoon itself reaches > 150 PSU (Webster, 2010), the ephemeral lakes are likely capable of exceeding this value during evapo-concentration. For example, Halite Lake salinity was observed at 162 PSU in August 2018 by Shao et al. (2021). If the water column is above 100 PSU, then the conversion of NH_4^+ to NO_x is significantly diminished. The pH of the waters then dictates the equilibrium chemistry of the reduced N-species (i.e., as pH increases, a larger proportion of ammonium is converted to ammonia). The total amount of ammonia that is volatilized is likely influenced by various additional parameters such as temperature and salinity. It is important to note that the proposed mechanism applies to shallow water environments that are not redox-stratified. Because the fractionation associated with denitrification is thought to be directly proportional to the amount of nitrate that occurs within the water column (Kessler et al., 2014; Rooze & Meile, 2016), it is unlikely to generate a significant N-isotope expression in these shallow settings, where nitrate is rare. Additionally, our model significantly hampers nitrate generation at > 100 PSU and, by extension, cuts off the oxidant supply (NO_x^-) needed for denitrification. Evaluations of deeper closed-basin systems that display

redox and/or salinity stratification would have to account for the potential effects of salinity gradients and water-column denitrification on $\delta^{15}N$.

Study site	Measured pH	Highest pH (previous studies)
Cantara South Lake	8.07	~9.7–10.2 (theoretical; von der Borch, 1965)
Dolomite Lake	8.56	9.26 (measured; Wright, 1999)
Halite Lake	7.59	7.82 (measured; Wright and Wacey, 2005)
Mini Dolomite Lake	8.32	9.11 (measured; Wright and Wacey, 2005)
North Stromatolite Lake	8.39	8.98 (measured; Raudsepp *et al.*, 2022)

Table 3.4 pH values recorded during the July 2018 sampling trip of this study, along with the highest pH values measured or calculated in previous studies.

Notably, our field measurements (**Table 3.4**) did not display pH > 8.6 at any site (i.e., below the pKa of ammonium [9.25]). Halite Lake (with the highest $\delta^{15}N$) yielded a pH value of 7.59. There are two key considerations when evaluating this apparent discrepancy between pH < 9.25 and elevated $\delta^{15}N$. First, our sediment cores likely record thousands of years of history, including 10^2–10^3 year before present at the earliest measurable horizons (0–2.5 cm depth; see radiocarbon dating from Raudsepp et al., 2022). In other words, paleo pH in these systems may have been considerably different than our modern surface measurements, which were taken during heavy rainfall. Second, the accumulation of ammonium in the water column may play a larger role for $\delta^{15}N$ elevation than does absolute pH. For example, at a pH of 8.5 and a temperature of 30°C, an equilibrated, ideal NH_4^+-NH_3 solution would be 20.3% NH_3. **Equation 3.1**, which is based on experimental results from a previous study (Li et al., 2012), indicates that the fractionation under those conditions would be $1000\ln\alpha = \sim 43.3$.

$$1000\ln\alpha_{NH_4^+\text{-}NH_3(aq)} = 25.94 \times (10^3/T) - 42.25 \quad (3.1)$$

In that same study, the effect was observed to follow batch equilibrium fractionation (**Eq. 3.2**; as opposed to kinetic):

$$1000\ln\alpha_{NH_4^+\text{-}NH_3(aq)} = (\delta^{15}N_{final} - \delta^{15}N_{initial})/(1\text{-}f), \quad (3.2)$$

where $\delta^{15}N_{initial}$ and $\delta^{15}N_{final}$ are the isotopic compositions of the initial and remaining ammonium, respectively, and *f* refers to the molar fraction of remaining ammonium after a portion is converted to ammonia. Therefore, if we conservatively assume an initial $\delta^{15}N_{ammonium}$ = 5‰ (the average $\delta^{15}N$ value of marine nitrate), then the volatilization of 20.3% of NH_x from solution would result in residual NH_4 with a $\delta^{15}N$ = 13.8‰. This value is in good agreement with previous interpretations of ammonia volatilization in both modern and ancient systems, despite pH being below those typically invoked (pH ≥ 9.25) for such an effect. However, a sufficiently large reservoir of isotopically heavy NH4+ is needed to be able to preserve this value in sediments; the reservoir needs to be large enough to feed a significant fraction of the biological community. If the absolute amount of dissolved ammonium is very low (< 1μM), N_2 fixation is favored (Knapp 2012 Frontiers in Microbiology), which generates biomass with a $\delta^{15}N$ value near zero permil and would thus dilute the isotopic signature of ammonium-assimilators within sediments. This mechanism also explains why many aqueous environments, including the ocean (pH ~8.1), have pH levels that should impart some degrees of ammonia generation but do not express it in terms of $\delta^{15}N$. If circumstances do not favor the accumulation of ammonium and/or allow for unidirectional escape of ammonia from a endorheic setting, then it is unlikely that volatilization will manifest in the $\delta^{15}N$ record.

The astrobiological value of nitrogen cycling in shallow, alkaline-hypersaline lakes

Life may have originated via cycles of wet and dry in a shallow aqueous environment, and the evapo-concentration of critical biomolecules is a common aspect of proposed origin-of-life mechanisms (Damer & Deamer, 2020; Frenkel-Pinter et al., 2021; Menor Salván et al., 2020; Toner & Catling, 2019, 2020). Furthermore, hypersalinity may have negated some of the effects of the so-called faint young Sun (whereby the sun was ~30% less luminous ca. > 3.5Ga) by depressing the freezing point of liquid water and consequently lowering albedo at a planetary scale (Olson et al., 2020). Yet these attributes must be viewed through the context of pH. For instance, the combination of abiotic polymerization reactions of organic carbon molecules and the self-assembly of membranous compartments has only been directly observed in acidic environments (Deamer et al., 2019). On the other hand, alkaline systems are the more favorable setting for the accumulation of phosphorus, an essential but relatively scarce element needed by all life (Toner & Catling, 2020).

The $\delta^{15}N$ record of ancient closed-basin lakes may help identify hypersaline and high pH conditions, as opposed to those that are hypersaline and alkaline exclusively (i.e., not basic). It is necessary to focus on alkalinity and pH as discrete parameters when discussing Earth or Mars > 3.5Ga, because surface warmth on both planets was likely supported by the insulation of a thick CO_2 atmosphere (Catling & Zahnle, 2020; Wordsworth et al., 2021). The equilibration of high atmospheric pCO_2 with surface waters likely served to drive down pH (pH < 7; Halevy & Bachan, 2017; Krissansen-Totton et al., 2018) while also contributing elevated carbonate alkalinity (Stüeken, Tino et al., 2020; Hurowitz et al.,

2023). However, ammonia volatilization is a function of pH, not alkalinity. At pH = 7.1 and 30°C, ammonia represents less than 1% of an ideal NH_4^+-NH_3 solution; that percentage decreases with lower temperatures. Thus, the nitrogen isotope effects of ammonia speciation would be negligible in this scenario.

Determining whether elevated $\delta^{15}N$ signifies hypersalinity adds complexity. Additional contextual data supporting both endorheic behavior and shallow water column depth (and/or repeated desiccation such as evidence for evaporite minerals) would be necessary prerequisites for connecting hypersalinity to $\delta^{15}N$. If the system is relatively deep, than the mechanism described above does not apply. The approximate placement of this water depth threshold is currently unknown but is likely dependent on additional constraints, specifically the capacity for redox stratification. If ammonia volatilization appears to be occurring from a relatively deeper setting, then this setting is likely redox- and/or salinity-stratified, similar to what has been observed in the Holocene Lonar and Devils lakes (located in central India and North Dakota, USA, respectively; Lent et al., 1995; Menzel et al., 2013) and in ancient systems such as the Miocene Ries crater lake and the Permian Fengcheng formation (Stüeken, Tino et al., 2020; Xia et al., 2020). In those systems, reduced-N accumulation likely occurs/occurred at depth, and ammonia release likely is/was most significant during periods of water column overturn. Deeper settings require an additional line of evidence to parse the competing effects of denitrification and ammonia volatilization, such as $\delta^{15}N$ values that are static under a redox-stratified regime but transiently elevated during an interval of high pH (Stüeken, Tino et al., 2020). Denitrification is perhaps the process most commonly associated with significant $\delta^{15}N$

shifts. However, our results suggest that ancient lakes with $\delta^{15}N$ values attributed to denitrification and thus oxygen deficiency may warrant re-evaluation, provided the broader geochemical context supports hypersalinity and restriction.

Conclusion

An investigation of the sedimentary $\delta^{15}N$ of shallow, alkaline-hypersaline lakes in the Coorong region has uncovered a significant amount of intersystem isotopic variation. These differences include $\delta^{15}N$ values that extend up to 18.6‰, which is substantially higher than the vast majority of both modern and ancient sediments. Contextual data, primarily in the form of major element abundances and other stable isotope ratios ($\delta^{13}C_{carb}$, $\delta^{18}O_{carb}$, and $\delta^{13}C_{org}$), provide a means of interpreting the key biogeochemical parameters that drive the intersystem $\delta^{15}N$ variation. The most significant correlations involve salinity-associated elements (SAEs), particularly Na and Sr. We posit that this relationship is linked to the well-studied effects of Na-induced dampening of nitrification rates and, by extension, the accumulation of ammonic nitrogen. Principal component analyses expand upon this inference by suggesting that high Sr may be hindering nitrogen cycling; however, the effects of Sr toxicity on nitrifying bacteria if real are unknown and warrant further study. Closed-basin behavior, as interpreted via $\delta^{13}C_{carb}$-$\delta^{18}O_{carb}$ correlations, was inconsistent across the study sites. This is despite the observation that most of the systems having no apparent outlet. However, Halite Lake, which consistently had the highest $\delta^{15}N$ of any site, displayed a strong relationship positive covariation ($R^2 = 0.78$, $p < 0.001$)

between $\delta^{13}C_{carb}$ and $\delta^{18}O_{carb}$, indicating the expected endorheic behavior. Halite Lake also appears to be evapo-concentrated from seawater, in agreement with previous sedimentological and mineralogical evidence (Warren, 1990). This mechanism is likely the cause of high SAE concentrations there. Ultimately, we have proposed a novel mechanism for $\delta^{15}N$ elevation (**Fig. 3.7**) that incorporates findings from previous work on salterns, cation substitution in clays, and the degradation of organic matter during early diagenesis.

Restricted and shallow aqueous systems were present on the earliest Earth and Mars (>3.5 Ga). Evaluating ammonia volatilization via $\delta^{15}N$ can be a powerful indicator of high pH in these systems if contextual evidence supports hypersalinity. Such constraints on pH can inform not only nutrient cycling but also paleoatmospheric pCO_2, as well as the plausibility of proposed prebiotic reactions that may have facilitated the origin of life. Additionally, previous $\delta^{15}N$ data that have been attributed to denitrification may warrant re-interpretation, provided that the broader geochemical context supports hypersalinity and restriction. Our study exemplifies how leveraging well-studied modern environments as calibration sites can provide a much-needed expansion of interpretive geochemical frameworks.

References

Berner, R. A. (1980). *Early Diagenesis: A Theoretical Approach*. Princeton University Press.

Berner, R. A., & Raiswell, R. (1983). Burial of organic carbon and pyrite sulfur in sediments over phanerozoic time: a new theory. *Geochimica et Cosmochimica Acta*, *47*(5), 855–862.

Bro, R., & Smilde, A. K. (2014). Principal component analysis. *Anal. Methods*, *6*(9), 2812–2831.

Campbell, T. D., Febrian, R., McCarthy, J. T., Kleinschmidt, H. E., Forsythe, J. G., & Bracher, P. J. (2019). Prebiotic condensation through wet–dry cycling regulated by deliquescence. *Nature Communications*, *10*(1), 4508.

Catling, D. C., & Zahnle, K. J. (2020). The Archean atmosphere. *Science Advances*, *6*(9).

Chase, J. E., Arizaleta, M. L., & Tutolo, B. M. (2021). A Series of Data-Driven Hypotheses for Inferring Biogeochemical Conditions in Alkaline Lakes and Their Deposits Based on the Behavior of Mg and SiO2. *Minerals*, *11*(2), 106.

Cohen, A. S. (2003). Lakes as Archives of Earth History. In *Paleolimnology*. Oxford University Press.

Collister, J. W., & Hayes, J. M. (1991). A preliminary study of the carbon and nitrogen isotopic biogeochemistry of lacustrine sedimentary rocks from the Green River Formation, Wyoming, Utah, and Colorado. In M. L. Tuttle (Ed.), *Geochemical, biogeochemical, and sedimentological studies of the Green River Formation, Wyoming, Utah, and Colorado* (pp. C1–C14). USGS.

Damer, B., & Deamer, D. (2020). The Hot Spring Hypothesis for an Origin of Life. *Astrobiology*, *20*(4), 429–452.

De Deckker, P., & Geddes, M. (1980). Seasonal fauna of ephemeral saline lakes near the Coorong lagoon, South Australia. *Marine and Freshwater Research*, *31*(5), 677.

Deamer, D., Damer, B., & Kompanichenko, V. (2019). Hydrothermal Chemistry and the Origin of Cellular Life. *Astrobiology*, *19*(12), 1523–1537.

Ehlmann, B. L., Mustard, J. F., Fassett, C. I., Schon, S. C., Head III, J. W., Des Marais, D. J., Grant, J. A., & Murchie, S. L. (2008). Clay minerals in delta deposits and organic preservation potential on Mars. *Nature Geoscience*, *1*(6), 355–358.

Fairén, A. G., Rodríguez, N., Sánchez-García, L., Rojas, P., Uceda, E. R., Carrizo, D., Amils, R., & Sanz, J. L. (2023). Ecological successions throughout the desiccation of Tirez lagoon (Spain) as an astrobiological time-analog for wet-to-dry transitions on Mars. *Scientific Reports*, *13*(1), 1423.

Frenkel-Pinter, M., Rajaei, V., Glass, J. B., Hud, N. V., & Williams, L. D. (2021). Water and life: The medium is the message. *Journal of molecular evolution*, *89*(1-2), 2-11.

Garrels, R. M., & Christ, C. L. (1965). *Solutions, Minerals, and Equilibria* (1st ed.). Harper & Row.

Halevy, I., & Bachan, A. (2017). The geologic history of seawater pH. *Science*, *355*(6329), 1069-1071.

Hecky, R. E., Bootsma, H. A., Mugidde, R. M., & Bugenyi, F. W. B. (1996). Phosphorus Pumps, Nitrogen Sinks, and Silicon Drains: Plumbing Nutrients in the African Great Lakes. In *The Limnology, Climatology and Paleoclimatology of the East African Lakes* (pp. 205–224). Routledge.

Horgan, B. H. N., Anderson, R. B., Dromart, G., Amador, E. S., & Rice, M. S. (2020). The mineral diversity of Jezero crater: Evidence for possible lacustrine carbonates on Mars. *Icarus*, *339*, 113526.

Hurowitz, J. A., Catling, D. C., & Fischer, W. W. (2023). High Carbonate Alkalinity Lakes on Mars and their Potential Role in an Origin of Life Beyond Earth. *Elements*, *19*(1), 37–44.

Isaji, Y., Kawahata, H., Ogawa, N. O., Kuroda, J., Yoshimura, T., Jiménez-Espejo, F. J., Makabe, A., Shibuya, T., Lugli, S., Santulli, A., Manzi, V., Roveri, M., & Ohkouchi, N. (2019). Efficient recycling of nutrients in modern and past hypersaline environments. *Scientific Reports*, *9*(1), 3718.

Kessler, A. J., Bristow, L. A., Cardenas, M. B., Glud, R. N., Thamdrup, B., & Cook, P. L. M. (2014). The isotope effect of denitrification in permeable sediments. *Geochimica et Cosmochimica Acta*, *133*, 156–167.

Kjerfve, B. (1994). Coastal Lagoons. In B. Kjerfve (Ed.), *Coastal Lagoon Processes* (pp. 1–8).

Koops, H. P., Böttcher, B., Möller, U. C., Pommerening-Röser, A., & Stehr, G. (1990). Description of a new species of Nitrosococcus. *Archives of Microbiology*, *154*(3), 244–248.

Krissansen-Totton, J., Arney, G. N., & Catling, D. C. (2018). Constraining the climate and ocean pH of the early Earth with a geological carbon cycle model. *Proceedings of the National Academy of Sciences, 115*(16), 4105-4110.

Krull, E., Haynes, D., Lamontagne, S., Gell, P., McKirdy, D., Hancock, G., McGowan, J., & Smernik, R. (2009). Changes in the chemistry of sedimentary organic matter within the Coorong over space and time. *Biogeochemistry*, *92*(1–2), 9–25.

Lahav, N., White, D., & Chang, S. (1978). Peptide Formation in the Prebiotic Era: Thermal Condensation of Glycine in Fluctuating Clay Environments. *Science*, *201*(4350), 67–69.

Land, L. S. (1985). The Origin of Massive Dolomite. *Journal of Geological Education*, *33*(2), 112–125.

Lent, R. M., Lyons, W. B., Showers, W. J., & Johannesson, K. H. (1995). Late holocene paleoclimatic and paleobiologic records from sediments of Devils Lake, North Dakota. *Journal of Paleolimnology*, *13*(3), 193–207.

Li, L., Lollar, B. S., Li, H., Wortmann, U. G., & Lacrampe-Couloume, G. (2012). Ammonium stability and nitrogen isotope fractionations for –NH3(aq)–NH3(gas) systems at 20–70°C and pH of 2–13: Applications to habitability and nitrogen cycling in low-temperature hydrothermal systems. *Geochimica et Cosmochimica Acta*, *84*, 280–296.

Mawson, D. (1929). Some South Australian Algal Limestones In Process of Formation. *Quarterly Journal of the Geological Society*, *85*(1–4), 613–620.

Meglen, R. R. (1992). Examining large databases: a chemometric approach using principal component analysis. *Marine Chemistry*, *39*(1–3), 217–237.

Menor Salván, C., Bouza, M., Fialho, D. M., Burcar, B. T., Fernández, F. M., & Hud, N. V. (2020). Prebiotic Origin of Pre-RNA Building Blocks in a Urea "Warm Little Pond" Scenario. *ChemBioChem, 21*(24), 3504-3510.

Menzel, P., Gaye, B., Wiesner, M. G., Prasad, S., Stebich, M., Das, B. K., Anoop, A., Riedel, N., & Basavaiah, N. (2013). Influence of bottom water anoxia on nitrogen isotopic ratios and amino acid contributions of recent sediments from small eutrophic Lonar Lake, central India. *Limnology and Oceanography*, *58*(3), 1061–1074.

Mosley, L. M., Priestley, S., Brookes, J., Dittmann, S., Farkaš, J., Farrell, M., Ferguson, A. J., Gibbs, M., Hipsey, M., Huang, J., Lam-Gordillo, O., Simpson, S. L., Tyler, J. J., Waycott, M., & Welsh, D. T. (2023). Extreme eutrophication and salinisation in the Coorong estuarine-lagoon ecosystem of Australia's largest river basin (Murray-Darling). *Marine Pollution Bulletin*, *188*, 114648.

Muzuka, A. N. N., Ryner, M., & Holmgren, K. (2004). 12,000-Year, preliminary results of the stable nitrogen and carbon isotope record from the Empakai Crater lake sediments, Northern Tanzania. *Journal of African Earth Sciences*, *40*(5), 293–303.

Nissenbaum, A. (1975). The microbiology and biogeochemistry of the Dead Sea. *Microbial Ecology*, *2*(2), 139–161.

Oren, A. (1999). Bioenergetic Aspects of Halophilism. *Microbiology and Molecular Biology Reviews*, *63*(2), 334–348.

Olson, S., Jansen, M. F., Abbot, D. S., Halevy, I., & Goldblatt, C. (2022). The effect of ocean salinity on climate and its implications for Earth's habitability. *Geophysical research letters*, *49*(10), e2021GL095748.

Post, F. J. (1977). The microbial ecology of the Great Salt Lake. *Microbial Ecology*, *3*(2), 143–165.

Priestley, S. C., Tyler, J., Liebelt, S. R., Mosley, L. M., Wong, W. W., Shao, Y., Woolston, Z., Farrell, M., Welsh, D. T., Brookes, J. D., Collins, A. S., Keneally, C., & Farkaš, J. (2022). N and C Isotope Variations Along an Extreme Eutrophication and Salinity Gradient in the Coorong Lagoon, South Australia. *Frontiers in Earth Science*, *9*.

Rapin, W., Ehlmann, B. L., Dromart, G., Schieber, J., Thomas, N. H., Fischer, W. W., Fox, V. K., Stein, N. T., Nachon, M., Clark, B. C., Kah, L. C., Thompson, L., Meyer, H. A., Gabriel, T. S. J., Hardgrove, C., Mangold, N., Rivera-Hernandez, F., Wiens, R. C., & Vasavada, A. R. (2019). An interval of high salinity in ancient Gale crater lake on Mars. *Nature Geoscience*, *12*(11), 889–895.

Raudsepp, M. J., Wilson, S., & Morgan, B. (2023). Making Salt from Water: The Unique Mineralogy of Alkaline Lakes. *Elements*, *19*(1), 22–29.

Raudsepp, M. J., Wilson, S., Morgan, B., Patel, A., Johnston, S. G., Gagen, E. J., & Fallon, S. J. (2022). Non-classical crystallization of very high magnesium calcite and magnesite in the Coorong Lakes, Australia. *Sedimentology*, *69*(5), 2246–2266.

Rooze, J., & Meile, C. (2016). The effect of redox conditions and bioirrigation on nitrogen isotope fractionation in marine sediments. *Geochimica et Cosmochimica Acta*, *184*, 227–239.

Rosen, M. R., Miser, D. E., Starcher, M. A., & Warren, J. K. (1989). Formation of dolomite in the Coorong region, South Australia. *Geochimica et Cosmochimica Acta*, *53*(3), 661–669.

Rosen, M. R., Miser, D. E., & Warren, J. K. (1988). Sedimentology, mineralogy and isotopic analysis of Pellet Lake, Coorong region, South Australia. *Sedimentology*, *35*(1), 105–122.

Rysgaard, S., Thastum, P., Dalsgaard, T., Christensen, P. B., & Sloth, N. P. (1999). Effects of Salinity on NH4+ Adsorption Capacity, Nitrification, and Denitrification in Danish Estuarine Sediments. *Estuaries*, *22*, 21–30.

Shao, Y., Farkaš, J., Holmden, C., Mosley, L., Kell-Duivestein, I., Izzo, C., Reis-Santos, P., Tyler, J., Törber, P., Frýda, J., Taylor, H., Haynes, D., Tibby, J., & Gillanders, B. M. (2018). Calcium and strontium isotope systematics in the lagoon-estuarine environments of South Australia: Implications for water source mixing, carbonate fluxes and fish migration. *Geochimica et Cosmochimica Acta*, *239*, 90–108.

Shao, Y., Farkaš, J., Mosley, L., Tyler, J., Wong, H., Chamberlayne, B., Raven, M., Samanta, M., Holmden, C., Gillanders, B.M. and Kolevica, A. (2021). Impact of salinity and carbonate saturation on stable Sr isotopes (δ88/86Sr) in a lagoon-estuarine system. *Geochimica et Cosmochimica Acta*, *293*, 461-476.

Stein, N., Grotzinger, J. P., Schieber, J., Mangold, N., Hallet, B., Newsom, H., Stack, K. M., Berger, J. A., Thompson, L., Siebach, K. L., Cousin, A., Le Mouélic, S., Minitti, M., Sumner, D. Y., Fedo, C., House, C. H., Gupta, S., Vasavada, A. R., Gellert, R., … Dehouck, E. (2018). Desiccation cracks provide evidence of lake drying on Mars, Sutton Island member, Murray formation, Gale Crater. *Geology*, *46*(6), 515–518.

Stüeken, E. E., Buick, R., & Schauer, A. J. (2015). Nitrogen isotope evidence for alkaline lakes on late Archean continents. *Earth and Planetary Science Letters*, *411*, 1–10.

Stüeken, E. E., Tino, C., Arp, G., Jung, D., & Lyons, T. W. (2020). Nitrogen isotope ratios trace high-pH conditions in a terrestrial Mars analog site. *Science Advances*, *6*(9).

Talbot, M. R. (1990). A review of the palaeohydrological interpretation of carbon and oxygen isotopic ratios in primary lacustrine carbonates. *Chemical Geology: Isotope Geoscience Section*, *80*(4), 261–279.

Talbot, M. R., & Johannessen, T. (1992). A high resolution palaeoclimatic record for the last 27,500 years in tropical West Africa from the carbon and nitrogen isotopic composition of lacustrine organic matter. *Earth and Planetary Science Letters*, *110*(1–4), 23–37.

Tesdal, J.-E., Galbraith, E. D., & Kienast, M. (2013). Nitrogen isotopes in bulk marine sediment: linking seafloor observations with subseafloor records. *Biogeosciences*, *10*(1), 101–118.

Toner, J. D., & Catling, D. C. (2019). Alkaline lake settings for concentrated prebiotic cyanide and the origin of life. *Geochimica et Cosmochimica Acta*, *260*, 124–132.

Toner, J. D., & Catling, D. C. (2020). A carbonate-rich lake solution to the phosphate problem of the origin of life. *Proceedings of the National Academy of Sciences of the United States of America*, *117*(2), 883–888.

Tutolo, B. M., & Tosca, N. J. (2023). Dry, Salty, and Habitable: The Science of Alkaline Lakes. *Elements*, *19*(1), 10–14.

von der Borch, C. (1965). The distribution and preliminary geochemistry of modem carbonate sediments of the Coorong area, South Australia. *Geochimica et Cosmochimica Acta*, *29*(7), 781–799.

von der Borch, C. C. (1976). Stratigraphy and Formation of Holocene Dolomitic Carbonate Deposits of the Coorong Area, South Australia. *Journal of Sedimentary Research*, *46*(4), 952–966.

Wacey, D., Wright, D. T., & Boyce, A. J. (2007). A stable isotope study of microbial dolomite formation in the Coorong Region, South Australia. *Chemical Geology*, *244*(1–2), 155–174.

Warren, J. K. (1988). Sedimentology of coorong dolomite in the Salt Creek region, South Australia. *Carbonates and Evaporites*, *3*(2), 175–199.

Warren, J. K. (1990). Sedimentology and Mineralogy of Dolomitic Coorong Lakes, South Australia. *Journal of Sedimentary Research*, *60*(6), 843–858.

Webster, I. T. (2010). The hydrodynamics and salinity regime of a coastal lagoon – The Coorong, Australia – Seasonal to multi-decadal timescales. *Estuarine, Coastal and Shelf Science*, *90*(4), 264–274.

Wordsworth, R., Knoll, A. H., Hurowitz, J., Baum, M., Ehlmann, B. L., Head, J. W., & Steakley, K. (2021). A coupled model of episodic warming, oxidation and geochemical transitions on early Mars. *Nature Geoscience*, *14*(3), 127–132.

Wright, D. T. (1999). The role of sulphate-reducing bacteria and cyanobacteria in dolomite formation in distal ephemeral lakes of the Coorong region, South Australia. *Sedimentary Geology*, *126*(1–4), 147–157.

Wright, D. T., & Wacey, D. (2005). Precipitation of dolomite using sulphate-reducing bacteria from the Coorong Region, South Australia: significance and implications. *Sedimentology*, *52*(5), 987–1008.

Xia, L., Cao, J., Stüeken, E. E., Hu, W., & Zhi, D. (2022). Linkages between nitrogen cycling, nitrogen isotopes, and environmental properties in paleo-lake basins. *GSA Bulletin*, *134*(9–10), 2359–2372.

Xia, L., Cao, J., Stüeken, E. E., Zhi, D., Wang, T., & Li, W. (2020). Unsynchronized evolution of salinity and pH of a Permian alkaline lake influenced by hydrothermal fluids: A multi-proxy geochemical study. *Chemical Geology*, *541*, 119581.

Xu, H., Ai, L., Tan, L., & An, Z. (2006). Stable isotopes in bulk carbonates and organic matter in recent sediments of Lake Qinghai and their climatic implications. *Chemical Geology*, *235*(3–4), 262–275.

Zastrow, A. M., & Glotch, T. D. (2021). Distinct Carbonate Lithologies in Jezero Crater, Mars. *Geophysical Research Letters*, *48*(9).

Chapter 4

Taking on big nitrogen: Understanding the pathways, controls, and significance of extreme $\delta^{15}N$ enrichments in modern and ancient lakes

Introduction

Nitrogen cycling and the sedimentary preservation of its outcomes are major themes in biogeochemical studies of modern and ancient aqueous settings. Accordingly, stable nitrogen isotope ratios [$\delta^{15}N$] have the capacity to inform many aspects of aqueous environments, including redox conditions and biological productivity. Nitrogen is perhaps the most cryptic of the traditional isotope systems—which also includes carbon [$\delta^{13}C$], hydrogen [$\delta^{2}H$], oxygen [$\delta^{18}O$], and sulfur [$\delta^{34}S$] (Sharp, 2017). Of those elements, which excludes phosphorus because it is monoisotopic, nitrogen is the least bioavailable and most likely to be a limiting nutrient (Howarth & Marino, 2006; Sigman & Fripiat, 2019; Zhang et al., 2020). Thus, N abundances tend to be low in most geologic samples and can be challenging to analyze and interpret.

There are several empirically verified redox reactions that are capable of generating large shifts in nitrogen isotope composition (Stüeken et al., 2016). Many of these pathways are microbiological and evolved early in Earth history (**Fig. 4.1**). Yet in the rock record, $\delta^{15}N$ exhibits the lowest amount of variance of any traditional stable isotope system despite its low mass and large relative mass difference between the major isotopes (Stüeken et al., 2016). Nitrogen fixation via the molybdenum [Mo]-bearing nitrogenase enzyme—the process that kickstarts N cycling in most environments by converting N_2 to NH_4^+—only

imparts a small isotope effect: ε ≈ -1‰ to +2‰ ($\varepsilon = \delta^{15}N_{product} - \delta^{15}N_{reactant}$) (Fogel & Cifuentes, 1993; Talbot, 2002). After fixation, the quantitative and/or rapid nature of multiple reactions during microbial processing of bioavailable-N tends to leave a muted, if any, signal. For example, ammonium assimilation can impart a fractionation of up to ε = -27‰ (Hoch et al., 1992); however, this is rarely (if ever) expressed in the long-term sedimentary record, possibly suggesting that bioavailable NH_4^+ reservoirs are often small and therefore rapidly taken up and incorporated into biomass with little or no accompanying fractionation (Stüeken et al., 2016).

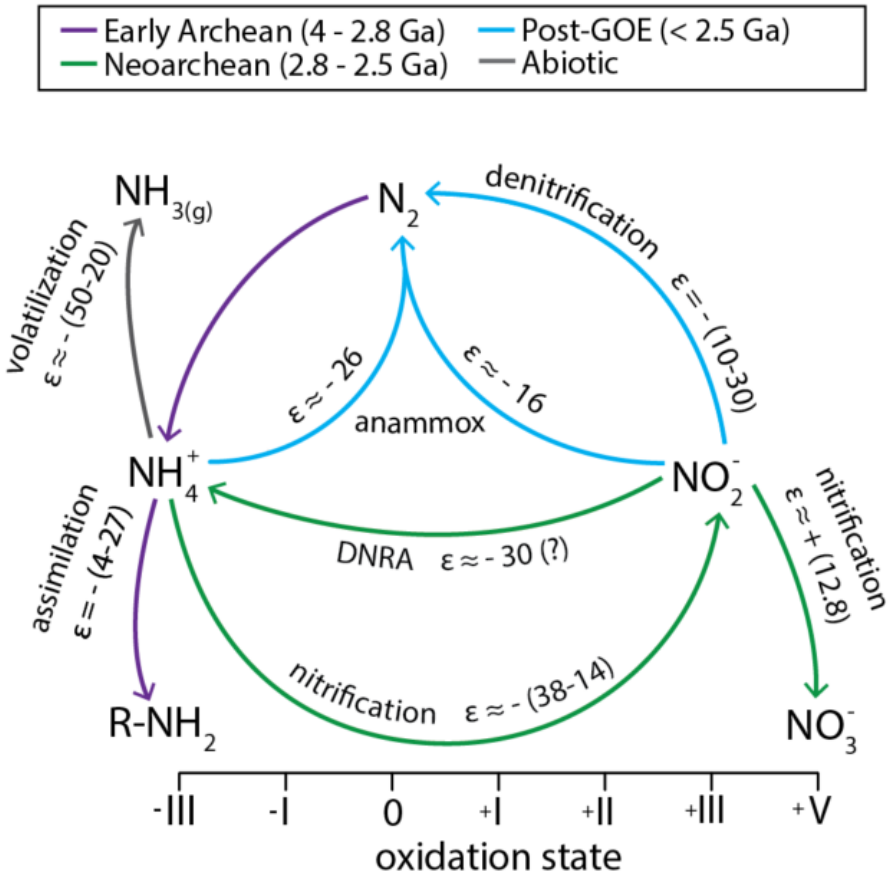

Figure 4.1 A simplified depiction of the nitrogen cycle that is color-coded based on the geologic interval at which a given pathway emerged. Approximate fractionations ($\varepsilon = \delta^{15}N_{product} - \delta^{15}N_{reactant}$) are provided for most of the depicted pathways. Nitrogen fixation results in near-zero fractionation and is not highlighted to enhance visual clarity. See Stüeken et al. (2016) for a review of these metabolic processes and their fractionation effects.

Over the last decade or so, an increased amount of attention has been given to the abiotic phenomenon of ammonia volatilization and its large fractionation effect (e.g., Deng et al., 2018; Li et al., 2012; Stüeken et al., 2015; Stüeken, Tino et al., 2020; Xia et al., 2020). In much of this previous work, ammonia volatilization has been linked to high $\delta^{15}N$ values ≥ 10‰. This distinction is made because such signals are rare; only ~5% of all reported bulk $\delta^{15}N$ values from greenschist and sub-greenschist facies exceed 10‰ (Stüeken et al., 2016). This relatively unusual phenomenon requires a specific set of conditions. At a minimum, pH > 7.5 seems necessary for NH_3 volatilization to affect $\delta^{15}N$ noticeably, based on the pH-dependent nature of the relationship between NH_4^+ and NH_3 in solution (pK_a = 9.25; **Chapter 3**; Li et al., 2012). Depending on the depositional setting, it appears that particular conditions pertaining to multiple parameters (i.e., pH, salinity and/or redox stratification, and endorheic behavior) may be necessary prerequisites for the significant elevation of $\delta^{15}N$ (**Chapter 3**; Stüeken, Tino et al., 2020; Xia et al., 2020). Thus, a single geochemical variable (i.e., $\delta^{15}N$) may provide multiple geochemical constraints on a given setting, which can be unmixed and calibrated for ancient applications when complementary data are generated.

The primary locations of NH_3 volatilization are intriguing, particularly with regards to the earliest Earth and Mars (> 3.5 Ga). This topic is discussed in more detail in **Chapters 2 and 3**. Briefly, alkaline lakes are an ideal environment for elevated $\delta^{15}N$ (Collister & Hayes, 1991; Stüeken, Tino et al., 2020; Talbot & Johannessen, 1992; Xia et al., 2020). Because NH_3 volatilization is linked to high pH and not necessarily alkalinity, this may inform whether pCO_2 was high enough to significantly decouple pH and alkalinity in

ancient lakes (Stüeken, Tino et al., 2020). Elevated pCO_2 is thought to play a large role in insulating the surfaces of early Earth and Mars in the face of a less luminous young Sun (Feulner, 2012; Sagan & Mullen, 1972). However, Mars provides very little geologic evidence for abundant pCO_2 in the past (e.g., there is a paucity of non-hydrothermal carbonate units; Niles et al., 2013). A pH proxy such as ammonia volatilization, as manifested in $\delta^{15}N$, could aid in filling that gap.

At present, there is no review that seeks to collect and summarize multiple sites of ammonia volatilization. To address this gap, we describe four systems to complement our studies of Miocene Ries crater (**Chapter 2**) and Holocene Coorong lakes (**Chapter 3**) with the hope of gleaning new insights into the possible depositional mechanisms and geochemical parameters associated with elevated $\delta^{15}N$. Key topics include the balance of NH_3 volatilization and denitrification, which is the conversion of NO_x to N_2 with maximum ε of -30‰, as well as the roles of the water column depth, salinity, and temperature in determining the primary mode and intensity of $\delta^{15}N$ fractionation. This discussion is centered around the presentation of a new data set from one of the foremost lacustrine systems in the geologic record—the Eocene Green River Formation. First, the new data from the Green River Formation will be reported and discussed. Then there will be brief, separate discussions for the three other sites, which are, in order of oldest to youngest, the (1) Tumbiana Formation (2.72 Ga; Blake et al., 2004); (2) Fengcheng Formation (ca. 305-296 Ma; Wang et al., 2022); and (3) Lake Bosumtwi (1.07 Ma-present; Koeberl et al., 1997). This step is followed by a synthesis section to evaluate how a holistic consideration of all the described sites allows for a deeper understanding of $\delta^{15}N$ elevation.

Sampling and Methods

A total of 113 samples were collected and analyzed from two drill cores of the Uinta Basin within the Eocene Green River Formation [GRF]—PR-15-7c (n = 78) and Skyline-16 (n = 35) (**Fig. 4.2**). Access to both was provided by the Utah Geological Survey at the Utah Core Research Center with support from Carie Frantz (Weber State University) and Michael Vanden Berg (Utah Geological Survey). The sample set spans ~6 Myr (from 54 Ma to 48 Ma), which includes four distinct units. They are, from oldest to youngest, the (1) Uteland Butte Member; (2) Carbonate Marker Unit; (3) Mahogany zone; and (4) Parachute Creek Member (Birgenheier et al., 2020; Elson et al., 2022; French et al., 2020).

Samples were cut with a rock saw and/or trimmed with a rock chipper, removing all potentially contaminated exteriors. The interiors were then examined, and features such as sulfide veins were deliberately avoided. Samples were then hammered into sub-cm sized pieces, dehydrated at 50°C for ≥ 48 hours, and powdered in a ball mill. Roughly 0.5 g of powder of each sample was decarbonated with 2 N HCl at 60°C overnight and rinsed three times with 18 MΩ DI-H_2O (Stüeken et al., 2015).

The residues were dried and weighed into tin capsules for organic carbon and total nitrogen isotopes analyses at the University of St Andrews. These measurements were performed on an EA Isolink coupled to a MAT253 isotope ratio mass spectrometer via a Conflo IV. The data were calibrated with international reference materials USGS-40 and USGS-41. Long-term reproducibility was tracked with the rock standard SGR-1. Data are expressed in standard delta notation relative to VPDB for $\delta^{13}C_{org}$ and air for $\delta^{15}N$. Reproducibility for all stable isotope values (1SD) was 0.9‰ or better. Total organic

carbon [TOC] and total nitrogen of the decarbonated materials [TN_{decarb}] were also collected through the above process. Average relative error was 0.18 wt% (n = 40) for TOC (median sample was 6.82 wt% TOC, n = 113) and 0.02 wt% (n = 43) for TN_{decarb}.

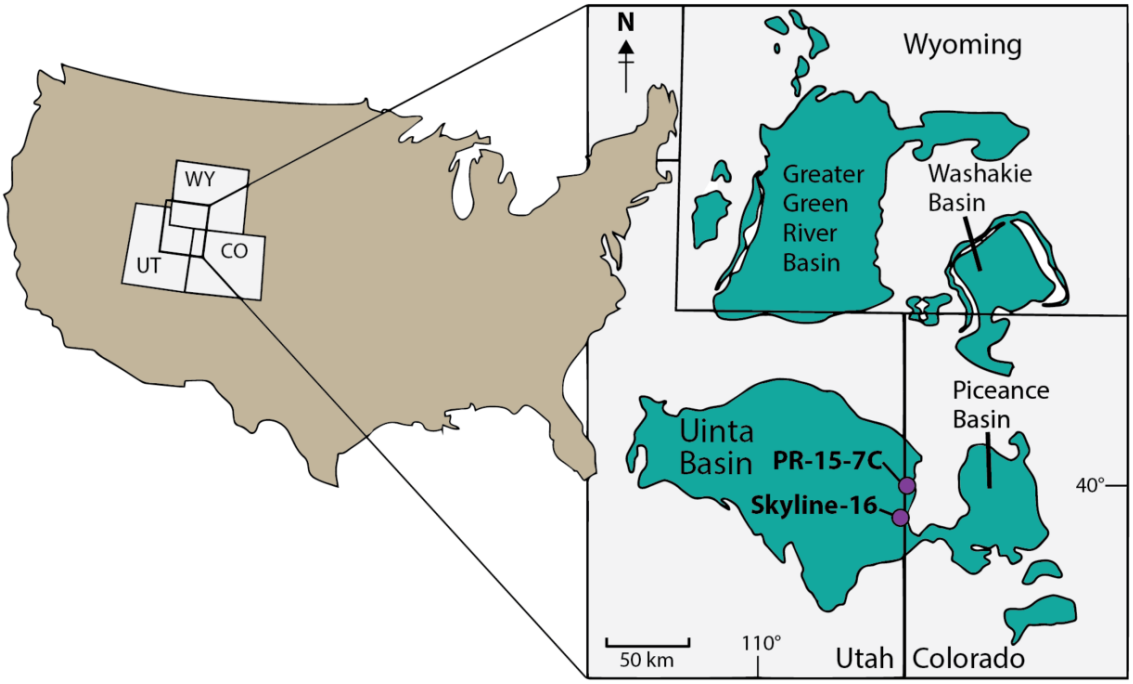

Figure 4.2 Geographical context for the Green River Formation, including the locations of all drill core and field sites sampled or referenced in this study. Adapted from Elson et al. (2022) and French et al. (2020).

Results

The $\delta^{15}N$ data for GRF range from 6.0‰ to 21.4‰, broadly decreasing in value with increasing depth. The mean values of each unit, progressing from oldest to youngest, follow: Uteland Butte Member (mean = 8.3‰, n = 28, σ = 1.3‰), Carbonate Marker Unit (mean = 12.5‰, n = 31, σ = 1.8‰), Mahogany zone (mean = 15.7‰, n = 30, σ = 1.0‰), and Parachute Creek Member (mean = 18.3‰, n = 24, σ = 1.5‰). The $\delta^{13}C_{org}$ data are comparatively invariant, ranging from -25.8‰ to -33.8‰. The mean $\delta^{13}C_{org}$ is -29.0‰ (n

= 113, σ = 1.6‰), and the mean of each unit is within ±1.1‰ of the mean of the entire dataset. The $\delta^{13}C_{org}$ agrees with previous studies, providing no novel insights within the scope of our study. TOC varies widely, ranging from 0.33 to 49.7 wt% (mean = 12.19 wt%, n = 113, σ = 11.0 wt%). Most of the exceptionally high values occur within the Mahogany zone (mean = 24.3 wt%, n = 24, σ = 11.52 wt%), in line with previous studies. There is strong correlation between TOC and TN_{decarb} ($R^2 = 0.91$, $p < 0.001$), indicating that the nitrogen analyzed is almost exclusively sourced from organic matter. In that sense, TN_{decarb} follows the same overall and unit-to-unit trends as described above for TOC. However, as is the case in all organic-bearing samples, TN_{decarb} values are much lower than those for TOC, which range from 0.06 to 1.68 wt% (mean = 0.46 wt%, n = 113, σ = 0.37 wt%).

Table 4.1 Geochemical data from the PR-157C and Skyline-16 cores. Reproducibility for $\delta^{15}N$ and $\delta^{13}C$ are 0.9‰ (1SD) or better. Average relative errors (1SD/mean) are 0.02% for TN_{decarb} and 0.18% for TOC.

Depth (m)	TN_{decarb} (wt%)	$\delta^{15}N$ (‰)	TOC (wt%)	$\delta^{13}C_{org}$ (‰)	Unit
PR-15-7C core					
33.67-33.74	0.70	13.44	9.51	-31.62	Mahogany zone
34.01-34.08	0.77	14.21	15.03	-32.83	Mahogany zone
36.41-36.48	1.23	14.59	42.35	-29.88	Mahogany zone
36.66-36.73	0.98	16.16	27.78	-31.13	Mahogany zone
37.66-37.73	0.53	16.34	14.34	-30.16	Mahogany zone
38.78-38.85	1.25	15.50	37.21	-26.38	Mahogany zone
39.75-39.83	1.35	15.51	37.84	-31.61	Mahogany zone
40.04-40.12	1.30	15.29	33.31	-29.48	Mahogany zone

40.62-40.70	1.13	15.08	29.57	-28.90	Mahogany zone
41.35-41.43	0.67	17.02	19.49	-30.94	Mahogany zone
41.78-41.85	0.86	16.10	27.69	-29.66	Mahogany zone
42.05-42.13	0.56	16.48	15.21	-31.75	Mahogany zone
43.03-43.10	1.12	16.10	34.30	-28.10	Mahogany zone
43.21-43.28	0.75	14.55	20.52	-28.77	Mahogany zone
43.68-43.75	0.87	14.19	18.94	-29.08	Mahogany zone
44.20-44.28	0.75	14.53	19.34	-28.53	Mahogany zone
46.57-46.64	0.85	16.55	24.96	-30.73	Mahogany zone
47.73-47.80	0.91	16.83	28.23	-28.09	Mahogany zone
51.10-51.17	0.62	14.52	6.40	-31.50	Mahogany zone
369.19-369.26	0.33	14.48	11.54	-31.12	Carbonate Marker Unit
370.42-370.50	0.11	12.70	2.36	-32.51	Carbonate Marker Unit
371.54-371.62	0.65	13.45	18.25	-31.29	Carbonate Marker Unit
372.99-373.07	0.11	11.49	1.93	-31.62	Carbonate Marker Unit
373.56-373.64	0.27	16.85	7.69	-32.53	Carbonate Marker Unit
374.04-374.12	0.36	13.96	10.04	-31.63	Carbonate Marker Unit
376.07-376.15	0.52	14.22	18.92	-31.60	Carbonate Marker Unit
376.63-376.71	0.31	14.48	8.61	-31.44	Carbonate Marker Unit
377.71-377.79	0.20	15.69	5.33	-33.82	Carbonate Marker Unit
378.25-378.33	0.35	12.95	9.37	-31.98	Carbonate Marker Unit
379.72-379.80	0.18	12.76	2.55	-30.72	Carbonate Marker Unit
380.70-380.78	0.20	11.72	2.30	-31.58	Carbonate Marker Unit
383.73-383.81	0.25	11.18	3.18	-31.25	Carbonate Marker Unit

385.88-385.96	0.17	10.43	3.02	-32.84	Carbonate Marker Unit
387.08-387.16	0.35	13.21	15.92	-31.58	Carbonate Marker Unit
389.86-389.93	0.18	11.59	3.51	-32.14	Carbonate Marker Unit
393.32-393.40	0.34	13.99	11.29	-30.82	Carbonate Marker Unit
395.27-395.35	0.25	13.03	9.00	-29.89	Carbonate Marker Unit
397.00-397.08	0.29	12.72	9.44	-31.79	Carbonate Marker Unit
399.77-399.84	0.09	10.84	1.91	-30.75	Carbonate Marker Unit
401.48-401.55	0.21	12.52	6.25	-31.94	Carbonate Marker Unit
403.89-403.96	0.17	13.31	4.37	-28.77	Carbonate Marker Unit
404.18-404.25	0.27	14.05	8.36	-30.40	Carbonate Marker Unit
405.00-405.07	0.18	9.89	4.45	-31.66	Carbonate Marker Unit
409.96-410.03	0.20	13.11	5.67	-31.60	Carbonate Marker Unit
410.58-410.65	0.30	11.71	12.02	-28.20	Carbonate Marker Unit
411.94-412.01	0.20	13.69	9.98	-29.34	Carbonate Marker Unit
413.53-413.61	0.15	9.88	4.54	-30.32	Carbonate Marker Unit
414.22-414.29	0.15	9.93	3.96	-30.54	Carbonate Marker Unit
415.03-415.10	0.08	9.76	1.71	-30.01	Carbonate Marker Unit
415.82-415.89	0.10	9.31	2.59	-29.68	Carbonate Marker Unit
430.81-430.88	0.74	9.71	21.84	-26.98	Uteland Butte
431.32-431.40	0.07	7.00	0.66	-26.66	Uteland Butte
439.06-439.13	0.06	7.76	0.33	-25.82	Uteland Butte
441.08-441.15	0.11	6.92	2.60	-29.42	Uteland Butte
441.38-441.45	0.10	6.46	2.22	-29.64	Uteland Butte
447.76-447.83	0.24	7.73	7.47	-27.91	Uteland Butte

449.69-449.76	0.25	11.39	8.47	-28.22	Uteland Butte
450.16-450.23	0.14	8.56	4.06	-31.11	Uteland Butte
451.89-451.96	0.90	7.27	34.60	-28.79	Uteland Butte
453.08-453.16	0.17	9.45	5.72	-31.04	Uteland Butte
454.98-455.05	0.12	10.49	3.50	-31.22	Uteland Butte
456.46-456.53	0.12	8.36	4.86	-31.08	Uteland Butte
457.36-457.43	0.27	9.47	7.11	-26.92	Uteland Butte
460.33-460.41	0.15	8.51	5.92	-30.99	Uteland Butte
460.42-460.50	0.16	11.32	8.97	-29.59	Uteland Butte
463.73-463.80	0.08	7.58	2.33	-26.70	Uteland Butte
465.54-465.61	0.11	7.19	4.05	-29.26	Uteland Butte
466.52-466.59	0.09	5.97	3.13	-30.30	Uteland Butte
467.10-467.17	0.13	6.98	2.85	-27.91	Uteland Butte
467.77-467.84	0.12	6.63	4.33	-28.82	Uteland Butte
468.90-468.97	0.11	7.75	5.20	-31.81	Uteland Butte
469.14-469.21	0.09	7.94	2.24	-28.22	Uteland Butte
469.63-469.70	0.08	8.14	3.34	-31.39	Uteland Butte
472.43-472.50	0.09	10.18	3.26	-32.89	Uteland Butte
474.75-474.82	0.11	7.40	1.67	-28.69	Uteland Butte
476.06-476.13	0.14	7.37	4.25	-27.69	Uteland Butte
476.71-476.78	0.15	8.50	8.04	-29.08	Uteland Butte
477.30-477.37	0.07	8.43	6.52	-30.15	Uteland Butte

Skyline-16 core

29.78-29.87	0.75	20.15	16.35	-30.93	Parachute Creek Member
29.89-29.98	0.85	20.58	18.26	-31.68	Parachute Creek Member
30.23-30.32	0.23	20.76	3.92	-29.09	Parachute Creek Member
30.48-30.57	0.20	18.30	3.81	-29.16	Parachute Creek Member
31.52-31.61	0.28	17.36	4.13	-28.82	Parachute Creek Member
32.23-32.32	0.27	18.08	4.22	-28.71	Parachute Creek Member
32.38-32.47	0.21	17.20	2.56	-27.39	Parachute Creek Member
32.48-32.51	0.24	18.78	2.79	-27.78	Parachute Creek Member
42.28-42.37	0.56	21.44	12.44	-28.69	Parachute Creek Member
42.42-42.51	0.96	19.88	21.56	-29.26	Parachute Creek Member
42.72-42.81	1.36	19.49	35.73	-27.64	Parachute Creek Member
46.09-46.18	0.51	16.98	6.49	-27.79	Parachute Creek Member
46.85-46.94	0.48	18.88	8.96	-27.79	Parachute Creek Member
47.00-47.09	0.58	18.35	12.33	-28.49	Parachute Creek Member
47.28-47.37	0.80	15.72	21.45	-28.97	Parachute Creek Member
48.69-48.78	0.43	17.37	8.04	-27.45	Parachute Creek Member
48.88-48.97	0.56	18.16	10.63	-27.88	Parachute Creek Member
53.56-53.65	0.40	16.10	5.99	-28.48	Parachute Creek Member
53.95-54.04	0.57	18.15	11.54	-28.30	Parachute Creek Member
54.21-54.29	0.51	18.46	10.08	-28.42	Parachute Creek Member
54.61-54.70	0.31	18.21	7.97	-29.24	Parachute Creek Member
56.56-56.64	0.57	16.73	9.68	-28.78	Parachute Creek Member
57.76-57.85	0.57	15.72	12.83	-30.44	Parachute Creek Member
58.22-58.31	0.31	18.92	6.66	-29.52	Parachute Creek Member

140.29-140.36	1.68	16.24	49.46	-31.31	Mahogany zone
140.97-141.04	0.91	15.15	28.33	-29.01	Mahogany zone
141.22-141.29	1.46	14.98	40.16	-30.00	Mahogany zone
141.81-141.88	0.57	16.85	16.67	-30.01	Mahogany zone
142.20-142.27	1.28	16.42	38.79	-28.77	Mahogany zone
142.75-142.83	0.23	16.64	8.16	-28.71	Mahogany zone
144.33-144.41	0.51	17.47	9.14	-28.42	Mahogany zone
145.09-145.16	0.36	15.29	7.86	-31.75	Mahogany zone
145.98-146.05	1.20	16.97	35.11	-31.41	Mahogany zone
147.25-147.32	0.56	16.74	15.87	-31.11	Mahogany zone
148.85-148.92	0.57	16.29	18.00	-31.11	Mahogany zone

Discussion

Eocene Green River Formation

The GRF is among the best-documented ancient lacustrine sites (Carroll & Bohacs, 1999; Smith et al., 2008) and is, in many ways, the archetypal alkaline paleolake system. It contains a well-preserved organic-rich sequence that has been the subject of extensive and ongoing academic and economic interest, including notable deposits of minerals such as trona and nahcolite that record highly elevated alkalinity values in the ancient waters (Bradley, 1931; Collister et al., 1992; Lowenstein et al., 2017). The interval under consideration (54-48 Ma) is synchronous with the Early Eocene Climatic Optimum (EECO; 53.3-49.1 Ma) and represents a time of significant contraction of the water mass

in the GRF basin. At 54 Ma, there were at least three major separate basins and several minor ones that defined the overall GRF system (Smith et al., 2008). By 48 Ma, the northern portions of the system (e.g., the Greater Green River and Washakie basins) had effectively dried up, with only the Piceance and Uinta basins retaining appreciable water (Smith et al., 2008). As a result, the Uinta Basin possesses among the longest-lived lacustrine records of any site within the GRF (Vanden Berg & Birgenheier, 2017).

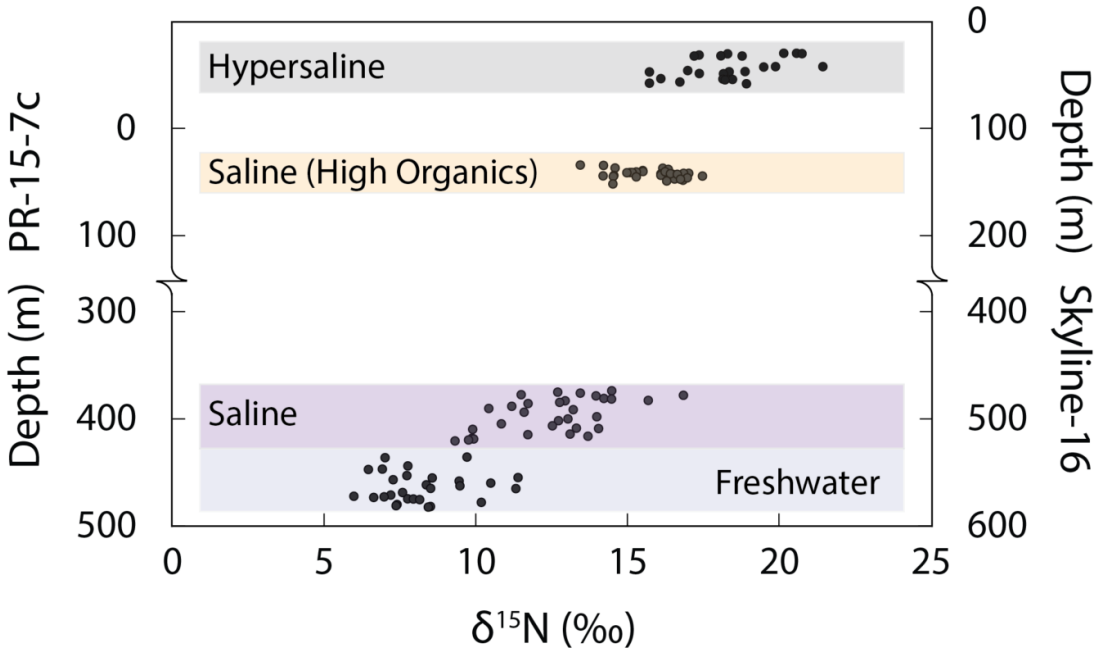

Figure 4.3 Scatter plot of all GRF (Uinta Basin) $\delta^{15}N$ values reported in this study, which were collected from the PR-15-7c and Skyline-16 cores. Qualitative descriptions of certain depths (e.g., "Freshwater") are derived from geochemical and sedimentological data from multiple previous studies including Birgenheier et al. (2020), Elson et al. (2022), French et al. (2020), and Walters et al. (2020).

The reported $\delta^{15}N$ composition (**Table 4.1; Figure 4.3**) increases along an interval that broadly marks a transition in the Uinta Basin from a freshwater to a hypersaline-alkaline system. A pH range of at least 8 to 9.5 has long been assumed for the alkaline intervals (e.g., Smith & Robb, 1973), although the source of this alkalinity remains a

subject of complex debate (Lowenstein et al., 2017). In a previous study, Collister & Hayes (1991) found an elevated range of $\delta^{15}N$ values (10.1 to 20.7‰) in their kerogen extracts, which is narrower than those reported here (**Table 4.**1). Additionally, their sample set was smaller (n = 49) and broader in distribution (i.e., from multiple basins comprising the GRF), with only 10 samples from the Uinta Basin.

Our data disagree with a key aspect of the Collister & Hayes (1991) study—specifically their claim that there is no connection between the most enriched $\delta^{15}N$ and evidence of evapo-concentration. We see a clear indication that the most saline and/or evaporative intervals show the highest $\delta^{15}N$ values, at least within the Uinta Basin (**Fig. 4.3**). The previous interpretation of Collister & Hayes (1991) acknowledged the role of NH_3 volatilization at high pH but argued that evapo-concentration led to lower $\delta^{15}N$ based on the notion that hypersalinity decreased nitrification, which in turn dampened denitrification and its isotope effect. We agree that hypersalinity decreases nitrification. However, based on our findings from the Coorong lakes in Australia (**Chapter 3**) and the work of Isaji et al. (2019), we argue that hypersalinity facilitated the accumulation of ammonic N by inhibiting microbial nitrification, leading to enhanced ammonia volatilization. In any case, the GRF displays exceptionally elevated values in its most hypersaline interval. Our maximum $\delta^{15}N$ (21.4‰) is the highest reported for GRF studies and is among the highest reported values from the rock record, although it is vastly exceeded values from the Archean Tumbiana Formation.

Tumbiana Formation

The Tumbiana Formation of the Fortescue Group sits atop the Pilbara Craton in Western Australia and displays a maximum $\delta^{15}N$ of 50.4‰, which is the highest known value in the rock record (Stüeken et al., 2015; Thomazo et al., 2011). Thomazo et al. (2011) discovered this signal, which displays a mean value of 29.5‰ ± 10.1‰ (n = 30, ranging from 8.6‰ to 50.4‰). This site was also examined by Stüeken et al. (2015), resulting in a mean $\delta^{15}N$ value of 31.9‰ ± 6.8‰ (n = 17, ranging from 22.9‰ to 44.0‰). These signals were deposited within a system of lakes that formed on top of flood basalts and volcanic ash deposits at 2.72 Ga (Buick, 1992; Coffey et al., 2013). As a result, weathering of these materials is thought to have driven pH up via a process analogous basaltic glass hydrolysis (Gislason & Eugster, 1987; Stüeken et al., 2015; Stüeken, Tino et al., 2020). A key and perhaps unique feature at Tumbiana is the extremely elevated C/N ratios (485 ± 327) attributable to unusually low N contents (< 21 ppm; Stüeken et al., 2015; Thomazo et al., 2011). Stüeken et al. (2015) linked the low N contents to significant N loss via ammonia volatilization from a restricted setting, resulting also in the observed elevated $\delta^{15}N$. This model was in disagreement with a previous interpretation by Thomazo et al. (2011), who suggested the primary fractionation mechanism was partial nitrification of ammonium followed by denitrification and/or N_2O escape. Perhaps the most puzzling aspect of the $\delta^{15}N$ data for the Tumbiana Formation is that they are on average much higher than any other site (the next highest value on record is ~31‰ at the marine 1.92 Ga Aravalli supergroup, which may be impacted by strong metamorphic alteration; Papineau et al., 2009). The Permian Fengcheng Formation (described directly below) appears to be an ideal

system for NH_3 volatilization, but the highest values there are at least 25‰ lower than the maximum value observed at the Tumbiana Formation. Stüeken et al. (2015) argued at the time that these unusually large values in the Tumbiana Formation may have been facilitated by the anoxic Archean atmosphere, which perhaps facilitated NH_3 escape from the lake waters.

Fengcheng Formation

There has been a recent flurry of research surrounding the alkaline lacustrine rocks of the Permian Fengcheng Formation (Bian et al., 2010; Zhang et al., 2018), including work targeting transitions in pH and salinity (Xia et al., 2020, 2022). The Fengcheng Formation sits within the Mahu sag of the Junggar Basin in Northwest China and is thought to have gone through multiple episodes of lake level rise and fall, as well as varying degrees of hydrothermal activity and pyroclastic rock weathering (Zhang et al., 2018). It is therefore a useful testbed for evaluating the potentially coupled effects of alkaline basin evolution and local fluid-temperature dynamics and related alteration on the preservation of high $\delta^{15}N$ data. There, a maximum $\delta^{15}N$ of 24.4‰ was reported among a consistently elevated data set (mean = 18.9‰, n = 56). Using $\delta^{18}O_{carb}$, TOC/TS, and rare earth elements and yttrium [REE+Y] as salinity proxies, Xia et al. (2020) argued that pH and salinity increases were decoupled in the paleolake. It was also inferred via europium anomalies [Eu*/Eu] that hydrothermal activity may have been the primary driver of increased pH. However, it should be noted that $\delta^{15}N$ was used exclusively as a pH proxy by Xia et al. (2020), whereby shifts in the range of 16 to 24‰ were interpreted as direct responses to changes in pH. Our

results from the Coorong lakes in **Chapter 3** and from the GRF suggest, however, that elevation of $\delta^{15}N$ results from a complex interplay of geochemical parameters and may therefore provide valuable insight into multiple aspects of aqueous composition in a lake. This complexity could alter its value as a sensitive pH proxy because pH is not the sole determining factor of (1) the capacity for volatilization to occur and (2) the extent of associated fractionation. Further insights on this topic come from studies of the Quaternary Bosumtwi impact crater lake system.

Lake Bosumtwi

Lake Bosumtwi is an extant impact crater lake located within the Obuom Range, ~30 km southeast of Kumasi, Ghana (Jones et al., 1981). The 11 km-diameter depression has likely housed a lake since its genesis at 1.07 Ma, and it has no natural outlet except in cases of overflow (Koeberl et al., 1998; Shanahan et al., 2006). The lake is currently oligohaline (~0.7 PSU) with elevated pH (9.1-9.6) and permanently anoxic bottom waters (Talbot & Johannessen, 1992). Importantly, it is known to have gone through multiple aridity-induced lowstands accompanied by increases in salinity. These characteristics indicate that it may be an ideal system for elucidating the effects of evapo-concentration (i.e., transient increases in salinity) on NH_3 volatilization and associated effects on $\delta^{15}N$.

A stable isotope study of the lake's sedimentary history over the last 27,500 years was conducted by Talbot & Johannessen (1992) who showed that modern surface sediments at Bosumtwi range in $\delta^{15}N$ from 4.03 to 7.81‰. There is clear evidence that the lake's sedimentary $\delta^{15}N$ only exceeds 10‰ during intervals of relatively intense evaporation (i.e.,

lowstands), which facilitates seasonal partial mixing of the water column. In redox-stratified settings, ammonic species may accumulate below the chemocline, and therefore overturn of the water column may be critical for escape of gaseous ammonia (Jellison et al., 1993). Based on the presence of dolomite with a high $\delta^{18}O$ composition, salinity during lowstands may have been significantly elevated compared to the modern system (Talbot & Kelts, 1986). However, only qualitative assessments of relative paleosalinity can be gleaned from currently published isotopic and mineralogical data. It has been speculated that the previously saline system was effectively diluted during an overflow event in the recent past (Turner et al., 1996). Conversely, an observed major highstand interval exhibits values of $\delta^{15}N$ that are < 4‰, despite evidence of permanent redox stratification that could have allowed for water-column denitrification. Over the past ~3 kyr, the lake has been at intermediate levels, which, as with lowstands, allow for seasonal partial mixing driven primarily by winds. The resulting $\delta^{15}N$ values fluctuate between 8 and 12‰. Bosumtwi highlights the importance of water column mixing and evaporation on $\delta^{15}N$ elevation via ammonia volatilization.

Synthesis

Our review enables a novel assessment of the essential characteristics underlying ammonia volatilization. The foremost constraint is that pH must be greater than 7.5; at pH < 7.5, there is likely not enough ammonia (i.e., NH_3 rather than NH_4^+) being generated to produce a robust isotopic signature (Li et al., 2012; **Chapter 3**). Each of the discussed

locations have independent lines of evidence beyond $\delta^{15}N$ data that point to high pH values, including their mafic weathering environments and/or the preservation of alkaline carbonate minerals such as trona or dolomite.

Hypersalinity appears to facilitate $\delta^{15}N$ fractionation via ammonia volatilization, but it remains unclear whether it is an essential prerequisite. Multiples studies point to inhibition of nitrification as being volumetrically important under hypersaline conditions, either by enabling ammonium accumulation, preventing denitrification, or both (e.g., Collister & Hayes, 1991; Isaji et al., 2019; **Chapter 3**).

Our new, high-resolution data set from the GRF links evapo-concentration and elevated $\delta^{15}N$ in sediments of the Uinta basin, which is at odds with previous literature from this location (Collister & Hayes, 1991) but in agreement with observations at both

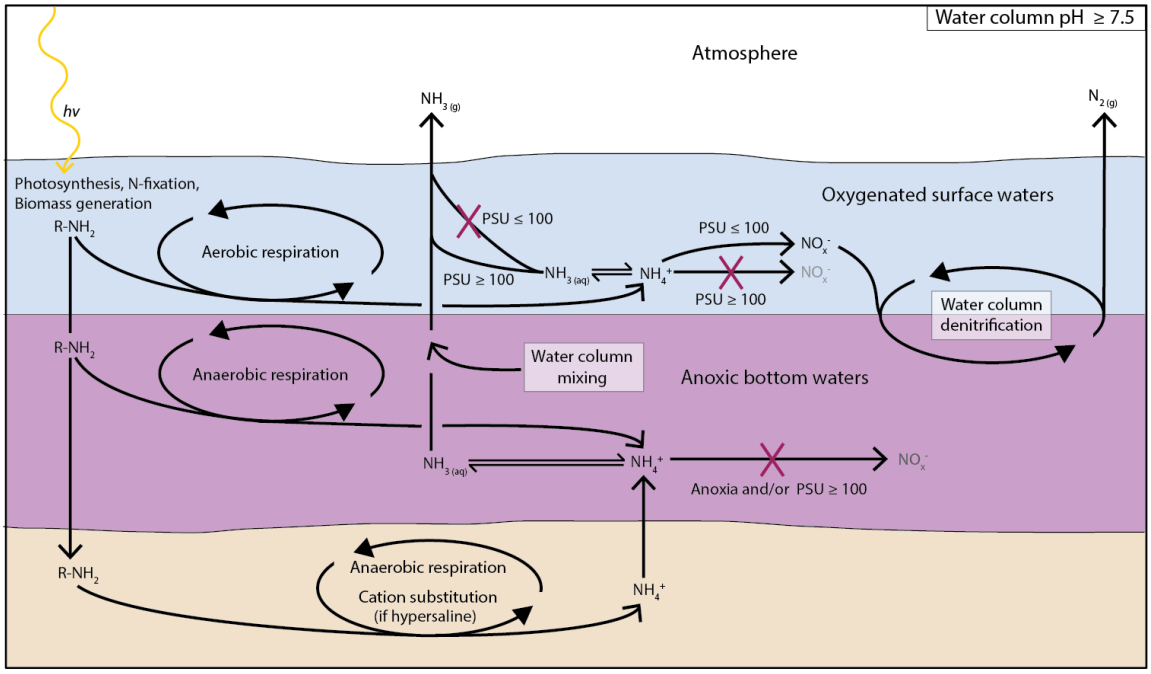

Figure 4.4 A proposed schematic of nitrogen cycling in redox-stratified basins where pH ≥ 7.5. Multiple routes of gaseous, unidirectional N escape that can result in elevated $\delta^{15}N$ are depicted. The important attributes and implications of this schematic are described in detail in the **Synthesis** section. Salinity and redox-stratification dictate the relative influence of ammonia volatilization versus denitrification.

Lake Bosumtwi and the Coorong lakes (Talbot & Johannessen, 1992; **Chapter 3**). In contrast, at the Fengcheng, it has been suggested that salinity and pH were decoupled during the intervals of highest $\delta^{15}N$ (Xia et al., 2020). We suggest that the use of $\delta^{15}N$ as a direct and sensitive pH proxy (e.g., to determine pH = 8.5 versus pH = 9.5) is complex and must be used with care and in combination with other, independent constraints on environmental conditions, such as tracers of paleosalinity. For example, independent evidence for high pH and hypersalinity within an endorheic basin would be ideal for leveraging the specific role of pH in impacting $\delta^{15}N$.

If circumstances allow for volatilization, the intensity of the effect and its resulting isotopic fractionation may be increased or decreased by changes in certain parameters. Based on the discussed studies, those vital parameters include pH, salinity, evaporation rate, biological productivity (as a source and sink of ammonium to the water column) and temperature. Experimental and theoretical work has repeatedly shown the importance of pH and temperature on fractionation (Deng et al., 2018; Li et al., 2012; Urey, 1947). For example, at a given pH, a hot solution would evolve more ammonia gas than one with moderate temperatures due to the temperature-dependent nature of the equilibrium constant (K_a) between ammonium and ammonia in water. Moreover, while heightened temperatures decrease instantaneous fractionation (e.g., Li et al., 2012), the continual unidirectional escape of ammonia could result in a Rayleigh distillation effect (a concept described in **Chapter 1**) that increases water-column $\delta^{15}N_{ammonium}$ over time. The data of Xia et al. (2020) may support this possibility through a positive correlation observed between inferred hydrothermal activity (Eu/Eu*) and $\delta^{15}N$. It is possible that pH was stagnant while

intensified hydrothermal activity and associated temperature increases produced more NH_3, assuming pH was already > 7.5. In this light, it is perhaps unsurprising that multiple sites exhibiting $\delta^{15}N > 10‰$ are closely linked to temperature-elevating phenomena, such as impact-induced hydrothermal activity and proximal volcanics (e.g., Stüeken, Tino et al., 2020; Xia et al., 2020).

To unify the discussed concepts, we propose a new schematic for elevated $\delta^{15}N$ in endorheic, redox-stratification settings (**Fig. 4.4**). This is complementary to the shallow hypersaline schematic presented in **Chapter 3** (**Fig. 3.7**). There is not a universal depth threshold for redox stratification, although Sullivan (1985) suggested depths of approximately 30 m were necessary for stratification at the GRF. While redox is an important part of the story, the goal of this schematic to more generally to depict how $\delta^{15}N$ preservation in the sediments of closed-basin alkaline systems is likely the net result of multiple N-cycling processes occurring in oxygenated surface waters, anoxic bottom waters, and sediments.

In oxygenated surface waters, salinity may dictate the mode of nitrogen isotope fractionation. Under hypersaline conditions (≥ 100 PSU; see **Chapter 3**), microbial nitrification may be significantly dampened, allowing for the accumulation of ammonic species even in the presence of O_2 (Isaji et al., 2019). If waters above the chemocline are not hypersaline, nitrate will be readily produced by biological nitrification. That nitrate is transported downward to low O_2 waters that favor nitrate reduction (biological denitrification), and the greater the proportion of denitrification that occurs in the water column, the larger the fractionation effect associated with that pathway (Devol, 2015;).

Within the anoxic bottom waters, anaerobic respiration in both the water column and sediments produces a stable ammonium reservoir below the chemocline. If the bottom waters are hypersaline, this may enhance cation substitution in clays and further promote the efflux of ammonium from sediments to the water column (Rysgaard et al., 1999). The amount of ammonium converted to ammonia is then dependent on pH. Given the sedimentary record of Bosumtwi, it appears that frequent mixing of the water column is necessary for the appreciable release of ammonia from bottom waters that underly non-hypersaline, oxygenated surface waters. If mixing does not occur, much of the upward-migrating ammonia gas can be expected to be nitrified within the oxygenated surface waters. For this reason, the Tumbiana Formation that was deposited under an anoxic atmosphere may have facilitated NH_3 escape, as oxidation to NO_x was suppressed by O_2 limitation (possibly in addition to salinity-induced suppression of nitrification).

Ultimately, our schematic introduces a dynamic scenario where the fractionation effects of ammonia volatilization and denitrification are co-occurring. For example, significant freshwater input could alter salinity in surface waters such that it drops from > 100 PSU to < 100 PSU. More nitrate would be produced under these conditions, and consequent denitrification would have a stronger influence on the overall $\delta^{15}N$ composition of the system. Thus, the depth of chemocline and the frequency of mixing may exert strong controls the relative extents ammonia volatilization and denitrification.

Conclusion

While there is still much to learn about the geologic preservation of elevated $\delta^{15}N$ values in the sediments of closed-basin systems, the collected and growing body of literature on ammonia volatilization offers valuable insights. Rather than being a stringently pH-controlled phenomenon, multiple other parameters (e.g., salinity, evaporation rate, and temperature) appear to play variable yet significant roles in facilitating and/or intensifying $\delta^{15}N$ fractionation linked specifically to the unidirectional escape of gaseous NH_3. In redox-stratified endorheic lakes, the relative roles of ammonia volatilization and denitrification represent a critical balance that dictates the eventual sedimentary isotopic expression in organic matter. There is little evidence that denitrification itself can lead to the long-term preservation of $\delta^{15}N \geq 10‰$ in sediments, as many sites with values of this magnitude display independent lines of evidence of high alkalinity and/or high pH. However, systems that exhibit ammonia volatilization may also facilitate varying degrees of denitrification in the water column (**Fig. 4.4**). We propose that while large enrichments in $\delta^{15}N$ can occur as a result of ammonia volatilization alone, scenarios where denitrification augments ammonia volatilization are highly plausible and warrant strong consideration in studies examining samples highly enriched in ^{15}N.

References

Bian, W., Hornung, J., Liu, Z., Wang, P., & Hinderer, M. (2010). Sedimentary and palaeoenvironmental evolution of the Junggar Basin, Xinjiang, Northwest China. *Palaeobiodiversity and Palaeoenvironments*, *90*(3), 175–186.

Birgenheier, L. P., Berg, M. D. Vanden, Plink-Björklund, P., Gall, R. D., Rosencrans, E., Rosenberg, M. J., Toms, L. C., & Morris, J. (2020). Climate impact on fluvial-lake system evolution, Eocene Green River Formation, Uinta Basin, Utah, USA. *GSA Bulletin*, *132*(3–4), 562–587.

Blake, T. S., Buick, R., Brown, S. J. A., & Barley, M. E. (2004). Geochronology of a Late Archaean flood basalt province in the Pilbara Craton, Australia: constraints on basin evolution, volcanic and sedimentary accumulation, and continental drift rates. *Precambrian Research*, *133*(3–4), 143–173.

Bradley, W. H. (1931). *Origin and microfossils of the oil shale of the Green River formation of Colorado and Utah*.

Buick, R. (1992). The Antiquity of Oxygenic Photosynthesis: Evidence from Stromatolites in Sulphate-Deficient Archaean Lakes. *Science*, *255*(5040), 74–77.

Carroll, A. R., & Bohacs, K. M. (1999). Stratigraphic classification of ancient lakes: Balancing tectonic and climatic controls. *Geology*, *27*(2), 99–102.

Coffey, J. M., Flannery, D. T., Walter, M. R., & George, S. C. (2013). Sedimentology, stratigraphy and geochemistry of a stromatolite biofacies in the 2.72Ga Tumbiana Formation, Fortescue Group, Western Australia. *Precambrian Research*, *236*, 282–296.

Collister, J. W., & Hayes, J. M. (1991). A preliminary study of the carbon and nitrogen isotopic biogeochemistry of lacustrine sedimentary rocks from the Green River Formation, Wyoming, Utah, and Colorado. In M. L. Tuttle (Ed.), *Geochemical, biogeochemical, and sedimentological studies of the Green River Formation, Wyoming, Utah, and Colorado* (pp. C1–C14). USGS.

Collister, J. W., Summons, R. E., Lichtfouse, E., & Hayes, J. M. (1992). An isotopic biogeochemical study of the Green River oil shale. *Organic Geochemistry*, *19*(1–3), 265–276.

Deng, Y., Li, Y., & Li, L. (2018). Experimental investigation of nitrogen isotopic effects associated with ammonia degassing at 0–70 °C. *Geochimica et Cosmochimica Acta*, *226*, 182–191.

Devol, A. H. (2015). Denitrification, Anammox, and N $_2$ Production in Marine Sediments. *Annual Review of Marine Science*, *7*(1), 403–423.

Elson, A. L., Rohrssen, M., Marshall, J., Inglis, G. N., & Whiteside, J. H. (2022). Hydroclimate variability in the United States continental interior during the early Eocene Climatic Optimum. *Palaeogeography, Palaeoclimatology, Palaeoecology*, *595*, 110959.

Feulner, G. (2012). The faint young Sun problem. *Reviews of Geophysics*, *50*(2).

Fogel, M. L., & Cifuentes, L. A. (1993). *Isotope Fractionation during Primary Production* (M. H. Engel & S. A. Macko, Eds.; pp. 73–98).

French, K. L., Birdwell, J. E., & Vanden Berg, M. D. (2020). Biomarker similarities between the saline lacustrine Eocene Green River and the Paleoproterozoic Barney Creek Formations. *Geochimica et Cosmochimica Acta*, *274*, 228–245.

Gislason, S. R., & Eugster, H. P. (1987). Meteoric water-basalt interactions. I: A laboratory study. *Geochimica et Cosmochimica Acta*, *51*(10), 2827–2840.

Hoch, M. P., Fogel, M. L., & Kirchman, D. L. (1992). Isotope fractionation associated with ammonium uptake by a marine bacterium. *Limnology and Oceanography*, *37*(7), 1447–1459.

Howarth, R. W., & Marino, R. (2006). Nitrogen as the limiting nutrient for eutrophication in coastal marine ecosystems: Evolving views over three decades. *Limnology and Oceanography*, *51*, 364–376.

Isaji, Y., Kawahata, H., Ogawa, N. O., Kuroda, J., Yoshimura, T., Jiménez-Espejo, F. J., Makabe, A., Shibuya, T., Lugli, S., Santulli, A., Manzi, V., Roveri, M., & Ohkouchi, N. (2019). Efficient recycling of nutrients in modern and past hypersaline environments. *Scientific Reports*, *9*(1), 3718.

Jones, W. B., Bacon, M., & Hastings, D. A. (1981). The Lake Bosumtwi impact crater, Ghana. *Geological Society of America Bulletin*, *92*(6), 342–349.

Koeberl, C., Bottomley, R., Glass, B. P., & Storzer, D. (1997). Geochemistry and age of Ivory Coast tektites and microtektites. *Geochimica et Cosmochimica Acta*, *61*(8), 1745–1772.

Koeberl, C., Reimold, W., Blum, J. D., & Chamberlain, C. P. (1998). Petrology and geochemistry of target rocks from the Bosumtwi impact structure, Ghana, and comparison with Ivory Coast tektites. *Geochimica et Cosmochimica Acta*, *62*(12), 2179–2196.

Li, L., Lollar, B. S., Li, H., Wortmann, U. G., & Lacrampe-Couloume, G. (2012). Ammonium stability and nitrogen isotope fractionations for –NH3(aq)–NH3(gas) systems at 20–70°C and pH of 2–13: Applications to habitability and nitrogen cycling in low-temperature hydrothermal systems. *Geochimica et Cosmochimica Acta*, *84*, 280–296.

Lowenstein, T. K., Jagniecki, E. A., Carroll, A. R., Smith, M. E., Renaut, R. W., & Owen, R. B. (2017). The Green River salt mystery: What was the source of the hyperalkaline lake waters? *Earth-Science Reviews*, *173*, 295–306.

Niles, P. B., Catling, D. C., Berger, G., Chassefière, E., Ehlmann, B. L., Michalski, J. R., Morris, R., Ruff, S. W., & Sutter, B. (2013). Geochemistry of Carbonates on Mars: Implications for Climate History and Nature of Aqueous Environments. *Space Science Reviews*, *174*(1–4), 301–328.

Papineau, D., Purohit, R., Goldberg, T., Pi, D., Shields, G. A., Bhu, H., Steele, A., & Fogel, M. L. (2009). High primary productivity and nitrogen cycling after the Paleoproterozoic phosphogenic event in the Aravalli Supergroup, India. *Precambrian Research*, *171*(1–4), 37–56.

Rysgaard, S., Thastum, P., Dalsgaard, T., Christensen, P. B., & Sloth, N. P. (1999). Effects of Salinity on NH4+ Adsorption Capacity, Nitrification, and Denitrification in Danish Estuarine Sediments. *Estuaries*, *22*, 21–30.

Sagan, C., & Mullen, G. (1972). Earth and Mars: Evolution of Atmospheres and Surface Temperatures. *Science*, *177*(4043), 52–56.

Shanahan, T. M., Overpeck, J. T., Wheeler, C. W., Beck, J. W., Pigati, J. S., Talbot, M. R., Scholz, C. A., Peck, J., & King, J. W. (2006). Paleoclimatic variations in West Africa from a record of late Pleistocene and Holocene lake level stands of Lake Bosumtwi, Ghana. *Palaeogeography, Palaeoclimatology, Palaeoecology*, *242*(3–4), 287–302.

Sharp, Z. (2017). *Principles of Stable Isotope Geochemistry* (2nd ed.).

Sigman, D. M., & Fripiat, F. (2019). Nitrogen Isotopes in the Ocean. In *Encyclopedia of Ocean Sciences* (pp. 263–278). Elsevier.

Smith, J. W., & Robb, W. A. (1973). *Aragonite and the genesis of carbonates in Mahogany Zone oil shales of Colorado's Green River Formation*. (Vol. 7727). US Department of Interior, Bureau of Mines.

Smith, M. E., Carroll, A. R., & Singer, B. S. (2008). Synoptic reconstruction of a major ancient lake system: Eocene Green River Formation, western United States. *Geological Society of America Bulletin*, *120*(1–2), 54–84.

Stüeken, E. E., Buick, R., & Schauer, A. J. (2015). Nitrogen isotope evidence for alkaline lakes on late Archean continents. *Earth and Planetary Science Letters*, *411*, 1–10.

Stüeken, E. E., Kipp, M. A., Koehler, M. C., & Buick, R. (2016). The evolution of Earth's biogeochemical nitrogen cycle. *Earth-Science Reviews*, *160*, 220–239.

Stüeken, E. E., Tino, C., Arp, G., Jung, D., & Lyons, T. W. (2020). Nitrogen isotope ratios trace high-pH conditions in a terrestrial Mars analog site. *Science Advances*, *6*(9).

Sullivan, R. (1985). Origin of Lacustrine Rocks of Wilkins Peak Member, Wyoming. *AAPG Bulletin*, *69*(6), 913–922.

Talbot, M. R. (2002). *Nitrogen Isotopes in Palaeolimnology* (W. M. Last & J. P. Smol, Eds.; pp. 401–439).

Talbot, M. R., & Johannessen, T. (1992). A high resolution palaeoclimatic record for the last 27,500 years in tropical West Africa from the carbon and nitrogen isotopic composition of lacustrine organic matter. *Earth and Planetary Science Letters*, *110*(1–4), 23–37.

Talbot, M. R., & Kelts, K. (1986). Primary and diagenetic carbonates in the anoxic sediments of Lake Bosumtwi, Ghana. *Geology*, *14*(11), 912–916.

Thomazo, C., Ader, M., & Philippot, P. (2011). Extreme ^{15}N-enrichments in 2.72-Gyr-old sediments: evidence for a turning point in the nitrogen cycle. *Geobiology*, *9*(2), 107–120.

Turner, B. F., Gardner, L. R., & Sharp, W. E. (1996). The hydrology of Lake Bosumtwi, a climate-sensitive lake in Ghana, West Africa. *Journal of Hydrology*, *183*(3–4), 243–261.

Urey, H. C. (1947). The thermodynamic properties of isotopic substances. *Journal of the Chemical Society (Resumed)*, 562–581.

Vanden Berg, M. D., & Birgenheier, L. P. (2017). An examination of the hypersaline phases of Eocene Lake Uinta, upper Green River Formation, Uinta Basin, Utah. *Journal of Paleolimnology*, *58*(3), 353–371.

Walters, A. P., Meyers, S. R., Carroll, A. R., Hill, T. R., & Vanden Berg, M. D. (2020). Lacustrine cyclicity in the early Eocene Green River Formation, Uinta Basin, Utah: Evidence from X-ray fluorescence core scanning. *Journal of Sedimentary Research*, *90*(4), 429–447.

Wang, T., Cao, J., Xia, L., Zhi, D., Tang, Y., & He, W. (2022). Revised age of the Fengcheng Formation, Junggar Basin, China: Global implications for the late Paleozoic ice age. *Global and Planetary Change*, *208*, 103725.

Xia, L., Cao, J., Jin, J., Xiang, B., Ma, W., & Wang, T. (2022). Response of nitrogen isotopes to paleo-environment and organic carbon accumulation in a Late Paleozoic alkaline lake, Junggar Basin. *Chemical Geology*, *602*, 120884.

Xia, L., Cao, J., Stüeken, E. E., Zhi, D., Wang, T., & Li, W. (2020). Unsynchronized evolution of salinity and pH of a Permian alkaline lake influenced by hydrothermal fluids: A multi-proxy geochemical study. *Chemical Geology*, *541*, 119581.

Zhang, X., Ward, B. B., & Sigman, D. M. (2020). Global Nitrogen Cycle: Critical Enzymes, Organisms, and Processes for Nitrogen Budgets and Dynamics. *Chemical Reviews*, *120*(12), 5308–5351.

Zhang, Z., Yuan, X., Wang, M., Zhou, C., Tang, Y., Chen, X., Lin, M., & Cheng, D. (2018). Alkaline-lacustrine deposition and paleoenvironmental evolution in Permian Fengcheng Formation at the Mahu sag, Junggar Basin, NW China. *Petroleum Exploration and Development*, *45*(6), 1036–1049.